Jordan Journal of
PHYSICS
An International Peer-Reviewed Research Journal

Volume 8, No. 1, 2015, 1436 H

Jordan Journal of Physics (*JJP*): An International Peer-Reviewed Research Journal issued by the support of the Scientific Research Support Fund, Ministry of Higher Education and Scientific Research, Jordan, and published biannually by the Deanship of Research and Graduate Studies, Yarmouk University, Irbid, Jordan.

Manuscripts should be submitted to:

Prof. Nehad M. Tashtoush
Editor-in-Chief, Jordan Journal of Physics
Deanship of Research and Graduate Studies
Yarmouk University-Irbid-Jordan
Tel. 00 962 2 7211111 Ext. 2075
E-mail: *jjp@yu.edu.jo*
Website: *http://Journals.yu.edu.jo/jjp*

Jordan Journal of

PHYSICS

An International Peer-Reviewed Research Journal

Volume 8, No. 1, 2015, 1436 H

INTERNATIONAL ADVISORY BOARD

Prof. Dr. Ahmad Saleh
Department of Physics, Yarmouk University, Irbid, Jordan.
salema@yu.edu.jo

Prof. Dr. Aurore Savoy-Navarro
LPNHE Universite de Paris 6/IN2P3-CNRS, Tour 33, RdC 4, Place Jussieu, F 75252, Paris Cedex 05, France.
auore@lpnhep.in2p3.fr

Prof. Dr. Bernard Barbara
Laboratoire Louis Neel, Salle/Room: D 108, 25, Avenue des Martyrs BP 166, 38042-Grenoble Cedex 9, France.
Barbara@grenoble.cnrs.fr

Prof. Dr. Bruno Guiderdoni
Observatoire Astronomique de Lyon, g, avenue Ch. Antre-F-69561, Saint Genis Laval Cedex, France.
Bruno.guiderdoni@olos.univ-lyon1.fr

Prof. Dr. Buford Price
Physics Department, University of California, Berkeley, CA 94720, U. S. A.
bprice@berkeley.edu

Prof. Dr. Colin Cough
School of Physics and Astronomy, University of Birmingham, B15 2TT, U. K.
c.gough@bham.ac.uk

Prof. Dr. Desmond Cook
Department of Physics, Condensed Matter and Materials Physics Research Group, Old Dominion University, Norfolk, Virginia 23529, U. S. A.
Dcook@physics.odu.edu

Prof. Dr. Evgeny Sheshin
MIPT, Institutskij per. 9, Dogoprudnyi 141700, Russia.
sheshin@lafeet.mipt.ru

Prof. Dr. Hans Ott
Laboratorium Fuer Festkorperphysik, ETH Honggerberg, CH-8093 Zurich, Switzerland.
ott@solid.phys.ethz.ch

Prof. Dr. Herwig Schopper
President SESAME Council, Chairman Scientific Board UNESCO IBSP Programme, CERN, 1211 Geneva, Switzerland.
Herwig.Schopper@cern.ch

Prof. Dr. Humam Ghassib
Department of Physics, Jordan University, Amman, Jordan.
humam@atf.org.jo

Prof. Dr. Ingo Hofmann
GSI Darmstadt, Planckstr. 1, 64291, Darmstadt, Germany.
i.hofmann@gsi.de

Prof. Dr. Jozef Lipka
Department of Nuclear Physics and Technology, Slovak University of Technology, Bratislava, llkovicova 3, 812 19 Bratislava, Slovakia.
Lipka@elf.stuba.sk

Prof. Dr. Khalid Touqan
Chairman of Jordan Atomic Energy Commission, Amman, Jordan.

Prof. Dr. Mark J. Hagmann
Desert Electronics Research Corporation, 762 Lacey Way, North Salt Lake 84064, Utah, U. S. A.
MHagmann@NewPathResearch.Com.

Prof. Dr. Nasr Zubeidey
President*: Al-Zaytoonah University of Jordan, Amman, Jordan.*
President@alzaytoonah.edu.jo

Prof. Dr. Patrick Roudeau
Laboratoire de l'Accelerateur, Lineaire (LAL), Universite Paris-Sud 11, Batiment 200, 91898 Orsay Cedex, France.
roudeau@mail.cern.ch

Prof. Dr. Paul Chu
Department of Physics, University of Houston, Houston, Texas 77204-5005, U. S. A.
Ching-Wu.Chu@mail.uh.edu

Prof. Dr. Peter Dowben
Nebraska Center for Materials and Nanoscience, Department of Physics and Astronomy, 255 Behlen Laboratory (10th and R Streets), 116 Brace Lab., P. O. Box 880111, Lincoln, NE 68588-0111, U. S. A.
pdowben@unl.edu

Prof. Dr. Peter Mulser
Instiute fuer Physik, T.U. Darmstadt, Hochschulstr. 4a, 64289 Darmstadt, Germany.
Peter.mulser@physik.tu-darmstadt.de

Prof. Dr. Rasheed Azzam
Department of Electrical Engineering, University of New Orleans New Orleans, Louisiana 70148, U. S. A.
razzam@uno.edu

Dr. Richard G. Forbes
University of Surrey, FEPS (X1), Guildford, Surrey GU2 7XH, U. K.
R.Forbes@surrey.ac.uk

Prof. Dr. Roy Chantrell
Physics Department, York University, York, YO10 5DD, U. K.
Rc502@york.ac.uk

Prof. Dr. Shawqi Al-Dallal
Department of Physics, Faculty of Science, University of Bahrain, Manamah, Kingdom of Bahrain.

Prof. Dr. Susamu Taketomi
Matsumoto Yushi-Seiyaku Co. Ltd., Shibukawa-Cho, Yao City, Osaka 581-0075, Japan.
staketomi@hotmail.com

Prof. Dr. Wolfgang Nolting
Institute of Physics / Chair: Solid State Theory, Humboldt-University at Berlin, Newtonstr. 15 D-12489 Berlin, Germany
Wolfgang.nolting@physik.hu-berlin.de

The Hashemite Kingdom of Jordan

Yarmouk University

Jordan Journal of
PHYSICS

An International Peer-Reviewed Research Journal issued by the
Support of the Scientific Research Support Fund

Volume 8, No. 1, 2015, 1436 H

Instructions to Authors

Instructions to authors concerning manuscript organization and format apply to hardcopy submission by mail, and also to electronic online submission via the Journal homepage website (http://jjp.yu.edu.jo).

Manuscript Submission

1- **E-mail to** : jjp@yu.edu.jo

2- **Online**: Follow the instructions at the journal homepage website.

Original *Research Articles*, *Communications* and *Technical Notes* are subject to critical review by minimum of two competent referees. Authors are encouraged to suggest names of competent reviewers. *Feature Articles* in active Physics research fields, in which the author's own contribution and its relationship to other work in the field constitute the main body of the article, appear as a result of an invitation from the Editorial Board, and will be so designated. The author of a *Feature Article* will be asked to provide a clear, concise and critical status report of the field as an introduction to the article. *Review Articles* on active and rapidly changing Physics research fields will also be published. Authors of *Review Articles* are encouraged to submit two-page proposals to the Editor-in-Chief for approval. Manuscripts submitted in *Arabic* should be accompanied by an Abstract and Keywords in English.

Organization of the Manuscript

Manuscripts should be typed double spaced on one side of A4 sheets (21.6 x 27.9 cm) with 3.71 cm margins, using Microsoft Word 2000 or a later version thereof. The author should adhere to the following order of presentation: Article Title, Author(s), Full Address and E-mail, Abstract, PACS and Keywords, Main Text, Acknowledgment. Only the first letters of words in the Title, Headings and Subheadings are capitalized. Headings should be in **bold** while subheadings in *italic* fonts.

Title Page: Includes the title of the article, authors' first names, middle initials and surnames and affiliations. The affiliation should comprise the department, institution (university or company), city, zip code and state and should be typed as a footnote to the author's name. The name and complete mailing address, telephone and fax numbers, and e-mail address of the author responsible for correspondence (designated with an asterisk) should also be included for official use. The title should be carefully, concisely and clearly constructed to highlight the emphasis and content of the manuscript, which is very important for information retrieval.

Abstract: A one paragraph abstract not exceeding 200 words is required, which should be arranged to highlight the purpose, methods used, results and major findings**.**

Keywords: A list of 4-6 keywords, which expresses the precise content of the manuscript for indexing purposes, should follow the abstract.

PACS: Authors should supply one or more relevant PACS-2006 classification codes, (available at http://www.aip.org/pacs/pacs06/pacs06-toc.html)

Introduction: Should present the purpose of the submitted work and its relationship to earlier work in the field, but it should not be an extensive review of the literature (e.g., should not exceed 1 ½ typed pages).

Experimental Methods: Should be sufficiently informative to allow competent reproduction of the experimental procedures presented; yet concise enough not to be repetitive of earlier published procedures.

Results: should present the results clearly and concisely.

Discussion: Should be concise and focus on the interpretation of the results.

Conclusion: Should be a brief account of the major findings of the study not exceeding one typed page.

Acknowledgments: Including those for grant and financial support if any, should be typed in one paragraph directly preceding the References.

References: References should be typed double spaced and numbered sequentially in the order in which they are cited in the text. References should be cited in the text by the appropriate Arabic numerals, enclosed in square brackets. Titles of journals are abbreviated according to list of scientific periodicals. The style and punctuation should conform to the following examples:

1. Journal Article:

a) Heisenberg, W., Z. Phys. 49 (1928) 619.
b) Bednorz, J. G. and Müller, K. A., Z. Phys. B64 (1986) 189
c) Bardeen, J., Cooper, L.N. and Schrieffer, J. R., Phys. Rev. 106 (1957) 162.
d) Asad, J. H., Hijjawi, R. S., Sakaji, A. and Khalifeh, J. M., Int. J. Theor. Phys. 44(4) (2005), 3977.

2. Books with Authors, but no Editors:

a) Kittel, C., "Introduction to Solid State Physics", 8th Ed. (John Wiley and Sons, New York, 2005), chapter 16.
b) Chikazumi, S., C. D. Graham, JR, "Physics of Ferromagnetism", 2nd Ed. (Oxford University Press, Oxford, 1997).

3. Books with Authors and Editors:

a) Allen, P. B. "Dynamical Properties of Solids", Ed. (1), G. K. Horton and A. A. Maradudin (North-Holland, Amsterdam, 1980), p137.
b) Chantrell, R. W. and O'Grady, K., "Magnetic Properities of Fine Particles" Eds. J. L. Dormann and D. Fiorani (North-Holland, Amsterdam, 1992), p103.

4. Technical Report:

Purcell, J. "The Superconducting Magnet System for the 12-Foot Bubble Chamber", report ANL/HEP6813, Argonne Natt. Lab., Argonne, III, (1968).

5. Patent:

Bigham, C. B., Schneider, H. R., US patent 3 925 676 (1975).

6. Thesis:

Mahmood, S. H., Ph.D. Thesis, Michigan State University, (1986), USA (Unpublished).

7. Conference or Symposium Proceedings:

Blandin, A. and Lederer, P. Proc. Intern. Conf. on Magnetism, Nottingham (1964), P.71.

8. Internet Source:

Should include authors' names (if any), title, internet website, URL, and date of access.

9. Prepublication online articles (already accepted for publication):

Should include authors' names (if any), title of digital database, database website, URL, and date of access.

For other types of referenced works, provide sufficient information to enable readers to access them.

Tables: Tables should be numbered with Arabic numerals and referred to by number in the Text (e.g., Table 1). Each table should be typed on a separate page with the legend above the table, while explanatory footnotes, which are indicated by superscript lowercase letters, should be typed below the table.

Illustrations: Figures, drawings, diagrams, charts and photographs are to be numbered in a consecutive series of Arabic numerals in the order in which they are cited in the text. Computer-generated illustrations and good-quality digital photographic prints are accepted. They should be black and white originals (not photocopies) provided on separate pages and identified with their corresponding numbers. Actual size graphics should be provided, which need no further manipulation, with lettering (Arial or Helvetica) not smaller than 8 points, lines no thinner than 0.5 point, and each of uniform density. All colors should be removed from graphics except for those graphics to be considered for publication in color. If graphics are to be submitted digitally, they should conform to the following minimum resolution requirements: 1200 dpi for black and white line art, 600 dpi for grayscale art, and 300 dpi for color art. All graphic files must be saved as TIFF images, and all illustrations must be submitted in the actual size at which they should appear in the journal. Note that good quality hardcopy original illustrations are required for both online and mail submissions of manuscripts.

Text Footnotes: The use of text footnotes is to be avoided. When their use is absolutely necessary, they should be typed at the bottom of the page to which they refer, and should be cited in the text by a superscript asterisk or multiples thereof. Place a line above the footnote, so that it is set off from the text.

Supplementary Material: Authors are encouraged to provide all supplementary materials that may facilitate the review process, including any detailed mathematical derivations that may not appear in whole in the manuscript.

Revised Manuscript and Computer Disks

Following the acceptance of a manuscript for publication and the incorporation of all required revisions, authors should submit an original and one more copy of the final disk containing the complete manuscript typed double spaced in Microsoft Word for Windows 2000 or a later version thereof. All graphic files must be saved as PDF, JPG, or TIFF images.

Allen, P.B., "…………….", in: Horton, G.K., and Muradudin, A. A., (eds.), "Dynamical…….", (North……..), pp….

Reprints

Twenty (20) reprints free of charge are provided to the corresponding author. For orders of more reprints, a reprint order form and prices will be sent with the article proofs, which should be returned directly to the Editor for processing.

Copyright

Submission is an admission by the authors that the manuscript has neither been previously published nor is being considered for publication elsewhere. A statement transferring copyright from the authors to Yarmouk University is required before the manuscript can be accepted for publication. The necessary form for such transfer is supplied by the Editor-in-Chief. Reproduction of any part of the contents of a published work is forbidden without a written permission by the Editor-in-Chief.

Disclaimer

Opinions expressed in this Journal are those of the authors and neither necessarily reflects the opinions of the Editorial Board or the University, nor the policy of the Higher Scientific Research Committee or the Ministry of Higher Education and Scientific Research. The publisher shoulders no responsibility or liability whatsoever for the use or misuse of the information published by JJP.

Indexing

JJP is currently applying for indexing and abstracting to all related International Services.

Jordan Journal of
PHYSICS
An International Peer-Reviewed Research Journal

Volume 8, No. 1, 2015, 1436 H

Table of Contents:

Volume 8, Number 1, 2015. pp. 1-16

Jordan Journal of Physics

ARTICLE

Relativistic Energy and Mass in the Weak Field Limit

Sergey G. Fedosin

P.O. Box 614088, Sviazeva Str. 22-79, Perm, Russia.

Received on: 13/5/2014; Accepted on: 21/9/2014

Abstract: Within the framework of the covariant theory of gravitation (CTG), the energy is calculated for a system with continuously distributed matter, taking into account the contribution of the gravitational and electromagnetic fields and the contribution of the pressure and acceleration fields. The total energy of all the fields is equal to zero, and the system's energy is formed from the energy of the particles, which are under the influence of these fields. From the expression for the energy, the inertial M and gravitational m_g masses of the system are found. These masses are compared with mass m_b, obtained by integrating the density over the volume, and with the total mass m' of the body particles scattered to infinity in order to make the energy of macroscopic fundamental fields equal to zero. The ratio for the masses is obtained: $m' = M < m_b = m_g$. From this the possibility of non-radiative ideal spherical collapse follows, when the system's mass M does not change during the collapse. In addition, the mass of the system is less than the gravitational mass. In contrast, in the general theory of relativity (GTR), the ratio for masses is obtained in a different form: $M = m_g < m_b < m'$. In CTG, the electromagnetic field energy reduces the gravitational mass; whereas in GTR, on the contrary, the electromagnetic field energy increases the gravitational mass. In order to verify the obtained results, it is suggested to conduct an experiment on measuring the change of the gravitational mass of the body with increasing its electrical charge.

Keywords: Relativistic energy; Mass; Acceleration field; Pressure field; Covariant theory of gravitation (CTG).

Introduction

Modern physical theories usually describe the energy, momentum and mass of a system in four-dimensional formalism and introduce various 4-vectors and 4-tensors to be taken into consideration. In order to simplify comparison of the obtained expressions, it is convenient to turn to such a weak field limit, that most of the formulae could be written in the same form as in the special theory of relativity, without loss of accuracy. In this work, this will be done for the covariant theory of gravitation and general theory of relativity; particular attention will be paid to the meaning acquired by the mass in these theories.

Energy and Mass in the Covariant Theory of Gravitation

We will calculate the relativistic energy for the body in the form of a sphere with the uniform density of mass and charge, moving at velocity $\mathbf{v}$ along the axis OX of the reference frame K. The body under consideration is a set of identical particles moving randomly in different directions within the specified sphere with the radius a. We will assume that all of these particles are held together by the force of gravitation. In order to simplify, we will assume that the spaces between the particles are so small that integration over the volume of all the particles is equivalent to integration over the volume of the sphere. The sphere is at rest in the

Corresponding Author: Sergey G. Fedosin **Email**: sergey.fedosin@gmail.com

co-moving reference frame K', associated with the center of mass, and the velocities of particles in K' are equal to $\mathbf{v}'$ and depend on the coordinates.

The Hamiltonian for continuously distributed matter in the covariant theory of gravitation is obtained from the Lagrangian with the help of Legendre transformations. This Hamiltonian is equal to the relativistic energy of the system and has the form [1-2]:

$$\left.\begin{aligned} E &= \frac{1}{c}\int \left(\rho_0 \vartheta + \rho_0 \psi + \rho_{0q} \varphi + \rho_0 \wp \right) u^0 \sqrt{-g}\, dx^1 dx^2 dx^3 - \\ &- \int \left(\frac{c^2}{16\pi G} \Phi_{\mu\nu} \Phi^{\mu\nu} - \frac{1}{4\mu_0} F_{\mu\nu} F^{\mu\nu} - \frac{c^2}{16\pi\sigma} f_{\mu\nu} f^{\mu\nu} - \frac{c^2}{16\pi\eta} u_{\mu\nu} u^{\mu\nu} \right) \sqrt{-g}\, dx^1 dx^2 dx^3 . \end{aligned} \right\} \qquad (1)$$

Here, c is the speed of light, ρ_0 is the mass density of an arbitrary point particle in the reference frame K_p associated with the particle, ϑ is the scalar potential of the acceleration field, ψ is the scalar potential of the gravitational field, ρ_{0q} is the charge density in the reference frame K_p, φ is the scalar potential of the electromagnetic field, $\wp$ is the scalar potential of the pressure field, u^0 denotes the timelike component of the 4-velocity of the particle, $\sqrt{-g}$ includes the determinant g of the metric tensor with the minus sign, $dx^1 dx^2 dx^3$ is an element of the three-dimensional volume in the reference frame K, G is the gravitational constant, $\Phi_{\mu\nu}$ is the gravitational tensor, μ_0 is the vacuum permeability, $F_{\mu\nu}$ is the electromagnetic tensor, $u_{\mu\nu}$ is the acceleration tensor, $f_{\mu\nu}$ is the pressure field tensor, η and σ are constants.

For our purposes, it suffices to consider the expression for relativistic energy (1) in the case when the sphere under consideration is at rest in K. Then, all the calculations can be performed in the reference frame K' associated with the system's center of mass. Let us assume that the gravitational field is small and the covariant theory of gravitation turns into the Lorentz-invariant theory of gravitation. In this case, the metric tensor $g_{\mu\nu}$ no longer depends on the coordinates and is transformed into the metric tensor of Minkowski spacetime $\eta_{\mu\nu}$ which is used in the special theory of relativity. For the case of the single fixed system, the expressions for physical quantities are as follows:

$$\vartheta = c g_{0\mu} u^{\mu} = c u_0 = \gamma' c^2 , \qquad u^0 = u_0 = \gamma' c ,$$

$$\frac{c^2}{16\pi G} \Phi_{\mu\nu} \Phi^{\mu\nu} = -\frac{1}{8\pi G} \left(\Gamma^2 - c^2 \Omega^2 \right),$$

$$\frac{1}{4\mu_0} F_{\mu\nu} F^{\mu\nu} = -\frac{\varepsilon_0}{2} (E^2 - c^2 B^2),$$

$$\frac{c^2}{16\pi\sigma} f_{\mu\nu} f^{\mu\nu} = -\frac{1}{8\pi\sigma} (C^2 - c^2 I^2),$$

$$\sqrt{-g} = 1,$$

$$\frac{c^2}{16\pi\eta} u_{\mu\nu} u^{\mu\nu} = -\frac{1}{8\pi\eta} (S^2 - c^2 N^2), \qquad (2)$$

where the Lorentz factor is $\gamma' = \frac{1}{\sqrt{1 - v'^2 / c^2}}$, v' is the particle's velocity in K', $\mathbf{\Gamma}$ is the gravitational field strength, $\mathbf{\Omega}$ is the torsion field vector, $\mathbf{E}$ is the electric field strength, $\mathbf{B}$ is the magnetic field induction, ε_0 is the vacuum permittivity, $\mathbf{C}$ is the pressure field strength, $\mathbf{I}$ is the solenoidal vector of the pressure field, $\mathbf{S}$ is the acceleration field strength, $\mathbf{N}$ is the solenoidal vector of the acceleration field.

Substituting expressions (2) into (1) gives the following:

$$\left.\begin{aligned}E_b &= \int \left(\rho_0 c^2 \gamma' + \rho_0 \psi + \rho_{0q}\varphi + \rho_0 \wp\right)\gamma'\, dx^1 dx^2 dx^3 + \\ &+\int\left(\frac{1}{8\pi G}\left(\Gamma^2 - c^2\Omega^2\right) - \frac{\varepsilon_0}{2}(E^2 - c^2B^2) - \frac{1}{8\pi\sigma}(C^2 - c^2I^2) - \frac{1}{8\pi\eta}(S^2 - c^2N^2)\right) dx^1 dx^2 dx^3.\end{aligned}\right\} \qquad (3)$$

First, we will calculate the first integral in (3). According to [2], the Lorentz factor γ' for the particles inside the fixed sphere is function of the current radius r:

$$\left.\begin{aligned}\gamma' &= \frac{c\gamma_c}{r\sqrt{4\pi\eta\rho_0}}\sin\left(\frac{r}{c}\sqrt{4\pi\eta\rho_0}\right) \\ &\approx \gamma_c - \frac{2\pi\eta\rho_0 r^2\gamma_c}{3c^2}\end{aligned}\right\}, \qquad (4)$$

where $\gamma_c = \frac{1}{\sqrt{1 - v_c^2/c^2}}$ is the Lorentz factor for velocities v_c of the particles in the center of the sphere, and due to the smallness of the argument the sine can be expanded to the second-order terms.

For the first term in the first integral in (3) with regard to (4) in spherical coordinates, we can write:

$$\left.\begin{aligned}\int \rho_0 c^2 \gamma'^2\, dx^1 dx^2 dx^3 &= \frac{c^4\gamma_c^2}{4\pi\eta}\int \frac{1}{r^2}\sin^2\left(\frac{r}{c}\sqrt{4\pi\eta\rho_0}\right) r^2 \sin\theta\, dr\, d\theta\, d\phi \\ &= \frac{c^4\gamma_c^2}{\eta}\left(\frac{a}{2} - \frac{c}{4\sqrt{4\pi\eta\rho_0}}\sin\left(\frac{2a}{c}\sqrt{4\pi\eta\rho_0}\right)\right) \approx mc^2\gamma_c^2 - \frac{3\eta m^2\gamma_c^2}{5a}.\end{aligned}\right\} \qquad (5)$$

In (5), the mass m is the product of the density of the particles' mass ρ_0 by the volume V_b of the sphere which is at rest in the reference frame K'. The origin of the factor γ_c^2 in (5) can be understood from the following. The quantity $\rho_0\gamma_c$ is the mass density of the particles in the center, which can be seen in the reference frame K'. Then, the product $\rho_0\gamma_c V_b = m\gamma_c = m_c$ gives the mass of the particles in the sphere for the observer in K' in the case, as if all the particles were in the center of the sphere. It is obvious that $m_c > m = \rho_0 V_b$. In (5), it occurs that $mc^2\gamma_c^2 = m_c c^2\gamma_c$, meaning that the total energy of the particles, increased due to the internal motion of the particles, is regarded by the Lorentz factor γ_c. The second term in (5) appears due to the radial gradient of mean velocities of the particles inside the sphere and takes into account that not all the particles are located in the center of the sphere.

The scalar potential of the gravitational field in (3) inside the sphere, according to [2], is equal to:

$$\left.\begin{aligned}\psi_i &= \frac{Gc^2\gamma_c}{\eta}\cos\left(\frac{a}{c}\sqrt{4\pi\eta\rho_0}\right) \\ &\quad - \frac{Gc^3\gamma_c}{r\eta\sqrt{4\pi\eta\rho_0}}\sin\left(\frac{r}{c}\sqrt{4\pi\eta\rho_0}\right) \\ &\approx \frac{2\pi G\gamma_c\rho_0(r^2 - 3a^2)}{3}.\end{aligned}\right\} \qquad (6)$$

Based on the similarity of the gravitational and electromagnetic fields, we can write for the electric potential, similarly to (6):

$$\left.\begin{aligned}\varphi_i &= -\frac{c^2\gamma_c}{4\pi\varepsilon_0\eta}\cos\left(\frac{a}{c}\sqrt{4\pi\eta\rho_{0q}}\right) \\ &\quad + \frac{c^3\gamma_c}{4\pi\varepsilon_0 r\eta\sqrt{4\pi\eta\rho_{0q}}}\sin\left(\frac{r}{c}\sqrt{4\pi\eta\rho_{0q}}\right) \\ &\approx -\frac{\gamma_c\rho_{0q}(r^2 - 3a^2)}{6\varepsilon_0}.\end{aligned}\right\} \qquad (7)$$

The scalar potential of the pressure field inside the sphere equals:

$$\left.\begin{aligned}
\wp &= \wp_c - \frac{\sigma c^2 \gamma_c}{\eta} \\
&\quad + \frac{\sigma c^3 \gamma_c}{r\eta\sqrt{4\pi\eta\rho_0}}\sin\left(\frac{r}{c}\sqrt{4\pi\eta\rho_0}\right) \\
&\approx \wp_c - \frac{2\pi\sigma\rho_0 r^2\gamma_c}{3}
\end{aligned}\right\}, \qquad (8)$$

where $\wp_c$ denotes the potential of the pressure field in the center of the sphere.

Substituting (6), (7) and (8) into (3), taking into account (4), we find:

$$\left.\begin{aligned}
&\int \rho_0 \psi_i\, \gamma' dx^1 dx^2 dx^3 \\
&= \frac{G\rho_0 c^3 \gamma_c^2}{\eta\sqrt{4\pi\eta\rho_0}} \int \left(\begin{array}{l} \cos\left(\frac{a}{c}\sqrt{4\pi\eta\rho_0}\right) \\ -\frac{c}{r\sqrt{4\pi\eta\rho_0}}\sin\left(\frac{r}{c}\sqrt{4\pi\eta\rho_0}\right) \end{array}\right) \frac{1}{r}\sin\left(\frac{r}{c}\sqrt{4\pi\eta\rho_0}\right) r^2 \sin\theta\, dr\, d\theta\, d\phi \\
&= \frac{Gc^4\gamma_c^2}{\eta^2}\left[\cos\left(\frac{a}{c}\sqrt{4\pi\eta\rho_0}\right)\left(\begin{array}{l} \frac{c}{\sqrt{4\pi\eta\rho_0}}\sin\left(\frac{a}{c}\sqrt{4\pi\eta\rho_0}\right) \\ -a\cos\left(\frac{a}{c}\sqrt{4\pi\eta\rho_0}\right) \end{array}\right) - \frac{a}{2} + \frac{c}{4\sqrt{4\pi\eta\rho_0}}\sin\left(\frac{2a}{c}\sqrt{4\pi\eta\rho_0}\right)\right] \\
&\approx -\frac{3Gm^2\gamma_c^2}{2a}.
\end{aligned}\right\} \qquad (9)$$

$$\int \rho_{0q}\varphi_i\, \gamma' dx^1 dx^2 dx^3 \approx \frac{3q^2\gamma_c^2}{8\pi\varepsilon_0 a}. \qquad (10)$$

$$\left.\begin{aligned}
&\int \rho_0 \wp \gamma' dx^1 dx^2 dx^3 \\
&= \frac{c\gamma_c\rho_0}{\sqrt{4\pi\eta\rho_0}} \int \left[\wp_c - \frac{\sigma c^2\gamma_c}{\eta} + \frac{\sigma c^3\gamma_c}{r\eta\sqrt{4\pi\eta\rho_0}}\sin\left(\frac{r}{c}\sqrt{4\pi\eta\rho_0}\right)\right] \frac{1}{r}\sin\left(\frac{r}{c}\sqrt{4\pi\eta\rho_0}\right) r^2\sin\theta\, dr\, d\theta\, d\phi = \\
&= \frac{c^2\gamma_c}{\eta}\left[\begin{array}{l} \left(\wp_c - \frac{\sigma c^2\gamma_c}{\eta}\right)\left[\frac{c}{\sqrt{4\pi\eta\rho_0}}\sin\left(\frac{a}{c}\sqrt{4\pi\eta\rho_0}\right) - a\cos\left(\frac{a}{c}\sqrt{4\pi\eta\rho_0}\right)\right] + \\ + \frac{\sigma c^2\gamma_c}{\eta}\left(\frac{a}{2} - \frac{c}{4\sqrt{4\pi\eta\rho_0}}\sin\left(\frac{2a}{c}\sqrt{4\pi\eta\rho_0}\right)\right) \end{array}\right] \\
&\approx m\,\wp_c\gamma_c - \frac{3\sigma m^2\gamma_c^2}{10a}.
\end{aligned}\right\} \qquad (11)$$

With regard to (5) and (9-11), the first integral in (3) will equal:

$$\left.\begin{aligned}
&\int \left(\rho_0 c^2\gamma' + \rho_0\psi + \rho_{0q}\varphi + \rho_0\wp\right)\gamma' dx^1 dx^2 dx^3 \\
&= mc^2\gamma_c^2 - \frac{3\eta m^2\gamma_c^2}{5a} - \frac{3Gm^2\gamma_c^2}{2a} + \frac{3q^2\gamma_c^2}{8\pi\varepsilon_0 a} + m\,\wp_c\gamma_c - \frac{3\sigma m^2\gamma_c^2}{10a}.
\end{aligned}\right\} \qquad (12)$$

The gravitational field strength and the torsion field inside the sphere are given by the formulae:

$$\mathbf{\Gamma} = -\nabla \psi - \frac{\partial \mathbf{D}}{\partial t}, \quad \mathbf{\Omega} = \nabla \times \mathbf{D}, \qquad (13)$$

where $\mathbf{D}$ is the vector potential of the gravitational field.

The vector potential of each particle is directed along its velocity, and due to random directions of the particles' velocities, the total vector potential $\mathbf{D}$ inside and outside the sphere is zero. Consequently, the torsion field will also be zero: $\mathbf{\Omega} = 0$. Substituting the scalar potential (6) into (13), we find the gravitational field strength:

$$\left.\begin{aligned} \mathbf{\Gamma}_i &= -\nabla \psi_i \\ &= -\frac{G c^2 \gamma_c \mathbf{r}}{\eta r^3}\left[\begin{aligned}&\frac{c}{\sqrt{4\pi \eta \rho_0}} \sin\left(\frac{r}{c}\sqrt{4\pi \eta \rho_0}\right) \\ &-r\cos\left(\frac{r}{c}\sqrt{4\pi \eta \rho_0}\right)\end{aligned}\right] \\ &\approx -\frac{4\pi G \rho_0 \gamma_c \mathbf{r}}{3}. \end{aligned}\right\} \qquad (14)$$

Taking into account (14) and the equality $\mathbf{\Omega} = 0$ for the integral of the first term in the second integral in (3), we have:

$$\left.\begin{aligned} &\int \frac{1}{8\pi G}\left(\Gamma_i^2 - c^2 \Omega_i^2\right) dx^1 dx^2 dx^3 \\ &= \frac{G c^4 \gamma_c^2}{2\eta^2} \int \left[\frac{c}{\sqrt{4\pi \eta \rho_0}} \sin\left(\frac{r}{c}\sqrt{4\pi \eta \rho_0}\right) - r\cos\left(\frac{r}{c}\sqrt{4\pi \eta \rho_0}\right)\right]^2 \frac{1}{r^2} dr \\ &= \frac{G c^6 \gamma_c^2}{8\pi \eta^3 \rho_0}\left[\frac{2\pi \eta \rho_0 a}{c^2} + \frac{\sqrt{4\pi \eta \rho_0}}{4c} \sin\left(\frac{2a}{c}\sqrt{4\pi \eta \rho_0}\right) - \frac{1}{a}\sin^2\left(\frac{a}{c}\sqrt{4\pi \eta \rho_0}\right)\right] \\ &\approx \frac{G m^2 \gamma_c^2}{10a}. \end{aligned}\right\} \qquad (15)$$

According to [2], the potential of the gravitational field outside the sphere equals:

$$\psi_o = -\frac{G c^3 \gamma_c}{\eta r \sqrt{4\pi \eta \rho_0}}\left[\sin\left(\frac{a}{c}\sqrt{4\pi \eta \rho_0}\right) - \frac{a}{c}\sqrt{4\pi \eta \rho_0}\cos\left(\frac{a}{c}\sqrt{4\pi \eta \rho_0}\right)\right] \approx -\frac{G m \gamma_c}{r}\left(1 - \frac{3\eta m}{10ac^2}\right).$$

From this, it follows that the gravitational mass of the sphere is equal to the quantity $m_g = m\gamma_c\left(1 - \frac{3\eta m}{10ac^2}\right)$.

Using (13), with $\mathbf{D} = 0$, we find the field strength:

$$\left.\begin{aligned} \mathbf{\Gamma}_o &= -\nabla \psi_o = -\frac{G c^3 \gamma_c \mathbf{r}}{\eta r^3 \sqrt{4\pi \eta \rho_0}}\left[\sin\left(\frac{a}{c}\sqrt{4\pi \eta \rho_0}\right) - \frac{a\sqrt{4\pi \eta \rho_0}}{c}\cos\left(\frac{a}{c}\sqrt{4\pi \eta \rho_0}\right)\right] \\ &\approx -\frac{4\pi G \rho_0 a^3 \gamma_c \mathbf{r}}{3r^3} = -\frac{G m \gamma_c \mathbf{r}}{r^3}. \end{aligned}\right\}$$

Substituting $\mathbf{\Gamma}_o$ into (3), using the equation $\mathbf{\Omega}=0$, we find for the gravitational field outside the sphere:

$$\left.\begin{aligned}&\int \frac{1}{8\pi G}\left(\Gamma_o^2-c^2\Omega_o^2\right)dx^1dx^2dx^3\\&\approx\frac{Gm^2\gamma_c^2}{2}\int\frac{1}{r^2}dr=\frac{Gm^2\gamma_c^2}{2a}.\end{aligned}\right\}\qquad(16)$$

The sum of (15) and (16) equals:

$$\left.\begin{aligned}&\int \frac{1}{8\pi G}\left(\Gamma^2-c^2\Omega^2\right)dx^1dx^2dx^3\\&=\frac{3Gm^2\gamma_c^2}{5a}\end{aligned}\right\}.\qquad(17)$$

The calculation of the term with the electromagnetic field in (3) is done similarly and gives for uniformly charged particles inside the stationary sphere the following:

$$\left.\begin{aligned}&-\int \frac{\varepsilon_0}{2}(E^2-c^2B^2)dx^1dx^2dx^3\\&=-\frac{3q^2\gamma_c^2}{20\pi\varepsilon_0 a}\end{aligned}\right\},\qquad(18)$$

where the charge q is the product of the charge density ρ_{0q} of an arbitrary particle in the reference frame K_p associated with the particle by the volume V_b of the stationary sphere.

In Minkowski space, the 4-velocity of the stationary sphere is $\hat{u}_\mu=u'_\mu=(c,0,0,0)$, and based on the definition of the total 4-potential of the sphere's pressure field $\pi_\mu=\frac{p_b}{\rho_b c^2}\hat{u}_\mu=\left(\frac{\wp}{c},-\mathbf{\Pi}\right)$, we find $\wp=\frac{p_b}{\rho_b}$, $\mathbf{\Pi}=0$, where ρ_b denotes the density inside the stationary sphere. In this case, the scalar potential $\wp$, density ρ_b and pressure inside the sphere p_b are functions of the current radius inside the sphere, and the equality $\mathbf{\Pi}=0$ for the vector potential of the pressure field in this case follows from the absence of ordered motion of particles inside the sphere. In view of this and (8) for $\wp$, the vectors $\mathbf{C}$ and $\mathbf{I}$ inside the sphere are expressed as follows:

$$\mathbf{C}=-\nabla\wp-\frac{\partial\mathbf{\Pi}}{\partial t}=-\nabla\wp,\ \mathbf{I}=\nabla\times\mathbf{\Pi}=0.$$

In case of uniform mass density ρ_0, calculations for the vector of the pressure strength inside the sphere give the following:

$$\left.\begin{aligned}&\mathbf{C}=-\nabla\wp\\&=\frac{\sigma c^2\gamma_c\mathbf{r}}{\eta r^3}\left[\begin{aligned}&\frac{c}{\sqrt{4\pi\eta\rho_0}}\sin\left(\frac{r}{c}\sqrt{4\pi\eta\rho_0}\right)\\&-r\cos\left(\frac{r}{c}\sqrt{4\pi\eta\rho_0}\right)\end{aligned}\right]\\&\approx\frac{4\pi\sigma\rho_0\gamma_c\mathbf{r}}{3}.\end{aligned}\right\}$$

Using this, we calculate the integral for the pressure:

$$\left.\begin{aligned}&-\int\frac{1}{8\pi\sigma}(C^2-c^2I^2)\,dx^1dx^2dx^3=\\&=-\frac{\sigma c^4\gamma_c^2}{2\eta^2}\int\left[\frac{c}{\sqrt{4\pi\eta\rho_0}}\sin\left(\frac{r}{c}\sqrt{4\pi\eta\rho_0}\right)-r\cos\left(\frac{r}{c}\sqrt{4\pi\eta\rho_0}\right)\right]^2\frac{1}{r^2}dr=\\&=-\frac{\sigma c^6\gamma_c^2}{8\pi\eta^3\rho_0}\left[\frac{2\pi\eta\rho_0 a}{c^2}+\frac{\sqrt{4\pi\eta\rho_0}}{4c}\sin\left(\frac{2a}{c}\sqrt{4\pi\eta\rho_0}\right)-\frac{1}{a}\sin^2\left(\frac{a}{c}\sqrt{4\pi\eta\rho_0}\right)\right]\\&\approx-\frac{\sigma m^2\gamma_c^2}{10a}.\end{aligned}\right\}\qquad(19)$$

We have to calculate one more term in the second integral in (3). The components of vectors $\mathbf{S}$ and $\mathbf{N}$ for the acceleration field are found as follows:

$$\mathbf{S} = -\nabla \vartheta - \frac{\partial \mathbf{U}}{\partial t}, \quad \mathbf{N} = \nabla \times \mathbf{U},$$

where the scalar potential ϑ and the vector potential $\mathbf{U}$ are part of the 4-potential of the acceleration field $u_\mu = \left(\frac{\vartheta}{c}, -\mathbf{U} \right)$, which is a covariant 4-velocity.

In the limit of special theory of relativity $u_\mu = (c\gamma, -\mathbf{v}\gamma)$, where $\gamma = \frac{1}{\sqrt{1 - v^2/c^2}}$ is the Lorentz factor for the velocity $\mathbf{v}$ of the particle's motion. In the reference frame K', the particle's velocities inside the sphere are equal to $\mathbf{v}'$ and γ' should be used instead of γ. Then, the potentials of an arbitrary particle will be $\vartheta' = c^2 \gamma'$, $\mathbf{U}' = \mathbf{v}'\gamma'$. We need the total potentials of the acceleration field inside the sphere, emerging due to direct interaction of the particles with each other and due to the influence of fields. In case of random motion of particles, the velocities $\mathbf{v}'$ are directed in different directions, and therefore, inside the sphere $\mathbf{U} = 0$ and $\mathbf{N} = 0$. However, the total Lorentz factor of particles γ' is a function of the current radius, and the total scalar potential $\vartheta = c^2 \gamma'$ is not equal to zero. With regard to (4), for γ', it gives the following:

$$\left. \begin{aligned} \mathbf{S} &= -c^2 \nabla \gamma' \\ &= \frac{c^2 \gamma_c \mathbf{r}}{r^3} \left[\begin{aligned} &\frac{c}{\sqrt{4\pi\eta\rho_0}} \sin\left(\frac{r}{c} \sqrt{4\pi\eta\rho_0} \right) \\ &- r\cos\left(\frac{r}{c} \sqrt{4\pi\eta\rho_0} \right) \end{aligned} \right] \\ &\approx \frac{4\pi\eta\rho_0 \gamma_c \mathbf{r}}{3}. \end{aligned} \right\}$$

We will calculate the last integral:

$$\left. \begin{aligned} &-\int \frac{1}{8\pi\eta} (S^2 - c^2 N^2)\, dx^1 dx^2 dx^3 = \\ &= -\frac{c^4 \gamma_c^2}{2\eta} \int \left[\frac{c}{\sqrt{4\pi\eta\rho_0}} \sin\left(\frac{r}{c} \sqrt{4\pi\eta\rho_0} \right) - r\cos\left(\frac{r}{c} \sqrt{4\pi\eta\rho_0} \right) \right]^2 \frac{1}{r^2} dr = \\ &= -\frac{c^4 \gamma_c^2}{2\eta} \left[\frac{a}{2} + \frac{c}{4\sqrt{4\pi\eta\rho_0}} \sin\left(\frac{2a}{c} \sqrt{4\pi\eta\rho_0} \right) - \frac{c^2}{4\pi\eta\rho_0 a} \sin^2\left(\frac{a}{c} \sqrt{4\pi\eta\rho_0} \right) \right] \\ &\approx -\frac{\eta m^2 \gamma_c^2}{10a}. \end{aligned} \right\} \qquad (20)$$

Substituting (12), (17), (18), (19) and (20) into (3), we find the relativistic energy of the system:

$$\left. \begin{aligned} E_b = mc^2\gamma_c^2 &- \frac{3\eta m^2 \gamma_c^2}{5a} - \frac{3G m^2 \gamma_c^2}{2a} \\ &+ \frac{3q^2 \gamma_c^2}{8\pi\varepsilon_0 a} + m\,\wp_c \gamma_c - \frac{3\sigma m^2 \gamma_c^2}{10a} \\ &+ \frac{3G m^2 \gamma_c^2}{5a} - \frac{3q^2 \gamma_c^2}{20\pi\varepsilon_0 a} \\ &- \frac{\sigma m^2 \gamma_c^2}{10a} - \frac{\eta m^2 \gamma_c^2}{10a}. \end{aligned} \right\} \qquad (21)$$

In [2], the coefficients σ and η were calculated for the case under consideration:

$$\eta = \sigma = 3G - \frac{3q^2}{4\pi\varepsilon_0 m^2}. \qquad (22)$$

If we substitute (22) into (21), we will see that the field energies are canceled completely. Only the energy of particles in corresponding fields remains:

$$\left.\begin{aligned} E_b &= m c^2 \gamma_c^2 - \frac{3\eta m^2 \gamma_c^2}{5a} \\ &- \frac{3G\, m^2 \gamma_c^2}{2a} + \frac{3q^2 \gamma_c^2}{8\pi \varepsilon_0 a} \\ &+ m\, \wp_c \gamma_c - \frac{3\sigma m^2 \gamma_c^2}{10a} \end{aligned}\right\}. \qquad (23)$$

Equation (22) fixes a definite relation between the pressure field, acceleration field and gravitational and electromagnetic fields. This relation according to [2] reveals the fact that the conserved integral 4-vector, which is the result of integrating the equations of motion, is equal to zero. In this case, condition (22) appears, and within the given model the 4/3 problem is explained.

Let us estimate the total mass of particles in the sphere, for which, taking into account (4), we integrate the mass density $\rho_b = \rho_0 \gamma'$ of particles in K' over the sphere's volume:

$$\left.\begin{aligned} m_b &= \int \rho_0 \gamma' r^2 \sin\theta\, dr\, d\theta\, d\phi \\ &= \frac{4\pi \rho_0 c\, \gamma_c}{\sqrt{4\pi \eta \rho_0}} \int \sin\left(\frac{r}{c}\sqrt{4\pi \eta \rho_0}\right) r\, dr \\ &= \frac{c^2 \gamma_c}{\eta} \left[\begin{aligned} &\frac{c}{\sqrt{4\pi \eta \rho_0}} \sin\left(\frac{a}{c}\sqrt{4\pi \eta \rho_0}\right) \\ &-a \cos\left(\frac{a}{c}\sqrt{4\pi \eta \rho_0}\right) \end{aligned} \right] \\ &\approx m\, \gamma_c \left(1 - \frac{3\eta m}{10ac^2}\right). \end{aligned}\right\} (24)$$

Hence, by solving the quadratic equation, we obtain: $m \gamma_c \approx m_b + \frac{3\eta m_b^2}{10ac^2 \gamma_c}$. Similarly, we can link the charge q with the charge q_b of the sphere, which is found by the observer in K': $q \gamma_c \approx q_b + \frac{3\eta q_b^2}{10ac^2 \gamma_c}$. We will substitute this into (23), given $\eta = \sigma$ from (22):

$$\left.\begin{aligned} E_b &= m_b c^2 \gamma_c - \frac{3\eta m_b^2}{5a} \\ &- \frac{3G\, m_b^2}{2a} + \frac{3q_b^2}{8\pi \varepsilon_0 a} + m_b\, \wp_c \end{aligned}\right\}. \qquad (25)$$

From (8), we will express the scalar potential $\wp_c$ of the pressure field in the center in terms of the potential $\wp_s$ near the surface of the sphere, and will consider the ratio $m \gamma_c \approx m_b + \frac{3\eta m_b^2}{10ac^2 \gamma_c}$:

$$\left.\begin{aligned} \wp_c &= \frac{2\pi \sigma \rho_0 a^2 \gamma_c}{3} + \wp_s \\ &= \frac{\sigma m\, \gamma_c}{2a} + \wp_s \approx \frac{\sigma m_b}{2a} + \wp_s \end{aligned}\right\}. \qquad (26)$$

Similarly, from (4), we will express γ_c in terms of the Lorentz factor γ_s of the particles near the surface of the sphere:

$$\left.\begin{aligned} \gamma_c &= \gamma_s + \frac{2\pi \eta \rho_0 a^2 \gamma_c}{3c^2} \\ &= \gamma_s + \frac{\eta m\, \gamma_c}{2ac^2} \approx \gamma_s + \frac{\eta m_b}{2ac^2} \end{aligned}\right\}. \qquad (27)$$

If we take into account (27) and (22) into (24), we can specify the relation between m_b and m:

$$\left.\begin{aligned} m_b &\approx m\, \gamma_s \left(1 - \frac{3\eta m}{10ac^2} + \frac{\eta m_b}{2ac^2 \gamma_s}\right) \\ &\approx m\, \gamma_s + \frac{\eta m^2}{5ac^2} \\ &\approx m + \frac{3G\, m^2}{5ac^2} - \frac{3q^2}{20\pi \varepsilon_0 a c^2} \end{aligned}\right\}. \qquad (28)$$

Substitution of (22), (26) and (27) in (25) gives the following:

$$\left.\begin{aligned} E_b &= M\, c^2 \\ &= m_b c^2 \gamma_s - \frac{3G\, m_b^2}{10a} \\ &+ \frac{3q_b^2}{40\pi \varepsilon_0 a} + m_b\, \wp_s \end{aligned}\right\}. \qquad (29)$$

(29) shows that when the covariant theory of gravitation in the weak field limit turns into Lorentz- invariant theory of gravitation, all fields in the system, including the acceleration field,

pressure field, electromagnetic and gravitational fields compensate each other so that the relativistic energy depends only on the mass, the energy of gravitational and electromagnetic fields, the energy of the surface pressure and the velocity of particles on the surface.

The scalar potential of the pressure field near the sphere's surface is connected with the pressure by relation: $\wp_s = \frac{p_s}{\rho_s}$, where p_s and ρ_s denote, respectively, the pressure and the mass density near the surface of the sphere. Using the relation $m_b = \bar{\rho} V_b$, where $\bar{\rho}$ is the average density with respect to the sphere's volume, we find: $m_b \wp_s = p_s V_b \frac{\bar{\rho}}{\rho_s} \ge p_s V_b$. For those massive bodies, in which we can assume $\gamma_s \approx 1$ and neglect the pressure p_s on the surface, (29) becomes a simple expression:

$$E_b \approx m_b c^2 - \frac{3G m_b^2}{10a} + \frac{3q_b^2}{40\pi \varepsilon_0 a}. \qquad (30)$$

From (29), we will express the mass of the system consisting of the matter mass m_b and the mass of the four fields associated with this system:

$$M = m_b \left(\gamma_s + \frac{\wp_s}{c^2} \right) - \frac{3G m_b^2}{10ac^2} + \frac{3q_b^2}{40\pi \varepsilon_0 ac^2}. (31)$$

The mass M is identical, at rest and in motion, and it is the invariant inertial mass of the system. Above, we found from the formula for the external gravitational potential ψ_o that the gravitational mass of the sphere is the quantity $m_g = m\gamma_c \left(1 - \frac{3\eta m}{10ac^2} \right)$. Comparison with (24) shows that the sphere's mass m_b according to our assumptions is equal to the gravitational mass m_g. According to (31), the system's inertial mass M increases relative to the mass m_b by the value of mass-energy of the surface pressure, and to a certain share of the mass-energy of the electromagnetic field, but it decreases due to the same share of the mass-energy of the gravitational field.

Relations between the Energies

We will compare the different energy components that make up the total relativistic energy (29). We will denote by E_{fg}, E_{fe}, E_{fp} and E_{fa} the energy components of the electromagnetic and gravitational fields, the pressure field and the acceleration field, respectively. As the measurement unit of energy, we will use the sum E_{fge} of the energy components of the electromagnetic and gravitational fields from (17) and (18). Taking into account (24), (19), (20) and (22), we find:

$$\left. \begin{aligned} E_{fge} &= E_{fg} + E_{fe} \\ &= \frac{3G m^2 \gamma_c^2}{5a} - \frac{3q^2 \gamma_c^2}{20\pi \varepsilon_0 a} \\ &\approx \frac{3G m_b^2}{5a} - \frac{3q_b^2}{20\pi \varepsilon_0 a} \end{aligned} \right\}. \qquad (32)$$

$$E_{fp} = -\frac{\sigma m^2 \gamma_c^2}{10a} \approx -\frac{\sigma m_b^2}{10a} = -\frac{1}{2} E_{fge},$$

$$E_{fa} = -\frac{\eta m^2 \gamma_c^2}{10a} \approx -\frac{\eta m_b^2}{10a} = -\frac{1}{2} E_{fge}.$$

According to (32), the energy components of the pressure field and acceleration field are twice less than the sum E_{fge} of the energy components of the gravitational and electromagnetic fields and have a different sign. As a result, the sum of field energy components in (21) is equal to zero.

We will now consider the energy components of the matter particles which are under the influence of fields. We will denote these components by E_{pg}, E_{pe}, E_{pp} and E_{pa}, as the energy components of the particle in the electromagnetic and gravitational fields, the pressure field and the acceleration field, respectively. According to (9), (10), (11), (26), (5) and (27), we have the following:

$$E_{pg} = -\frac{3G m^2 \gamma_c^2}{2a} \approx -\frac{3G m_b^2}{2a},$$

$$E_{pe} = \frac{3q^2 \gamma_c^2}{8\pi \varepsilon_0 a} \approx \frac{3q_b^2}{8\pi \varepsilon_0 a},$$

$$E_{pg}+E_{pe}=-\frac{3G\,m_b^2}{2a}+\frac{3\,q_b^2}{8\pi\varepsilon_0 a}=-\frac{5}{2}E_{fge},$$

$$\left.\begin{aligned} E_{pp} &= m\,\wp_c\gamma_c-\frac{3\sigma m^2\gamma_c^2}{10a} \\ &\approx m_b\,\wp_c-\frac{3\sigma m_b^2}{10a} \\ &= m_b\,\wp_s+\frac{\sigma m_b^2}{5a} \\ &= m_b\,\wp_s+E_{f\,ge} \end{aligned}\right\}, \qquad (33)$$

$$\left.\begin{aligned} E_{pa} &= mc^2\gamma_c^2-\frac{3\eta m^2\gamma_c^2}{5a} \\ &\approx m_b c^2\gamma_c-\frac{3\eta m_b^2}{10a} \\ &= m_b c^2\gamma_s+\frac{\eta m_b^2}{5a} \\ &= m_b c^2\gamma_s+E_{f\,ge} \end{aligned}\right\}.$$

Now, we will sum up the energy components in (32) and (33) separately for each field:

$$\left.\begin{aligned} E_{ge} &= E_{fg}+E_{fe}+E_{pg}+E_{pe}=-\frac{3}{2}E_{fge}, \\ E_p &= E_{fp}+E_{pp}=m_b\,\wp_s+\frac{1}{2}E_{fge}, \\ E_a &= E_{fa}+E_{pa}=m_b c^2\gamma_s+\frac{1}{2}E_{fge}. \end{aligned}\right\} \qquad (34)$$

The quantity E_{ge} denotes the sum of the energy components of the gravitational and electromagnetic fields, including the energy components of the fields themselves and of particles in these fields. The definition of E_{fge} is given in (32). The sum of all the energy components in (34) equals the relativistic energy of the system (29):

$$\left.\begin{aligned} E_b &= E_{ge}+E_p+E_a \\ &= m_b c^2\gamma_s-\frac{1}{2}E_{f\,ge}+m_b\,\wp_s \end{aligned}\right\}. \qquad (35)$$

If in (35) we neglect the product $m_b\,\wp_s$ due to the small pressure on the body surface and disregard the rest energy $m_b c^2\gamma_s$, then the energy value remains, which is equal to:

$$W=-\frac{1}{2}E_{fge}=-\frac{3G\,m_b^2}{10a}+\frac{3q_b^2}{40\pi\varepsilon_0 a}.$$

In classical mechanics, in which the rest energy is not considered, the total energy of the gravitational and electromagnetic fields for a sphere with uniform distribution of mass and charge is equal to:

$$W_{ge}=-\frac{3G\,m_b^2}{5a}+\frac{3q_b^2}{20\pi\varepsilon_0 a}.$$

According to the virial theorem, it is considered that the internal kinetic energy should equal half the absolute value of the energy of fields: $W_i=-\frac{1}{2}W_{ge}$. The total energy is composed of the energy of fields and the internal energy:

$$\left.\begin{aligned} W &= W_i+W_{ge}=\frac{1}{2}W_{ge} \\ &= -\frac{3G\,m_b^2}{10a}+\frac{3q_b^2}{40\pi\varepsilon_0 a} \end{aligned}\right\}. \qquad (36)$$

This shows that the total energy W in classical mechanics coincides with the relativistic energy (35), if we exclude from the latter the rest energy and the energy of the surface pressure. Thus, the transition is performed of the covariant theory of gravitation into classical mechanics. However, in classical mechanics, it is not determined how the internal pressure makes contribution to the mass and energy of the system.

We will now specify how in our model the virial theorem is realized, particularly for field energies and particle energies. We have the energy E_{fp} of the pressure field and the energy E_{fa} of the acceleration field, and the sum of these energies, according to (32), is equal to the absolute value of the sum of energies E_{fge} of the gravitational and electromagnetic fields. As a result, the sum of fields' energies is equal to zero.

The situation for the energies of particles in fields is different. The energy of a particle in the field in the absence of the vector potential is defined by the product of the mass (charge) by the scalar potential. The sum of the energies of particles in the gravitational and electromagnetic fields, according to (33), is equal to $-\frac{5}{2}E_{fge}$, the energy of particles in the pressure field is $m_b \wp_s + E_{fge}$ and the energy of particles in the acceleration field is $m_b c^2 \gamma_s + E_{fge}$. From the energy of particles in the pressure field, we can distinguish the energy E_{fge} and the energy E_{fge} – from the energy of particles in the acceleration field. But, the sum of these energies is $5/4$ times less than the absolute value $\left|-\frac{5}{2}E_{fge}\right| = \frac{5}{2}E_{fge}$ of the sum of energies of particles in the gravitational and electromagnetic fields. At the same time, the excess energy of particles in the gravitational and electromagnetic field, which is equal to $-\frac{1}{2}E_{fge}$, is compensated by the fact that the gravitational mass energy of the system increases from Mc^2 to $m_b c^2 \gamma_s$.

Relation with the Cosmological Constant

In [1], we obtained a relation that connects the cosmological constant Λ with the 4-potentials of fields, which are included in the Lagrangian:

$$\left.\begin{aligned} 2ck\Lambda &= -2u_\mu J^\mu - 2D_\mu J^\mu \\ &\quad - 2A_\mu j^\mu - 2\pi_\mu J^\mu \end{aligned}\right\}. \qquad (37)$$

Let us expand the products of 4- vectors:

$$u_\mu J^\mu = \hat{\gamma}\rho_0(\vartheta - \mathbf{v}\cdot\mathbf{U}),$$

$$D_\mu J^\mu = \hat{\gamma}\rho_0(\psi - \mathbf{v}\cdot\mathbf{D}),$$

$$A_\mu j^\mu = \hat{\gamma}\rho_{0q}(\varphi - \mathbf{v}\cdot\mathbf{A}),$$

$$\pi_\mu J^\mu = \hat{\gamma}\rho_0(\wp - \mathbf{v}\cdot\mathbf{\Pi}).$$

Here, $J^\mu = \rho_0 u^\mu$ is the mass 4-current; $j^\mu = \rho_{0q} u^\mu$ is the charge (electromagnetic) 4-current; $\mathbf{U}$, $\mathbf{D}$, $\mathbf{A}$ and $\mathbf{\Pi}$ denote the vector potentials of the acceleration field, gravitational and electromagnetic fields and pressure field, respectively; and we use the approximation of the special theory of relativity, in which $u^\mu = (\hat{\gamma}c, \hat{\gamma}\mathbf{v})$, where $\hat{\gamma} = \frac{1}{\sqrt{1 - v^2/c^2}}$, $\mathbf{v}$ is the velocity of motion of the body's arbitrary particle.

Let us consider the situation in the reference frame K', which is stationary relative to the body in question. In K', the particle velocities are equal to $\mathbf{v}'$ and the Lorentz factor $\gamma' = \frac{1}{\sqrt{1 - v'^2/c^2}}$ should be used instead of $\hat{\gamma}$. As a result, (37) can be rewritten as follows:

$$\left.\begin{aligned} -ck\Lambda &= \gamma'\rho_0(\vartheta - \mathbf{v}'\cdot\mathbf{U}) \\ &\quad + \gamma'\rho_0(\psi - \mathbf{v}'\cdot\mathbf{D}) \\ &\quad + \gamma'\rho_{0q}(\varphi - \mathbf{v}'\cdot\mathbf{A}) \\ &\quad + \gamma'\rho_0(\wp - \mathbf{v}'\cdot\mathbf{\Pi}) \end{aligned}\right\}. \qquad (38)$$

In relation (38), the cosmological constant Λ has its own value for each particle of the body. We intend to integrate (38) over the volume of the body in the form of a fixed sphere, which is filled with moving particles as tightly as possible, and which has uniform density of mass and charge in the entire volume of the sphere. In the absence of general rotation or directed matter flows, the particles' velocities $\mathbf{v}'$ are directed randomly in different directions. Then, after integrating (38), the contribution of vector products containing $\mathbf{v}'$ will be zero, and the total vector potentials $\mathbf{U}$, $\mathbf{D}$, $\mathbf{A}$ and $\mathbf{\Pi}$ inside the sphere will be zero as well. Therefore, the integral of (38) over the volume is as follows:

$$\left.\begin{aligned} -\int ck\Lambda\, dx^1 dx^2 dx^3 &= m'c^2 \\ = \int \begin{pmatrix} \gamma'\rho_0\vartheta + \gamma'\rho_0\psi \\ +\gamma'\rho_{0q}\varphi + \gamma'\rho_0\wp \end{pmatrix} & dx^1 dx^2 dx^3 \end{aligned}\right\}.$$

The quantity $-ck\Lambda$ in our opinion is the energy density of each particle, and the integral of this density over the volume gives a certain energy constant $m'c^2$, which is associated with all the particles of the system. In the right side of the equation, there is the integral that we have already calculated in (12). With this in mind, we can write:

$$\left.\begin{aligned} m'c^2 = mc^2\gamma_c^2 - \frac{3\eta m^2\gamma_c^2}{5a} \\ -\frac{3G\,m^2\gamma_c^2}{2a} + \frac{3q^2\gamma_c^2}{8\pi\varepsilon_0 a} \\ + m\,\wp_c\gamma_c - \frac{3\sigma m^2\gamma_c^2}{10a} \end{aligned}\right\}. \qquad (39)$$

If we compare (39) with (21), we see that the quantity $m'c^2$ is part of the relativistic energy E_b of the system and denotes the sum of energy components of the particles under the influence of fields. The energy E_b also includes the energy components associated with the fields themselves. But according to (23) in case of a spherical body, all these components cancel each other. Therefore, we can assume that for a sphere $E_b = M\,c^2 = m'c^2$ and $M = m'$.

In (39), the mass m' is some constant mass, which denotes the total mass of body particles, excluding the contribution from the mass-energy of macroscopic fields associated with this body. If we divide the total body matter by particles and scatter them from each other to infinity, then for the matter at rest there will be no electromagnetic and gravitational fields associated with the interaction of these particles with each other. There will be no internal pressure from the particles' influence on each other. In this case, with regard to (38) written for a single particle, the mass m' will consist of the total mass of all the particles in view of the energy of particles' proper fields, the energy of their internal pressure and the internal kinetic energy. We considered such mass in [4] as the total mass of the body parts, scattered from each other and located at infinity at zero absolute temperature. At infinity, $\gamma' = 1$, $\vartheta = c^2$ and then the system's mass M turns into the mass m'.

From (29-30), it follows that the system mass is less than the body mass: $M < m_b$, and the body mass m_b is equal to the gravitational mass m_g. Since the mass m' is constant and associated with the cosmological constant, and $M = m'$, it turns out that the gravitational mass $m_g = m_b$ of the system in (29) can change, when in the system there is a change in the energy of the pressure field or the energy of the electromagnetic and gravitational fields. From (28), we find that $m < m_b$, and M is in the middle between m and m_b. As a result, the ratio of the masses is as follows:

$$m < m' = M < m_b = m_g\,. \qquad (40)$$

Discussion of Results

The Masses

According to (40), in the weak field the inertial mass M of the system in the form of a sphere with particles, taking into account the field energies, the internal pressure and the internal kinetic energy, can be described either by formula (29) or by the system mass m' from (39). The equality $M = m'$ means conservation of the system's energy, regardless of whether the system's parts are at infinity and do not interact with each other, or these parts come into close contact and form a coupled system. This is possible in case of ideal spherical collapse, when there are no emission and matter ejections from the system at any stage of the collapse or the matter accumulation. We discussed this question in [2] in connection with the problem of energy in spherical supernova collapse. There, we explained the possibility of low energy emission by neutrinos based on the fact that almost all the work of the gravitational forces during the matter compression can come on increasing the kinetic energy of the stellar matter motion and the pressure energy, as well as on creating the internal pressure gradients and particle's velocities.

Earlier in [5], we found the expression for the masses, which differs from (40): $m' < M < m = m_b = m_g$. We can explain this by a different accepted gauge of the cosmological constant – in this paper we use the formulae obtained with the gauge according to [1] – which differs from the gauge in [5]. Also, we are currently using for analysis another physical system in the form of a sphere, consisting of a set of particles moving inside the sphere, which are held together by gravitation. In such a system, inevitably there is difference between the masses m and m_b as a consequence of the radial gradient of the Lorentz factor γ' inside the sphere and as a consequence of the difference between the density ρ_0 of the particles in the reference frame K_p and the density ρ_b of particles from the standpoint of the reference frame K', associated with the system's center of mass. The mass m in (40) in its meaning has technical nature, since it is determined only mathematically by multiplying the density ρ_0 by the sphere's volume. We will note that the density ρ_0 is included in the system's Lagrangian with the 4-vector of the gravitational (mass) current density in the form $J^{\mu} = \rho_0 u^{\mu}$. The density ρ_0 is also included in the equation of motion of a point particle and in the field equations in [1].

According to (29) and (40), the mass m_g is greater than the mass M. This means that the gravitational mass of the system is always greater than the inertial mass of the system by half of the absolute value of the gravitational and electromagnetic field energy minus the mass-energy of the surface pressure.

According to (40), the gravitational mass m_g is also greater than the mass m' of the system's parts, scattered to infinity. We can explain this in the following way. As we know, for a ball, the absolute value of the potential energy of the gravitational field is equal to the total work on the matter transfer from infinity to the surface and inside the ball. It is assumed that the ball is formed by gradual growth due to layering of spherical shells as the matter is transferred. But, beside the fact that the matter is transferred from infinity inside the body, which results in an increase of the absolute value of the potential energy of the body's gravitational field, the force of gravitation performs other actions; it increases the kinetic energy of the particles inside the body as well as the energy of the particles' pressure on each other and creates the gradients of pressure and kinetic energy of the particles inside the body. All these types of work of the gravitation force on the body formation increase the body mass from m' to m_g. The main contribution to the gravitational mass increase is made by the emerging motion; at infinity the particles were stationary, but inside the body the particles move at velocities $\mathbf{v}'$.

If we consider the virial theorem, connecting half the absolute value of gravitational and electromagnetic energies with the internal energy of the body, then it turns out that half of the work of the gravitational and electromagnetic fields on the body formation is transformed into the internal energy of the body. The total energy W of the body, according to (36), is negative and with the help of it (35), (39) and (29) can be written as follows:

$$E_b = M c^2 = m_b c^2 \gamma_s + W + m_b \wp_s = m' c^2 . \quad (41)$$

Since W is equal to half the sum of the gravitational and electrical energies, then we can see that half of the work of the gravitational and electromagnetic fields on the body formation is transformed into the mass increase from $M = m'$ to the value $m_b = m_g$.

From the virial theorem, the approximate equality follows between the absolute value of the total system's energy W (36), the internal body energy W_i and the binding energy, if we define it in (41) as the difference between the rest energy $m_b c^2 \gamma_s + m_b \wp_s$ for the mass m_b and the rest energy of the initial state at infinity $m'c^2$. However, in usual interpretation of the binding energy it is not so, since the binding energy is defined as the difference between the total energy of the individual parts of the system and the energy of the system made up of these parts into a whole. This definition of the binding energy in this case gives us the relation: $m'c^2 - M c^2 = 0$; i.e., in case of ideal spherical collapse, the system's energy at the beginning and the end of the process is the same and the binding energy is equal to zero. Despite the equality of the binding energy to zero, the system does not fall apart, because the masses are always attracted. The total energy W (36) of the system remains negative.

The invariant mass M of the system is the measure of inertia of the system as a whole and the measure of the relativistic energy of the system. This means that the system's acceleration under the influence of forces should depend on the mass M. The mass m_b can be calculated as the integral of the density ρ_b over the volume of the sphere. The gravitational mass m_g is equal to m_b and can be determined by means of gravitational experiments near the body on the gravitational effect on the test bodies. According to (31), at an infinitely large radius of the body, the mass of the spherical system $M = m'$ becomes equal to the gravitational mass of the body $(m_b = m_g)_\infty$. Equation (31) can be regarded as the quadratic equation to determine the gravitational mass m_g depending on the body radius a, on its electrical charge q_b and the total mass of the fixed parts of this body $m' = M$, when these parts are motionless and infinitely distant from each other:

$$m_g \approx \frac{1}{\gamma_s + \frac{\wp_s}{c^2}} \left(M - \frac{3q_b^2}{40\pi \varepsilon_0 a c^2} \right).$$

Energies and Masses in the General Theory of Relativity

In the general theory of relativity (GTR), the system's mass M is considered to be less than the total mass of the body's parts m' [6-7]. In GTR, there is gravitational mass of the system from the standpoint of a distant observer, calculated as the volume integral of the sum $nM_N + e$, where n is the concentration of matter nucleons, M_N is the mass of one nucleon, e is the density of the body's internal mass-energy [8]. The inertial mass of the system is also considered, which is calculated with the volume integral of the timelike component of the stress-energy tensor, which is then divided by the square of the speed of light and equated to the gravitational mass based on the principle of equivalence. Accordingly, to determine the system's mass M we need either to know the internal energy of the body which is not precisely known, or use the stress-energy tensor, which however does not include the gravitational field energy in principle. The latter is due to the fact that in GTR the gravitational field is understood as a metric field and is described by the stress-energy pseudotensor. As a result, calculation of the relativistic energy and the system's mass in GTR is much more difficult and involves a number of conditions. For example, for calculating the energy the coordinates of the reference frame at infinity should transfer into the coordinates of Minkowski space.

The mass of the system, with regard of the gravitational and electromagnetic fields, according to [6] and [9], in GTR in the weak field in our notation relative to the mass, density and radius of the body is equal to:

$$\left.\begin{aligned} &\int T^{00} dV = M \\ &= \frac{1}{c^2} \int \left(\begin{aligned} &\rho_b c^2 + \rho_b \Pi + \rho_b \psi \\ &+ \frac{1}{2} \rho_b v^2 + \rho_{bq} \varphi - \frac{1}{2} \varepsilon_0 E^2 \end{aligned} \right) dV \\ &= m_b + \frac{1}{c^2} E_k - \frac{6G m_b^2}{5ac^2} \\ &\quad + \frac{3q_b^2}{20\pi \varepsilon_0 a c^2} + \frac{1}{c^2} \int \rho_b \Pi dV , \end{aligned} \right\} \quad (42)$$

where T^{00} is the mass tensor, turning after multiplying by the square of the speed of light into the stress-energy tensor of the system; the body mass $m_b = \int \rho_b \, dV$; ρ_b and ρ_{bq} are the density of mass and charge, respectively; $E_k = \frac{1}{2} \int \rho_b v^2 \, dV$ is the kinetic energy; Π is the pressure energy per unit mass, and the case of uniform density is considered.

In [6] also the invariant mass density ρ^* is used, which implies such mass density, which does not change under the influence of the pressure or gravitational field. It is assumed that such invariant density ρ^* is part of the continuity relation in the curved spacetime: $\partial_\alpha (\sqrt{-g}\, \rho^* u^\alpha) = 0$, here g is the determinant of the metric tensor, u^α is the 4-velocity. We will note in this regard that in the covariant theory of gravitation, the continuity relation is written not for ρ^* but for ρ_0 [1], and ρ_0 can vary and depend on any factors, including the pressure and gravitational field.

In the weak field for the fixed body in GTR may be written:

$$\rho^* = \rho_b \left(1 - \frac{v^2}{2c^2} + \frac{3\psi}{c^2} \right). \qquad (43)$$

We will assume that $E_k = \frac{3Gm_b^2}{10ac^2} - \frac{3q_b^2}{40\pi \varepsilon_0 a c^2}$, as it should be expected due to virial theorem. If we substitute (43) into (42), we obtain the relation: $m^* < M < m_b$, so that the mass M of the system is greater than the mass $m^* = \int \rho^* \, dV$. After substituting (43) into (42), we obtain the expression for the mass-energy of the system, which is similar to those presented in [7] and [10] (in contrast to [6], in [10] ρ is an invariant density and ρ^* denotes the mass density corresponding to our density ρ_b).

We will assume that the mass of the system in (42) according to GTR is calculated precisely and is equal to our mass of the system in (31):

$$\left.\begin{aligned} M &= m_b + \frac{1}{c^2} E_k - \frac{6G\, m_b^2}{5ac^2} \\ &\quad + \frac{3q_b^2}{20\pi \varepsilon_0 ac^2} + \frac{1}{c^2}\int \rho_b \Pi dV \\ &= m_b \left(\gamma_s + \frac{\wp_s}{c^2} \right) - \frac{3G\, m_b^2}{10ac^2} \\ &\quad + \frac{3q_b^2}{40\pi \varepsilon_0 ac^2} \end{aligned}\right\}. \qquad (44)$$

From the left side of (44), we see that in GTR the gravitational energy is included in the equation with the increased weight relative to the electromagnetic energy, and in the right side both energies have the same weight due to the similarity of equations for the fields. This is due to the fact that in GTR the gravitational field is replaced by the effect of the action of the metric field of the metric tensor. As a result, the entire metric contains gravitation and the electromagnetic field and pressure remain independent.

If we neglect the contribution of $\gamma_s + \frac{\wp_s}{c^2}$ to (44) and consider this quantity as a unity, then with regard to the expression $E_k = \frac{3Gm_b^2}{10ac^2} - \frac{3q_b^2}{40\pi\varepsilon_0 ac^2}$ from (44), we can estimate the pressure energy in GTR:

$$\int \rho_b \Pi dV = \frac{3Gm_b^2}{5a}.$$

In (42), the mass M of the system due to the equivalence principle is considered equal to the gravitational mass. This means that in GTR a charged body increases its gravitational mass. Based on the statement above, the ratio of masses in GTR is as follows:

$$m^* < m < M = m_g < m_b < m', \qquad (45)$$

where in the first approximation $m' = N m_n$ (here N is the number of nucleons in the body, m_n is the mass of a nucleon), $M = m' - W_i$ (M is the mass of the system in the form of the body and its fields, W_i is the internal energy in (36)), the mass M is equal to the gravitational mass m_g, the mass m^* is determined by the integral over the volume of the invariant density ρ^* (43), the mass m_b is calculated by integrating over the volume of the body density ρ_b, and the mass m is determined by us in (28) with the help of m_b and has technical nature.

If the mass of the system decreases from the value m' to M, then there is excess energy of the order of W_i. In GTR, the collapsing system must radiate this energy, so that the ideal spherical non-radiating collapse in GTR is impossible [8].

As we can see, relation (45) for the masses in GTR differs significantly from relation (40) for the masses in the covariant theory of gravitation.

Conclusion

According to (32), the total energy of the gravitational and electromagnetic fields summed up with the energy of the acceleration field and the energy of the pressure field inside the spherical body is equal to zero. During the body formation, distribution of energies of the body particles takes place in the potentials of all the four fields. This leads to the kinetic energy of the motion of particles, to the internal pressure and the energy of particles in the gravitational and electromagnetic fields.

The difference of our approach from the results of GTR is that the mass of the system in the ideal spherical collapse does not change, $m' = M$. Really, if at the beginning of the ideal collapse the spatial component of the total 4-momentum of the particles falling on the center of mass is equal to zero due to the spherical symmetry, the same will take place at the end of the collapse, so that the mass-energy, which is part of the time component of 4-momentum, may be conserved. However, the gravitational mass m_g is greater than the mass M of the system, since the state of the particles changes; they start moving inside the system and exert pressure on each other. Besides, the particles acquire additional energy in the internal fields.

If the system contains the electromagnetic field, its influence on the mass m_g is opposite to the influence of the gravitational field; i.e., the electromagnetic field must reduce the gravitational mass m_g. We can calculate that if a body with the mass of 1 kg and the radius of 1 meter is charged up to the potential of about 5 megavolt, it must reduce the gravitational mass of the body (not including the mass of the additional charges) at weighing in the gravity field by 10^{-13} mass fraction, which is close to the present day accuracy of mass measurement.

References

[1] Fedosin, S.G., vixra.org, 5 Mar 2014.

[2] Fedosin, S.G., American Journal of Modern Physics, 3(4) (2014) 152.

[3] Fedosin, S.G., Advances in Physics Theories and Applications, 23 (2013) 19.

[4] Fedosin, S.G., Canadian Journal of Physics, 92(10) (2014) 1074.

[5] Fedosin, S.G., Advances in Natural Science, 5(4) (2012) 55.

[6] Fock, V.A., “The Theory of Space, Time and Gravitation”, (Pergamon Press, London, 1959).

[7] Papapetrou, A., Proc. Phys. Soc. A, 64 (1951) 57.

[8] Abhas, M., Phys. Rev. D, 74 (2006) 024010.

[9] Landau, L.D. and Lifshitz, E.M., “The Classical Theory of Fields”, Vol. 2, 4th ed., (Butterworth-Heinemann, 1975).

[10] Chandrasekhar, S., Ap. J., 142 (1965) 1488; Ap. J., 158 (1969) 45.

Volume 8, Number 1, 2015. pp. 17-27

Jordan Journal of Physics

ARTICLE

Dose from Naturally Occurring Radium Radioactivity in Abstracted Disi Fossil Groundwater*

Saed Dababneh

Department of Physics, Faculty of Science, Al-Balqa Applied University, P.O. Box 2587, Amman 11941, Jordan.

Received on: 21/5/2014; Accepted on: 28/8/2014

Abstract: The radium activity concentration data measured by Vengosh *et al.* [1] in water samples from the Disi aquifer are utilized to calculate the annual effective dose delivered to adult human consumers. Although the total activity in the Rum group in particular is significantly high compared to the very conservative World Health Organization WHO guidelines, the calculated average effective dose is slightly higher than the Jordanian standard and less than the corresponding value in the Australian guidelines. Blending models are suggested which reduce the dose and its associated risks. The results reveal the radiological quality of the indispensable Disi drinking-water to be satisfactory for consumption in a water-poor part of the World.

Keywords: Radioactivity; Disi aquifer; Disi conveyance project; Groundwater; Dose; Risk assessment.

PACS: 89.60.-k; 92.40.Kf; 92.40.kh; 92.40.kc; 67.63.-r; 67.80.F-

Introduction

Although Mediterranean countries are diverse in their socio-economic development, infrastructure, climate and water availability, the region as a whole is undergoing rapid social and environmental changes which may harbor negative implications for future sustainability [2]. Water scarcity is anticipated to become an even greater regional problem in the near future, as the population grows and climate change potentially makes precipitation more uncertain and variable. Jordan, in particular, has already one of the lowest levels of water resource availability per capita in the World. Management of water resources is therefore a key issue facing national government authorities [3, 4].

In July 2013, Jordan began pumping water from the southern fossil aquifer of Disi. A $990 million project started in 2009 which involves digging 55 wells and piping water supplies 325 kilometers to the capital city Amman, as well as to other governorates in the country. The lifespan of this non-renewable water conveyance project is estimated at 20-30 years, if abstraction rates are kept at around 100 mcm each year. The project hence provides a provisional solution to a long-term problem, but provides Jordan with enough time to consider other options like desalination [3]. Therefore, the Disi resource is of vital importance to the country, especially amid the unrest in the region which imposes direct multifold impacts on Jordan, one of which is related to hosting significant numbers of refugees.

In 2009, a study by Vengosh *et al.* [1] was conducted aiming at understanding how salinity is correlated with radioactivity in groundwater, to evaluate the sources of radium in the Disi aquifer, to investigate the possible mechanisms of radium mobilization from the host aquifer rocks and to evaluate the impact of this phenomenon on future water utilization from similar aquifer basins in the Middle East.

---

* A new analysis of the Vengosh *et al.* [1] data.

Corresponding Author: Saed Dababneh **Email**: dababneh@bau.edu.jo

Though the high radium content in the Disi aquifer in Central Jordan is hypothetically correlated to its high salinity, Vengosh *et al.* noticed that the corresponding high radioactivity in the Rum Group is associated with low-saline groundwater. In addition, this finding cannot be explained by anomalous radium content in the host aquifer rocks which are not different from those of other worldwide sandstone rocks.

The study ultimately revealed the Disi water to be highly radioactive, thus surrounding the Disi conveyance project with controversy. The paper [1] reported the combined ^{226}Ra and ^{228}Ra activities to be much higher than international drinking water standards. The reported data raised concerns over the safety of Disi and similar nonrenewable groundwater reservoirs, intensifying the already severe water crisis in the region. That important paper was cited in different reports [*e.g.* refs. 5-8] in addition to local and international media and became the focus of attention for a continued debate over the indispensable Disi conveyance project.

The activity concentration of three α-emitting isotopes of radium; namely ^{223,224,226}Ra, in addition to the β-emitting ^{228}Ra, were measured by Vengosh *et al.* [1] in thirty-seven groundwater samples collected, at different dates, from wells in the sandstone Disi aquifer. The study covered the Rum Group aquifer [9], the Khreim Group in Disi-Mudawwara [10] and areas in Central Jordan. The current work aims at a further analysis of the same raw data reported in Table 1 of the Vengosh *et al.* paper. In addition to radioactivity concentration, this work evaluates the committed effective annual dose from the four radium isotopes measured by Vengosh *et al.*. The results are then discussed in the framework of national and international guidelines and standards. The associated risks are finally assessed.

Results and Discussion

The hydrogeological nature of the Vengosh *et al.* [1] study did not require the calculation of the corresponding effective dose delivered to consumers. Therefore, Table 1 of the Vengosh *et al.* paper only lists the measured activity concentration (in Bq/l) for the four radium isotopes. Although the table compares these activity concentration values to the corresponding international requirements and guidelines, no dose calculation at that stage was implied by the objectives of the study.

In order to complement that earlier research, the quantity of interest in this work becomes the committed effective annual dose. It is calculated from the individual radionuclide concentration and the corresponding dose coefficient [11] for adults, assuming annual consumption of 730 liters [12]. The total dose is calculated as:

$$\left.\begin{aligned} &D_{Total}(mSv/a) = \\ &\sum_i D_i(mSv/a) = \\ &\sum_i A_i(Bq/l)\times 730(l/a)\times C_i(mSv/Bq), \end{aligned}\right\} \quad (1)$$

where D_i is the dose from a given isotope i, A_i is the activity concentration for each isotope as measured by Vengosh *et al.*, while the dose conversion coefficients C_i (Table 1) are obtained from the International Commission on Radiological Protection ICRP 2012 report [11], which are also adopted by the World Health Organization [12]. These dose coefficients account for radiation and tissue weighting factors, in addition to relevant metabolic information.

TABLE 1. The dose conversion coefficients for the four radium isotopes [11].

Isotope	C_i (mSv/Bq)
^{223}Ra	1 x 10^{-4}
^{224}Ra	6.5 x 10^{-5}
^{226}Ra	2.8 x 10^{-4}
^{228}Ra	6.9 x 10^{-4}

Data in Table 2 of this work was calculated using the corresponding data in Table 1 of Vengosh *et al.*. For each of the investigated wells, regular font data in the table are related to activity concentration, while bold font data are dose-related values. Private communication with the Water Authority of Jordan WAJ indicated that water currently pumped from the wells arrive at the reservoirs after a minimum period of 2.7 days. Though this period does not include an additional time to reach households through the distribution network, the 2.7 days period was adopted for a conservative estimate of the decay of the relatively short lived radium isotopes; namely ^{223}Ra and ^{224}Ra, with half-life times $T_{1/2}$ of 11.435 and 3.66 days [13], respectively.

Obviously, no significant decay is expected for the other two isotopes ($T_{1/2}(^{226}Ra)$=1600 years and $T_{1/2}(^{228}Ra)$=5.75 years [13]). Consequently, the activity concentration values in Table 2 (regular font) for ^{223}Ra and ^{224}Ra differ from the corresponding values in Vengosh *et al.*. In addition to these activity concentration values A_i, the corresponding dose from each isotope D_i (Eq. 1) is also tabulated in boldface.

It is evident that though the relative contribution of ^{224}Ra (a progeny of the relatively high abundant ^{232}Th) to the total activity concentration, and in general to the gross alpha activity, is significant (Table 1 in Vengosh *et al.*), its short half-life together with its relatively small conversion coefficient C_i (Table 1) cause its contribution to the total dose to diminish (Table 2 and Fig. 1). In addition, the activity concentration of ^{223}Ra, being a progeny of the much less abundant ^{235}U, is obviously small. This fact, together with its short half-life and relatively small C_i, yield a negligible contribution of this radium isotope to the total dose (Fig. 1). Table 2 and Fig. 1 reveal the fact that ^{228}Ra, being a progeny of ^{232}Th with long half-life and large C_i, dominates in terms of its contribution to the total dose. Finally, ^{226}Ra, a daughter in the ^{238}U decay series, contributes significantly to the total dose for reasons qualitatively similar to those related to ^{228}Ra, but with quantitatively smaller effect. In the above discussion, the half-life affects the dose in terms of the decay during the period between water withdrawal and consumption. On the other hand, the four radionuclides under consideration have the same biological half-life, and the reverse effect of decay half-life is accounted for by the dose conversion factors C_i.

The total activity concentration (in the reservoirs) and the corresponding dose value are calculated and listed in the seventh column of Table 2. The activity concentration screening levels of 0.5 Bq/l for gross alpha activity and 1 Bq/l for gross beta activity as set by the WHO [12] are obviously exceeded. Consequently, the dose from individual radionuclides should be considered (Fig.1). The total dose from the four Ra isotopes for each Disi aquifer group are histogrammed in Fig. 2. Obviously, the dose from the Rum Group as well as from Central Jordan wells is high compared to the 0.1 mSv/a recommended in the WHO Guidelines [12].

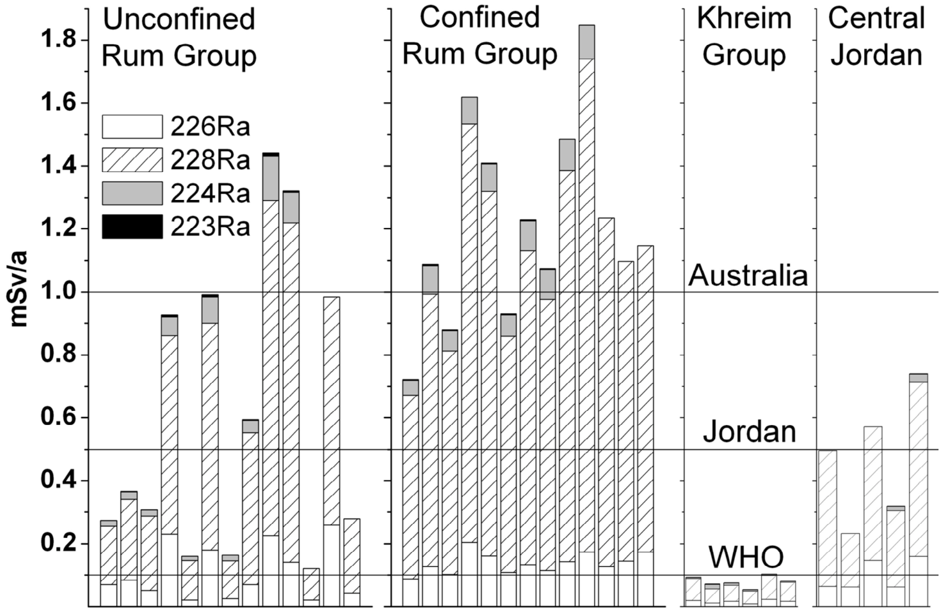

FIG. 1. The dose contribution of the four radium isotopes for each of the Disi aquifer groups. A conservative delay period of 2.7 days for water pumped from each well to reach the collection/mixing reservoir has been assumed.

TABLE 2. The data are based on data in Table 1 of Vengosh *et al.* [1]. The activity concentration after a conservative conveyance delay period of 2.7 days has been calculated for the four radium isotopes, together with the corresponding dose. The total dose is compared to the WHO guideline value of 0.1 mSv/a, to the Jordanian standard of 0.5 mSv/a, as well as to the Australian guideline of 1 mSv/a.

Area and well name	Well ID	^{226}Ra Bq/L **mSv/a**	^{228}Ra Bq/L **mSv/a**	^{224}Ra Bq/L **mSv/a**	^{223}Ra Bq/L **mSv/a**	Total Bq/L **mSv/a**	WHO Activity %[a] **Dose %**[b]	Jordanian **Dose %**[b]	Australian **Dose %**[b]
				Unconfined Rum Group					
Sahl El Suwan SS-6	ED1506	0.34	0.37	0.37	0.009	1.09	442		
		0.0695	**0.1864**	**0.0176**	**0.0007**	**0.2742**	**274**	**55**	**27**
Sahl El Suwan SS-5A	ED1505	0.41	0.51	0.51	0.023	1.45	604		
		0.0838	**0.2569**	**0.0242**	**0.0017**	**0.3666**	**367**	**73**	**37**
M 14 (Rum Co.)	ED1612	0.25	0.47	0.40	0.017	1.13	536		
		0.0511	**0.2367**	**0.0188**	**0.0012**	**0.3079**	**308**	**62**	**31**
Sahl El Suwan SS-4	ED1504	1.13	1.25	1.26	0.082	3.72	1497		
		0.2310	**0.6296**	**0.0598**	**0.0060**	**0.9264**	**926**	**185**	**93**
M 4 (Rum Co.)	ED1623	0.10	0.25	0.28	0.010	0.64	289		
		0.0204	**0.1259**	**0.0134**	**0.0007**	**0.1605**	**160**	**32**	**16**
SS20 (Sahl El Suwwan)	ED1614	0.88	1.43	1.77	0.103	4.18	1705		
		0.1799	**0.7203**	**0.0840**	**0.0075**	**0.9916**	**992**	**198**	**99**
M 5 (Rum Co.)	ED1624	0.12	0.24	0.38	0.010	0.75	291		
		0.0245	**0.1209**	**0.0179**	**0.0007**	**0.1641**	**164**	**33**	**16**
Mneisheer M6	ED1540	0.34	0.96	0.81	0.036	2.15	1079		
		0.0695	**0.4836**	**0.0384**	**0.0026**	**0.5941**	**594**	**119**	**59**
SS24 (Sahl El Suwwan)	ED1608	1.11	2.11	2.99	0.135	6.35	2534		
		0.2269	**1.0628**	**0.1420**	**0.0099**	**1.4416**	**1442**	**288**	**144**
Mneisheer W-2 /M 8	ED1402	0.69	2.14	2.07	0.062	4.96	2422		
		0.1410	**1.0779**	**0.0982**	**0.0045**	**1.3217**	**1322**	**264**	**132**
Qa Abu Suwana M2	ED1509	0.10	0.20			0.30	210		
		0.0204	**0.1007**			**0.1212**	**121**	**24**	**12**
Qa Disi well no. 3	QD3	1.27	1.44			2.71	1567		
		0.2596	**0.7253**			**0.9849**	**985**	**197**	**98**
Quweirah well no. 3	S5	0.21	0.47			0.68	491		
		0.0429	**0.2367**			**0.2797**	**280**	**56**	**28**
				Confined Rum Group					
Gramco G 6	K1034	0.43	1.16	1.00	0.031	2.62	1306		
		0.0879	**0.5843**	**0.0475**	**0.0022**	**0.7219**	**722**	**144**	**72**
Gramco G 3	K1031	0.62	1.72	1.91	0.058	4.31	1979		
		0.1267	**0.8664**	**0.0908**	**0.0042**	**1.0881**	**1088**	**218**	**109**

Area and well name	Well ID	^{226}Ra Bq/L **mSv/a**	^{228}Ra Bq/L **mSv/a**	^{224}Ra Bq/L **mSv/a**	^{223}Ra Bq/L **mSv/a**	Total Bq/L **mSv/a**	WHO Activity %[a] **Dose %[b]**	Jordanian **Dose %[b]**	Australian **Dose %[b]**
Gramco G 4	K1039	0.50	1.41	1.34	0.031	3.28	1597		
		0.1022	**0.7102**	**0.0638**	**0.0023**	**0.8785**	**878**	**176**	**88**
Wafa 3	K1043	1.00	2.64	1.81		5.45	2921		
		0.2044	**1.3298**	**0.0857**		**1.6198**	**1620**	**324**	**162**
Wafa 2	K1028	0.79	2.30	1.82	0.047	4.95	2565		
		0.1615	**1.1585**	**0.0862**	**0.0034**	**1.4096**	**1410**	**282**	**141**
Wafa 1	K1027	0.53	1.49	1.42	0.048	3.49	1690		
		0.1083	**0.7505**	**0.0675**	**0.0035**	**0.9298**	**930**	**186**	**93**
Arab Agriculture Co. 1	K1016	0.65	1.98	2.00	0.053	4.69	2251		
		0.1329	**0.9973**	**0.0951**	**0.0038**	**1.2291**	**1229**	**246**	**123**
Arab Agriculture Co. 3	K1020	0.56	1.71	2.03	0.043	4.34	1973		
		0.1145	**0.8613**	**0.0962**	**0.0032**	**1.0751**	**1075**	**215**	**108**
Arab Agriculture Co. 6	K1026	0.70	2.47	2.07		5.24	2747		
		0.1431	**1.2441**	**0.0982**		**1.4854**	**1485**	**297**	**149**
Suleiman MarI El Ataneh	K3023	0.85	3.11	2.29		6.25	3424		
		0.1737	**1.5665**	**0.1084**		**1.8487**	**1849**	**370**	**185**
Al-Arabiya well no. 9	K1041	0.62	2.20			2.82	2262		
		0.1267	**1.1081**			**1.2349**	**1235**	**247**	**123**
Suleiman Abu Juweied		0.71	1.89			2.60	1961		
		0.1451	**0.9520**			**1.0971**	**1097**	**219**	**110**
			Khreim Group						
Al Hodood well	11S1	0.09	0.14	0.07	0.003	0.31	157		
		0.0184	**0.0705**	**0.0034**	**0.0002**	**0.0926**	**93**	**19**	**9**
Fawwaz Jeryes El Halaseh (BH9)	ED1602	0.05	0.09	0.30	0.017	0.46	127		
		0.0102	**0.0453**	**0.0142**	**0.0012**	**0.0710**	**71**	**14**	**7**
Hasan Salameh El Hawashleh 1	ED3009	0.08	0.10	0.16	0.009	0.35	125		
		0.0164	**0.0504**	**0.0077**	**0.0007**	**0.0751**	**75**	**15**	**8**
Mohammad Odeh El Njadat	ED3008	0.04	0.08	0.10	0.007	0.22	94		
		0.0082	**0.0403**	**0.0046**	**0.0005**	**0.0535**	**54**	**11**	**5**
Halet Ammar 2 (HA2)/W16	K3000	0.11	0.15	0.10	0.004	0.36	171		
		0.0225	**0.0756**	**0.0046**	**0.0003**	**0.1029**	**103**	**21**	**10**
Halet Ammar 2 (HA2)/W16	K3000	0.08	0.12	0.07	0.003	0.27	135		
		0.0164	**0.0604**	**0.0034**	**0.0002**	**0.0804**	**80**	**16**	**8**
			Central Jordan						
Lajjun deep well	Lajjun	0.31	0.86			1.17	891		
		0.0634	**0.4332**			**0.4966**	**497**	**99**	**50**

Area and well name	Well ID	^{226}Ra Bq/L **mSv/a**	^{228}Ra Bq/L **mSv/a**	^{224}Ra Bq/L **mSv/a**	^{223}Ra Bq/L **mSv/a**	Total Bq/L **mSv/a**	WHO Activity %[a] **Dose %[b]**	Jordanian **Dose %[b]**	Australian **Dose %[b]**
Potash well 2-TA2	DA1039	0.30	0.34			0.64	370		
		0.0613	**0.1713**			**0.2326**	**233**	**47**	**23**
Potash well 1-TA1	DA3023	0.72	0.84			1.56	912		
		0.1472	**0.4231**			**0.5703**	**570**	**114**	**57**
Potash well 1-TA1	DA3023	0.30	0.48	0.31	0.013	1.10	542		
		0.0613	**0.2418**	**0.0148**	**0.0009**	**0.3188**	**319**	**64**	**32**
Potash well 2-TA2	DA1039	0.78	1.10	0.52	0.024	2.42	1232		
		0.1594	**0.5541**	**0.0245**	**0.0017**	**0.7397**	**740**	**148**	**74**

[a] Percent values of the recommended activity concentration by the WHO [12]): [^{226}Ra activity + (^{228}Ra activity/0.1) + ^{224}Ra activity + ^{223}Ra activity] x 100;

[b] Percent values of the recommended dose.

TABLE 3. The average radium dose of the four Disi aquifer groups, their overall average and combinations of them. Blending with non-Disi waters with two different ratios could reduce the overall average dose to levels below the Jordanian limit.

	Dose (mSv/a)		
Group	Pure Disi	Mixing 1:1[a]	Mixing 2:1[b]
Unconfined Rum	0.61 ± 0.47	0.38 ± 0.23	0.46 ± 0.31
Confined Rum	1.21 ± 0.31	0.68 ± 0.16	0.86 ± 0.21
Khreim	0.08 ± 0.02	0.11 ± 0.01	0.10 ± 0.01
Central Jordan	0.47 ± 0.20	0.31 ± 0.10	0.36 ± 0.13
Average for all groups	0.59 ± 0.15	0.37 ± 0.07	0.45 ± 0.10
Ave. Rum and Khreim	0.63 ± 0.19	0.39 ± 0.09	0.47 ± 0.12
Ave. Rum	0.91 ± 0.28	0.53 ± 0.14	0.66 ± 0.19
Ave. Unconfined Rum and Khreim	0.34 ± 0.23	0.25 ± 0.12	0.28 ± 0.16

A conservative fixed non-Disi dose of 0.15 mSv/a was adopted [6], therefore: [a] the uncertainty is the statistical uncertainty of the Disi group(s) × $^{1}/_{2}$; [b] the uncertainty is the statistical uncertainty of the Disi group(s) × $^{2}/_{3}$.

In addition, and since consumption of radium in drinking water increases the risks for bone cancer and leukemia, it is important to note that “many” Rum-group wells exceed the derived concentration of 0.5 Bq/l (or 1 Bq/l) for ^{226}Ra and “most” Rum-group wells exceed the derived concentration of 0.2 Bq/l (or 0.1 Bq/l) for ^{228}Ra, as set by the European Union [14] (or in the WHO guidelines [12]). The combined ^{226}Ra and ^{228}Ra activities also exceed the US-EPA limit of 5 pCi/l [15]. Consequently, the committed effective annual dose from individual radionuclides should be considered (Fig.1). Obviously, the annual dose from the Rum-Group as well as from Central Jordan wells is high compared to the 0.1 mSv/a recommended in the WHO Guidelines. It is worth mentioning that in October 2013, the European Union [14] adopted the same WHO guideline value of 0.1 mSv/a. The above mentioned guidelines on activity concentration of 1 Bq/l and 0.1 Bq/l for ^{226}Ra and ^{228}Ra, respectively, are derived from this recommended dose of 0.1 mSv/a.

Nevertheless, the very same WHO report emphasizes the fact that "it is essential that each country reviews its needs and capacities in developing its regulatory framework". It also mentions that no international standards for drinking water quality are promoted for adoption, the main reason being "the advantage provided by the use of a risk-benefit approach, qualitative or quantitative, in the establishment of national standards and regulations". According to the report, the guidelines provide a scientific point of departure for national authorities to develop drinking water regulations and standards appropriate to the national situation. In particular, Chapter 9 of the WHO report that particularly discusses radiological aspects emphasizes that "screening levels and guidance levels are conservative and should not be interpreted as mandatory limits. Exceeding a guidance level should be taken as a trigger for further investigation, but not necessarily as an indication that the drinking-water is unsafe". The WHO report also emphasizes the fact that background radiation exposures vary widely across the Earth, but the average is about 2.4 mSv/a, with the highest local levels being up to 10 times higher without any apparent health consequences; 0.1 mSv therefore represents a small addition to background levels.

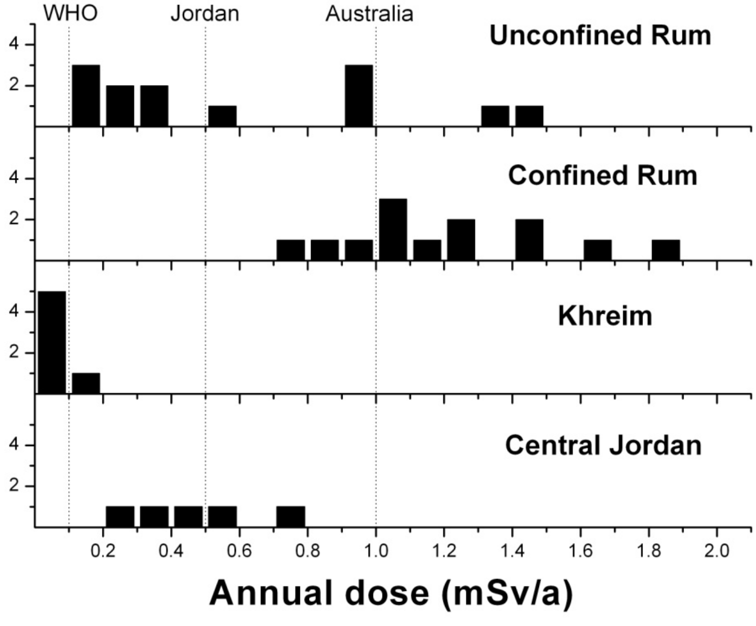

FIG. 2. A histogram of the radium dose from each well in the four Disi aquifer groups, compared to the WHO, Jordanian and Australian guidelines and standards.

In this context, the Australian National Water Quality Management Strategy report; namely the 2011 Australian Drinking-Water Guidelines [16], recommends a guideline dose of 1 mSv per year to be applied for radioactivity in drinking water. This is ten times the corresponding 2011 WHO value of 0.1 mSv/a [12]. The Australian document does not consider its recommended dose as a mandatory limit, but when exceeded, a decision on the need for and the degree of remedial action should be based on a cost-benefit analysis, and there may be circumstances where there is no practical alternative but to accept a dose that exceeds the guideline dose of 1 mSv/a. The Australian guideline value is based on earlier studies [17,18] on drinking water quality in areas dependent on groundwater. In Jordan, however, a mandatory regulation sets a standard of 0.5 mSv/a [19].

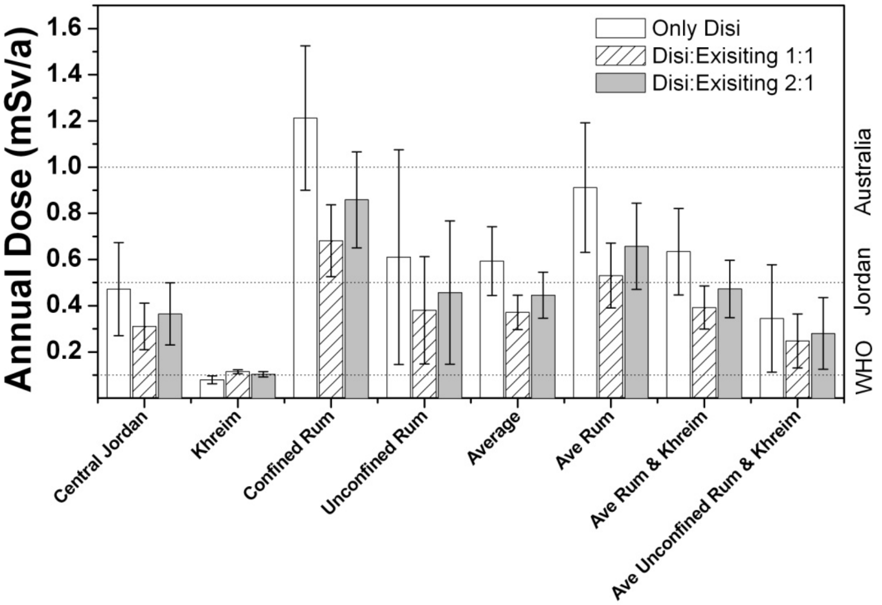

FIG. 3. Average radium dose according to two mixing models with non-Disi water with a conservative 0.15 mSv annual dose [6].

Therefore, in addition to the WHO guideline, both Australian guideline and Jordanian standard values are indicated in Figs. 1 and 2. The average dose from each group, together with its uncertainty, are depicted in the white column of Fig.3 (see Table 3). Water from the Khreim group could comply with the conservative WHO recommendation when the other less significant radionuclides are accounted for, while the average dose from Central Jordan wells could satisfy the Jordanian standard. The unconfined and confined Rum groups slightly exceed the Jordanian dose limit and the Australian guideline, respectively.

Needless to say, water treatment could considerably reduce radium concentration and hence the associated dose to levels well below the Jordanian standard. An alternative cost-effective solution is to develop a crude model for blending Disi ground-water with *e.g.* surface water in a reservoir in *e.g.* Amman. This is intended to provide an assessment, at least qualitatively, about the effectiveness of such mixing on reducing the dose in drinking water delivered to consumers. To make this model as conservative as possible, a dose value of 0.15 mSv/a will be adopted for the non-Disi resource [6]. Mixing ratios of Disi:Non-Disi =1:1 and 2:1 are considered (Table 3) and depicted in the shaded and gray columns of Fig. 3, respectively. According to such conservative models, a dose of less than the WHO guideline is definitely not achievable. Nevertheless, blending can reduce the dose well below the Jordanian standard.

Associated Risk Assessment

The linear-no-threshold LNT hypothesis [20-22] assumes that the demonstrated relationship between radiation dose and adverse effects at high levels of exposure can be linearly extrapolated to low levels relevant to drinking water, hence providing the "deliberately conservative" basis of radiation protection standards. Some evidence suggests that there may be a threshold below which no harmful effects of radiation occur. However, this is not yet accepted by radiation protection bodies as sufficiently well proven to be taken into official standards. Hence, the rather conservative LNT hypothesis is adopted in this assessment. Using LNT, the International Commission on Radiological Protection ICRP estimates the lifetime risk of a fatal cancer resulting from exposure to radiation to be 5×10^{-2} per Sv of annual radiation dose [16,23,24]. Fig. 4 depicts this linear relation in the relevant dose region of this study. On the basis of this estimate, a dose of 0.1 mSv per year gives a lifetime risk of about five additional fatal cancers per million people. The term "additinal fatal cancers" means incidences that occur in addition to those resulting from all other causes. The above discussion concentrated only on fatal cancer risks. The WHO documentation [12], on the other hand, considers the nominal probability coefficient for radiation-induced stochastic health effects, which include fatal cancer, non-fatal cancer and severe hereditary effects for the whole population to be 7.3×10^{-2} Sv^{-1} (which also refers to ICRP). Multiplying this by the annual dose yields the dashed line in Fig.4.

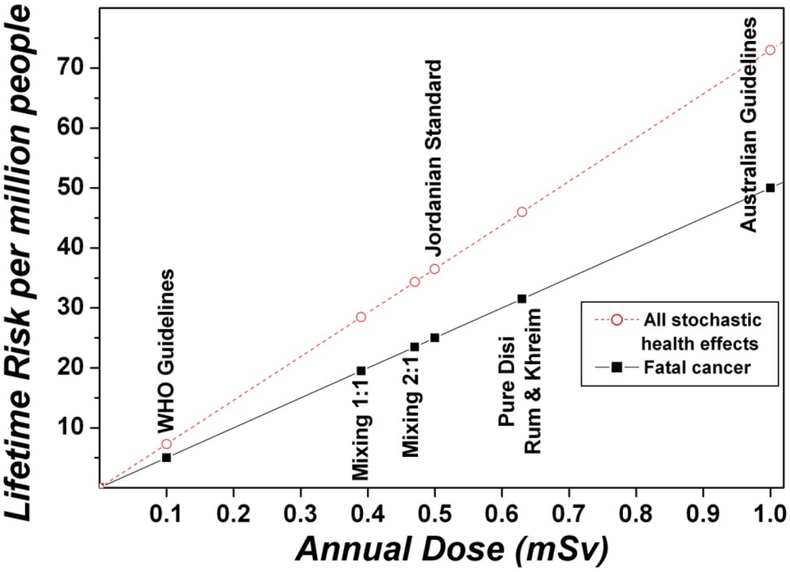

FIG. 4. Lifetime fatal cancer risks as well as all stochastic radiation-induced health effects per million people as a function of the annual radiation dose. Obviously, the conservative LNT hypothesis has been adopted. In calculating the average dose from pure Disi water, as well as for the two blending models, the Central Jordan wells have been excluded (Table 3), since water is assumed to be pumped from Rum- and Khreim-like wells.

It is worth emphasizing here that this study includes only radium isotopes. However, some guidelines and standards exclude radon and radon progeny, tritium, ^{14}C and ^{40}K from the calculation related to the limit of the total ingested dose. Among radon daughters, the β-emitter ^{210}Pb and α-emitter ^{210}Po with C_i values of 6.9×10^{-4} $mSvBq^{-1}$ and 1.2×10^{-3} $mSvBq^{-1}$, respectively, are worth particular attention. Though their dose conversion coefficients are high, being progenies of the gaseous radon, their corresponding activity concentration is remarkably low compared to radium in abstracted groundwater [7, 25]. The isotopic species in the natural decay series that belong to the elements thorium and protactinium can be neglected when groundwater safety is discussed, since both elements exhibit very poor aqueous solubility [26]. Uranium isotopes have relatively small C_i values [11]; namely 4.5×10^{-5} $mSvBq^{-1}$ for ^{238}U and 4.9×10^{-5} $mSvBq^{-1}$ for its grand-daughter ^{234}U (compare Table 1), and ^{235}U is poorly abundant. In general, uranium chemical toxicity is addressed separately.

Nevertheless, a comprehensive rigorous risk assessment should include all radionuclides; the above cited literature [*e.g.* ref. 7] indicates a possible conservative contribution of isotopes other than radium of about 5% to 25% to the total effective dose. Of particular importance is ^{210}Po [27]. Age-related doses should also be considered in a more comprehensive risk assessment. Finally, risk assessment should consider all radiological, chemical and biological factors, balanced against risks associated with deficiency in water supplies.

Conclusions and Recommendations

This work has been motivated by the necessity to provide further analysis of the data published by Vengosh *et al.* [1]. Though the author prepared a short comment on that paper, which has been recently published in the same journal [28], this work provides a more comprehensive analysis and discussion than provided in that short correspondence [28].

The results of this work reveal the radiological quality of the indispensable Disi drinking-water to be satisfactory for consumption in a water-poor part of the World, if risks are carefully managed. Blending ratios should take into consideration any possible buildup of the non-mobile ^{228}Th in the system, which could affect the ^{224}Ra concentration. Continuous and routine monitoring, including sample collection and measurement, is essential to ensure compliance with the local standards.

Transparency in the governmental water policies psychologically enhances the public acceptance. Practically, decision on blending ratios should always take into consideration the importance of reducing risk as much as reasonably achievable. However, the availability and quality of surface water, to a given blending reservoir, could be a limiting factor. Water treatment facilities, if found feasible, should be considered locally in regions with limited availability of surface water resources. Proposals for water desalination in the Gulf of Aqaba, which is intended to provide a more sustainable supply, can be considered as a future resource for blending which can take place on-site in the south, thus eliminating the necessity for regional blending. This scenario enables freeing surface water resources to be available to other usage.

References

[1] Vengosh, A., Hirschfeld, D., Vinson, D., Dwyer, G., Raanan, H., Rimawi, O., Al-Zoubi, A., Akkawi, E., Marie, A., Haquin, G., Zaarur, S. and Ganor, J., Environmental Science and Technology, 43 (2009) 1769.

[2] Iglesias, A., Garrote, L., Diz, A., Schlickenrieder, J. and Martin-Carrasco, F., Environmental Science and Policy, 14 (2011) 744.

[3] Jaber, J.O. and Mohsen, M.S., Desalination, 136 (2001) 83.

[4] World Health Organization, HELI Technical Advisory Group in Jordan, Accessed in September 2013. http://www.who.int/heli/pilots/jordan/en/.

[5] Upson, S., Spectrum IEEE, 46 (2009) 13.

[6] Al-Amir, S.M., Al-Hamarneh, I.F., Al-Abed, T. and Awadallah, M., Applied Radiation and Isotopes, 70 (2012) 692.

[7] Bonotto, D.M., Applied Radiation and Isotopes, 69 (2011) 1572.

[8] Szabo, Z., dePaul, V.T., Fischer, J.M., Kraemer, T.F. and Jacobsen, E., Applied Geochemistry, 27 (2012) 729.

[9] Lloyd, J. and Pim, R., Journal of Hydrology, 121 (1990) 1.

[10] El-Naser, H. and Gedeon, R., *IAEA-TECDOC,* 890 (1996) 61.

[11] Compendium of Dose Coefficients based on ICRP Publication 60. ICRP Publication 119. Ann. ICRP 41 (Suppl.), The International Commission on Radiological Protection, (2012).

[12] Guidelines for Drinking-water Quality, Fourth Ed., World Health Organization, (2011).

[13] Chu, S., Ekstrom, L. and Firestone, R., WWW Table of Radioactive Isotopes, The Lund/LBNL Nuclear Data Search, Version 2.0, 1999, accessed in September 2013. http://nucleardata.nuclear.lu.se/toi/index.asp.

[14] Council Directive. Laying down requirements for the protection of the health of the general public with regard to radioactive substances in water intended for human consumption (2013). http://register.consilium.europa.eu/pdf/en/13/st07/st07445-re03.en13.pdf.

[15] United States Environmental Protection Agency US-EPA. Drinking Water: Radionuclides Rule (2001). http://water.epa.gov/lawsregs/rulesregs/sdwa/radionuclides/compliancehelp.cfm.

[16] Australian Drinking Water Guidelines 6, Volume 1, Australian Natural Resource Management Ministerial Council, National Health and Medical Research Council: Canberra, Australia, (2011).

[17] Recommendations for limiting exposure to ionizing radiation, Radiation Health Series No. 39, Government Publishing Service, Canberra, NHMRC National Health and Medical Research Council: Canberra, Australia, (1995).

[18] Lokan, K., Radiation Protection in Australasia, 15 (1998) 11.

[19] Technical Regulation (Mandatory) 286/2008 on Water - Drnking Water (in Arabic), Jordan Standards and Metrology Organization: Amman, Jordan, (2008).

[20] Tubiana, M., Aurengo, A., Averbeck, D. and Masse, R., Radiat. Environ. Biophys., 44 (2006) 245.

[21] Brenner, D.J. and Sachs, R.K., Radiat. Environ. Biophys., 44 (2006) 253.

[22] Breckow, J., Radiat. Environ. Biophys., 44 (2006) 257.

[23] Annals of the ICRP, Publication 103, The 2007 Recommendations of the International Commission on Radiological Protection, The International Commission on Radiological Protection, (2007).

[24] Report of the Committee Examining Radiation Risks of Internal Emitters (CERRIE), London, 2004, accessed in September 2013. http://www.cerrie.org/.

[25] Bonotto, D., Caprioglio, L., Bueno, T. and Lazarindo, J., Radiation Measurements, 44 (2009) 311.

[26] Schubert, M., Schuth, C., Michelsen, N., Rausch, R. and Al-Saud, M., International Journal of Water Resources and Arid Environments, 1 (2011) 25.

[27] Walsh, M., Wallner, G. and Jennings, P., Journal of Environmental Radioactivity, 130 (2014) 56.

[28] Dababneh, S., Journal of Environmental Science and Technology, 48 (2014) 9943.

Volume 8, Number 1, 2015. pp. 29-37

Jordan Journal of Physics

ARTICLE

Comparative Study of Soil Radon Concentration Levels Using Active and Passive Detectors

N. M. Ershaidat, B. A. Al-Bataina and **W. S. Al-Rayashi**

Department of Physics, Yarmouk University, Irbid 21163, Jordan.

Received on: 16/7/2014; Accepted on: 30/10/2014

Abstract: Passive radon diffusion dosimeters containing CR-39 detectors, and an active electronic device, RAD7®, were used for measuring soil radon concentration levels, at different depths, in a phosphatic site in the city of Irbid, north of Jordan. Time-averaged values of the active detector readings based on the periodicity of soil radon concentration levels are compared with measurements of the passive detectors at different depths. An acceptable agreement is observed.

Highlights

- Soil radon measured using an active detector (RAD7®) and a passive one (CR-39).
- Diurnal periodicity of soil radon diffusion and time-averaged values of RAD7® readings.
- The "average" readings of the RAD7® are compared to the measurements of the CR-39.

Keywords: Soil; Radon; Active detector, RAD7®, CR-39 dosimeters; Phosphate.

Introduction

Radon (^{222}Rn) study and measurements is an important topic in the applied nuclear and environmental field. Health hazards due to the exposure of population to radon and its progeny for long periods are the motivation behind many studies in this field. The major source of radon is soil and rocks beneath it. At least 80% of the radon emitted into the atmosphere comes from the top layers of the ground (around 1.5 m) [1].

Radon emanation is associated with the presence of uranium and its daughter radium in soil. Different types of rocks have typically different concentrations of uranium, thus different concentrations of radon, in soil and in the air above it. In particular, phosphate deposits contain the naturally occurring radionuclides ^{238}U and ^{232}Th together with their decay progeny. The radon gas belongs to the ^{238}U chain [2]. In Jordan, phosphate is an important national economic source. Many regions in the country are of the type of phosphatic formation. Radon environmental studies in many locations in Jordan, where the soil is phosphatic, were initiated more than 20 years ago. A national effort for the assessment of radon in dwellings, soil, water sources, …etc. had been carried out since the early 1990s [3-6]. The present work is a continuation of this effort.

There are several detection techniques for measuring radon concentration levels, among which are solid-state nuclear track detectors (SSNTD), ion chambers and solid-state detectors. They are mainly grouped into two categories: 1) passive diffusion radon dosimeters using CR-39 detectors [7-8] and the LR115 detectors [9]. 2) active detectors based on continuous radon sampling requiring an electric power [10] such as the RAD7® [11] and AalphaGuard® [20].

In this work, both CR-39 and RAD7®, from Durridge Co., Bedford, MA 01730, USA, have been used. Time integrated average values for soil radon concentration levels are obtained using the CR-39 dosimeters. In contrast, the

Corresponding Author: Nidal M. Ershaidat **Email**: enidal@yu.edu.jo

active detector RAD7® gives multiple readings over a given period of time.

Criteria for comparing these two types are mainly related to measurement precision and time needed for performing measurements in different operational conditions: atmospheric, landscape, … etc. [12].

The present comparative study is based on measurements of soil radon concentration levels in a phosphatic formation, using an active detector; RAD7®, in NORMAL mode, and a passive one; the CR-39 dosimeter.

There are several similar studies in literature. It is worth mentioning that none of them was concerned with phosphatic formations.

S. Giammanco et al. [13] made a comparison between different detection systems for measuring soil radon concentration levels along an active fault: the case of the Pernicana fault system, Mt. Etna (Italy). Three techniques were used: SSNTDs (CR-39 type), active detector (RAD7®) and soil CO_2 efflux measurement devices. Their main conclusion was as follows: while spot measurements of soil radon using RAD7® are useful for the quick recognition of high emission sites to be later monitored for ^{222}Rn variations in time, SSNTD (CR-39 type) allow for the temporal monitoring of a relatively large number of sites, but cannot distinguish short-term changes due to their long integration times.

M. Abo-Elmagd et al. [14] measured radon and its related parameters inside seven ancient Egyptian tombs of the Valley of the Kings in Luxor, using passive (CR-39) and active (Alpha-Guard analyzer) techniques. The measurements were performed throughout winter and summer seasons. They concluded that active measurements are precise and provide fast results, but cannot be used for a long time. The CR-39 can be used over long exposure periods; i.e., this technique is useful in *low-radioactivity* measurements.

G. Jönsson et al. [15], in the framework of an EU-radon project, measured radon levels with passive, solid state nuclear track detectors of the types LR 115, CR-39 and Makrofol and with active electronic devices. They showed that active detectors are able to give time resolved data, while passive detectors give time integrated data.

Finally, in a recent work, Espinosa et al. [10] published the results of an intercomparison of indoor radon data using NTDs (nuclear track detectors) and four different dynamic recording systems, including RAD7®. Measurements were carried out in a controlled one-room cellar carved into volcanic rock presenting an almost constant radon emanation throughout the four seasons. Averages of the sum of short-term measurements over a long period were used in order to make a comparison with the passive detectors' response. Their main conclusion was that the active electronic devices can give good account of short-term indoor fluctuations even if the average radon concentrations of different monitors differ by 35%. They attribute these fluctuations to sudden changes in temperature and humidity of the air in the cellar.

The previous results [10] were based on averaging over a long period of time (three months). In this study, the idea is to use the periodicity of diurnal soil radon concentration levels in order to find an average over a relatively short period of time (7 hours).

Methodology and Experimental Procedure

Active detectors are designed to be used in measurements of indoor radon, especially in dwellings for safety purposes. For measurements of radon in water samples or in soil, simple extra accessories are needed.

RAD7®, recently acquired, was used for the first time in this work. It is calibrated by the manufacturer against a master instrument, which, in turn, is calibrated against a standard maintained by the British National Radiological Protection Board (NRPB), known as HPA (Health Protection Agency) since 2004. The overall calibration accuracy is estimated to be about ±5%.

RAD7® is a versatile radon detector. It is a measuring instrument used in laboratories and research work by radon testers, mitigators and home inspectors, in various sites with different climatic conditions. RAD7® is a computer-driven electronic detector and easy to use, with pre-programmed set-ups for common tasks.

The RAD7®'s internal sample cell is a 0.7 liter hemisphere, coated on the inside with an electrical conductor. A solid-state, ion-implanted, planar, silicon alpha detector is at the center of the hemisphere. The high voltage power circuit charges the inside conductor to a potential of 2000 to 2500V, relative to the detector, creating an electric field throughout the volume of the cell.

RAD7® is a sniffer that uses the 3-minute alpha decay of a radon daughter, without interference from other radiations, and the instantaneous alpha decay of a thoron daughter. It sniffs out entry points and radon gushers and recovers in minutes from high radon exposures.

The site chosen (latitude 32° 32’, longitude 35° 51’) is in the city of Irbid, Jordan, near the campus of Yarmouk University. The bedrock is a mixture of Al-Hisa Phosphatic (AHP) Limestone and Amman Silicified Limestone (ASL) formations [16].

A hole was dug and, for averaging purposes, two previously calibrated CR-39 dosimeters of closed can technique [6] were placed at 100, 80, 60, 40, 20 and 0 cm depths. Thus, a total of twelve dosimeters were used. Each time a dosimeter was planted, the depth was refilled with the soil extracted while digging. No external source of soil was used.

All dosimeters were left *in situ* for 22 days before being collected, so that radon gas can reach secular equilibrium with its parent (^{226}Ra). In order to extract the soil radon concentration levels, a standard procedure for the treatment of the dosimeters is followed in a similar manner as in [6]. A 15% error estimation is also made as in the previous reference.

When using the active detector, it is essential to collect radon samples without exposing them to outside air. For this purpose, a special probe was devised for this study. A flexible transparent tube, 0.45 inch in diameter and 10 m in length, is inserted into metallic pipes of half an inch diameter. The metallic pipes’ lengths were (10, 30, 50, 70, 90 and 110 cm) used for the depths: 0, 20, 40, 60, 80 and 100 cm, respectively. Thus, each of the latter pipes appears 10 cm above the soil. The probes were inserted at the same time as the dosimeters were planted. To avoid leakages of all kinds, the metallic pipes were tightly closed. Fig. 1 shows a schematic representation of the setup. Measurements were carried out on a daily basis for each depth for eight hours from 09:00 am to 5:00 pm. Readings after every half-hour cycle ware registered. Thus, the total number of readings taken is sixteen (16). To avoid the effect of deposition of solid particles (decay products of radon) on the active detector, RAD7® was put off for the rest of the day between two consecutive sets of measurement in order to get rid of these solid daughters.

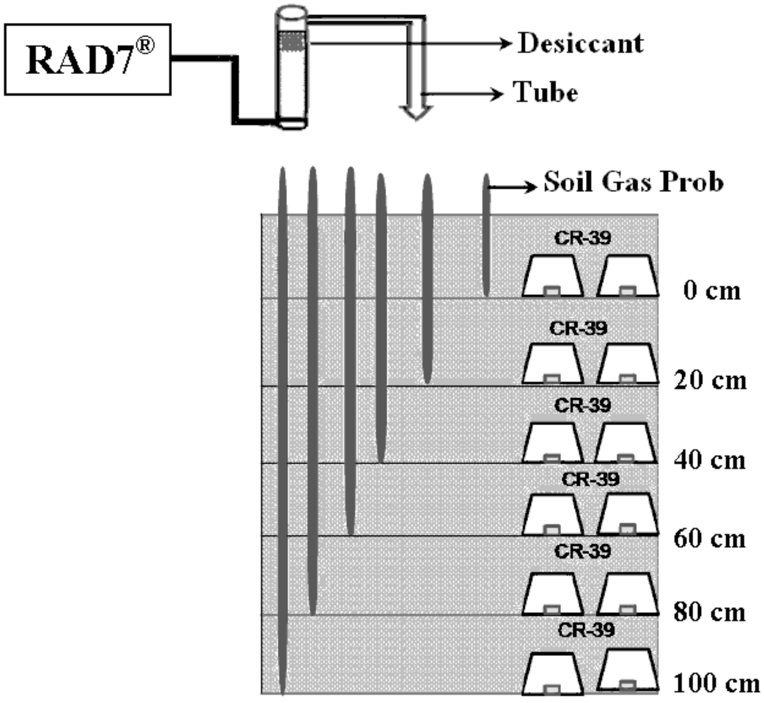

FIG. 1. Experimental setup - schematic.

Data were taken from Feb. 26 to March 3, 2011, during the rainfall season in the region. There was no rainfall during this period and temperatures of the air registered by RAD7® ranged between 15.5 °C and 19.4 °C. In addition, the studied soil represents an acceptable homogeneity and thus variations of moisture and water saturation will be neglected in this study [16].

The first two readings will be low, because the ^{218}Po decay rate in the detector takes more than 10 minutes to reach equilibrium with the radon concentration in the measurement chamber. Readings are stored in the RAD7® memory for later use. Thus, 14 of the 16 recorded readings, for each depth, will be used in this work.

Because of the high quality alpha semiconductor detector, and unique real-time spectral analysis, the RAD7® background is vanishingly small and is immune to the buildup of lead-210, which plagues other instruments. Intrinsic background may add less than 1 Bq/m^3 to a typical measurement, far below the radon concentration of outdoor air (usually several Bq/m^3 to few tens of Bq/m^3). All the previous details as well as the technique of calculating the radon concentration levels separately from those of thoron and corrections due to absolute humidity and more technical specifications can be found in the RAD7® user's manual [11]. The practical timetable followed is shown in Table 1.

TABLE 1. Practical timetable for measuring soil radon concentration levels.

Depth (cm)	0	20	40	60	80	100
RAD7® (8 hours daily)	Day 1	Day 2	Day 3	Day 4	Day 5	Day 6
CR-39	22 days					

Results and Data Analysis

The RAD7® Readings

Figures 2-6 show radon concentration levels using RAD7® (C_{RAD7}) for the depths 20, 40, 60, 80 and 100 cm. In most circumstances, the precision of individual RAD7® measurements of radon concentration is limited by counting statistics. In Figs. 2-6, an overall error of ±5% is considered for each individual measurement instead of using the error given by the device itself. For the depth z = 0 cm, the maximum measured value is adopted; namely 1170 Bq/m^3. As explained earlier, the first two readings, for each depth, are dropped.

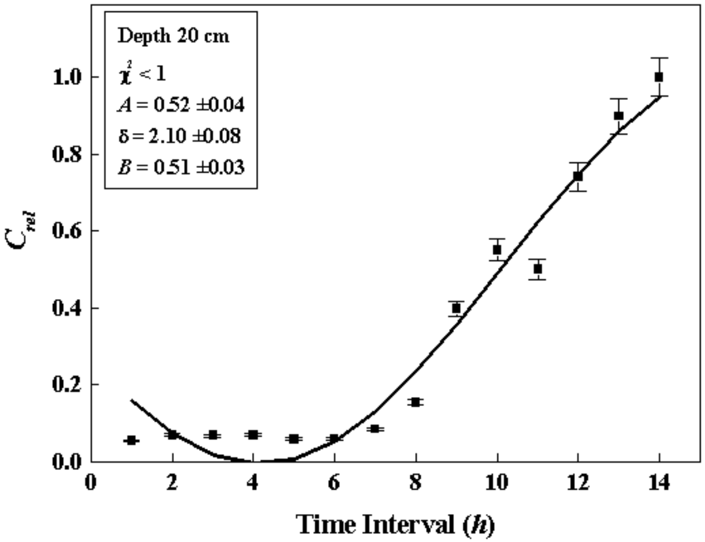

FIG. 2. RAD7® readings at a depth of 20 cm. See text for the fit details.

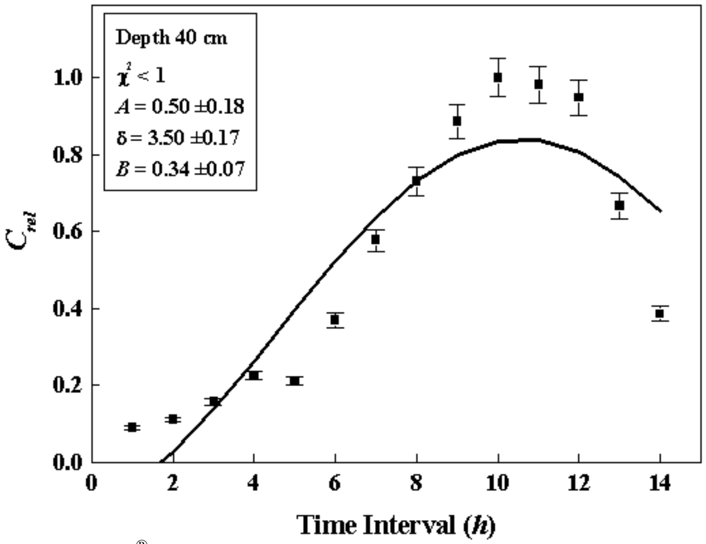

FIG. 3. RAD7® readings at a depth of 40 cm. See text for the fit details.

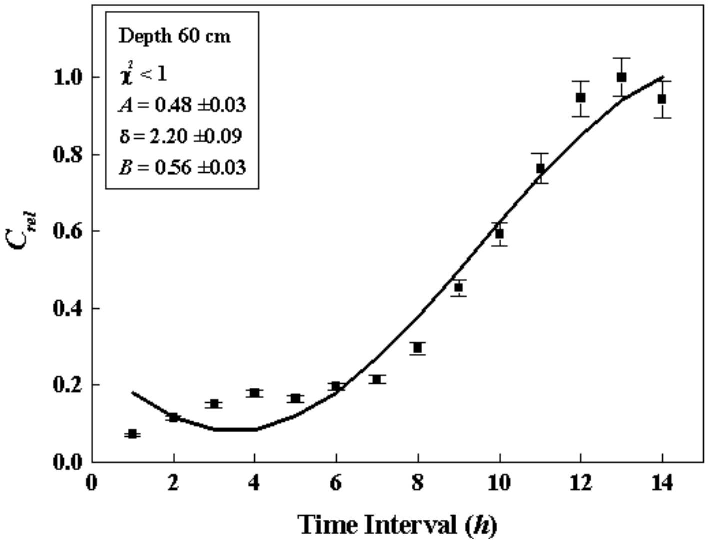

FIG. 4. RAD7® readings at a depth of 60 cm. See text for the fit details.

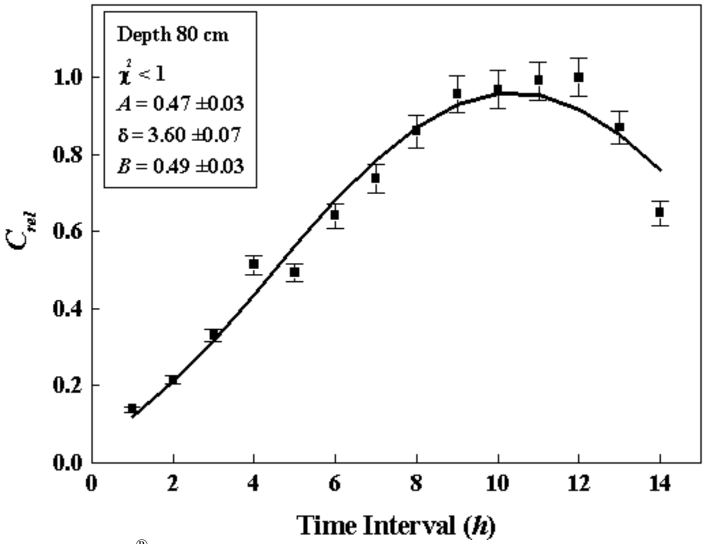

FIG. 5. RAD7® readings at a depth of 80 cm. See text for the fit details.

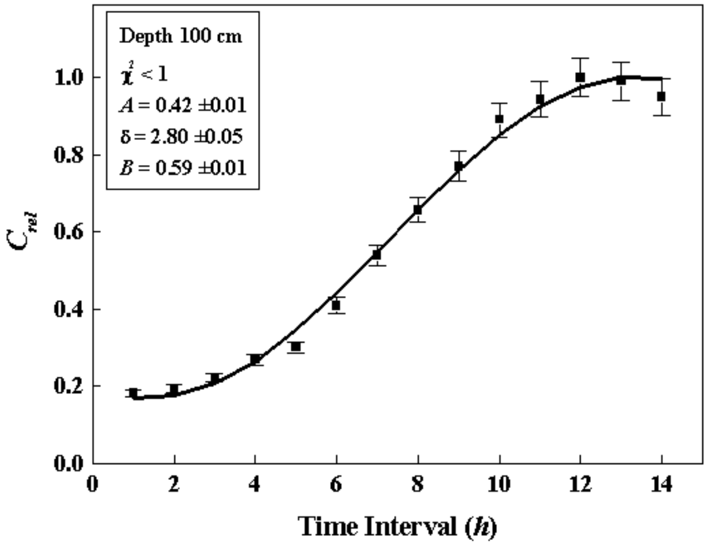

FIG. 6. RAD7® readings at a depth of 100 cm. See text for the fit details.

The CR-39 Readings

Table 2 shows the soil radon concentration levels measured using the CR-39 dosimeters (C_{CR39} in Bq/m^3) for the depths 0, 20, 40, 60, 80 and 100 cm. Each of these measurements is the average reading of two dosimeters positioned at a given depth.

Fig. 7 shows a comparison between the two types of detectors, for the same depths mentioned above, where the averages of the RAD7® readings for each depth were considered.

Another possible comparison can be achieved where the RAD7® data is fitted to a cosine function. This choice is based on the well established periodicity of soil radon diffusion [17-18]. The basic idea is that, for a given depth *z*, variation of soil radon concentration with time follows a similar pattern as the soil's temperature. In the appendix below, the major ideas are discussed.

We actually use the relative quantity, for a given depth,

$$C_{rel} = \frac{C_{RAD7}}{C_{max}} \qquad (1)$$

where C_{RAD7} and C_{max} are respectively the reading of RAD7® and the maximum value of the set of 14 readings of the active detector.

TABLE 2. C_{CR39}, C_{max}, $\overline{C}$ and $\overline{C}_{Fit}$ for all depths. See text for the definitions.

Depth z (cm)	0	20	40	60	80	100
C_{CR39} (Bq/m^3)	1390	9682	16778	19817	21720	24206
C_{max} (Bq/m^3)	1170	7904	25168	28359	23041	17328
$\overline{C}$ (Bq/m^3)	1170	2655	13197	12303	15412	10299
$\overline{C}_{Fit}$ (Bq/m^3)	-	2907	15714	13782	17852	11588
$diff_1 = \frac{\lvert C_{max} - C_{CR39} \rvert}{C_{CR39}} \times 100\%$	16	18	50	43	6	28
$diff_2 = \frac{\lvert \overline{C} - C_{CR39} \rvert}{C_{CR39}} \times 100\%$	16	73	21	38	29	57
$diff_3 = \frac{\lvert \overline{C}_{Fit} - C_{CR39} \rvert}{C_{CR39}} \times 100\%$		74	18	39	27	57

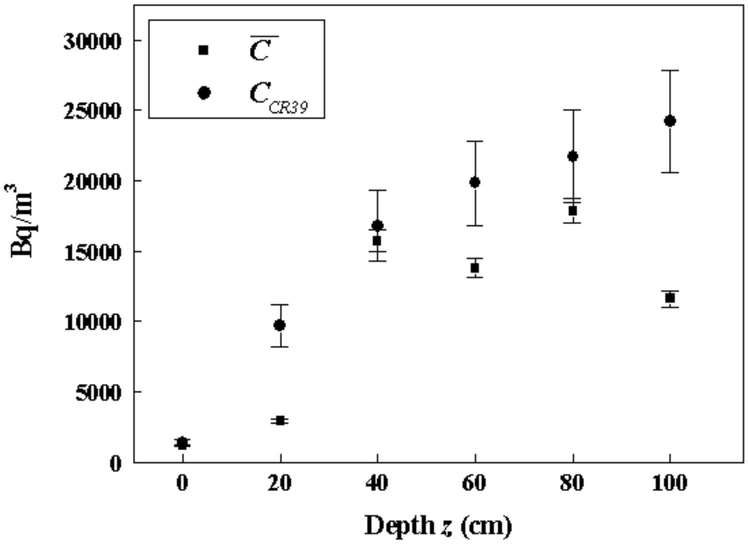

FIG. 7. $\overline{C}$ (RAD7®) vs. C_{CR39} for all depths.

Eq. A7; namely $C_{fit} = A\cos(\omega t+\delta)+B$ with ω = 0.262 rad/hour, is used to fit the data (C_{rel}). The fit parameters are: the dimensionless offset constants *A* and *B* and the phase constant δ. The pre-imposed confidence level is 90%.

Figures 2-6 also show the fitting curves, as well as the resulting parameters of the fit: *A*, B and δ.

Although the periodicity of soil radon diffusion is admitted to be valid for small depths (typically 50 cm), the fit here was done for all depths from 20 to 100 cm. It is being used as a mathematical tool in order to find a time-averaged value for the set of readings of RAD7® for each depth.

This average is defined as:

$$\overline{C}_{Fit} = C_{RAD7} \times \frac{1}{13}\int_{1}^{14} \left(A\cos(\omega t+\delta)+B\right)\, dt \tag{2}$$

The obtained values, called ($\overline{C}_{Fit}$), are shown in Table 2. The simple average ($\overline{C}$) as well as (C_{max}) for each set of the RAD7® measured values are also shown for comparison purposes. The last rightmost columns in the table give the following differences:

$$\left.\begin{aligned} diff_1 &= \frac{|C_{max} - C_{CR39}|}{C_{CR39}} \times 100\%\ , \\ diff_2 &= \frac{|\overline{C} - C_{CR39}|}{C_{CR39}} \times 100\%\ , \\ diff_3 &= \frac{|\overline{C} - C_{CR39}|}{C_{CR39}} \times 100\%\ . \end{aligned}\right\} \tag{3}$$

Finally, Fig. 8 shows $\overline{C}_{Fit}$ compared to the readings of the CR-39 passive detectors.

Discussion

The following remarks can be drawn from the previous results:

1- Both types of measurements, using the RAD7® active detector and the CR-39 passive dosimeters, show that soil radon concentration levels increase exponentially with depth as expected and confirmed by many previous studies [19].

2- Data fitting to a time-dependent cosine function, inspired by the variation of the soil's temperature, is valid for small depths $z \leq 60$ cm. Extrapolating to larger depths give acceptable results.

3- Averages, over a short period of time, obtained using this fit, give values of soil radon concentration levels which are comparable, and in the right range, to measurements obtained using the passive detectors.

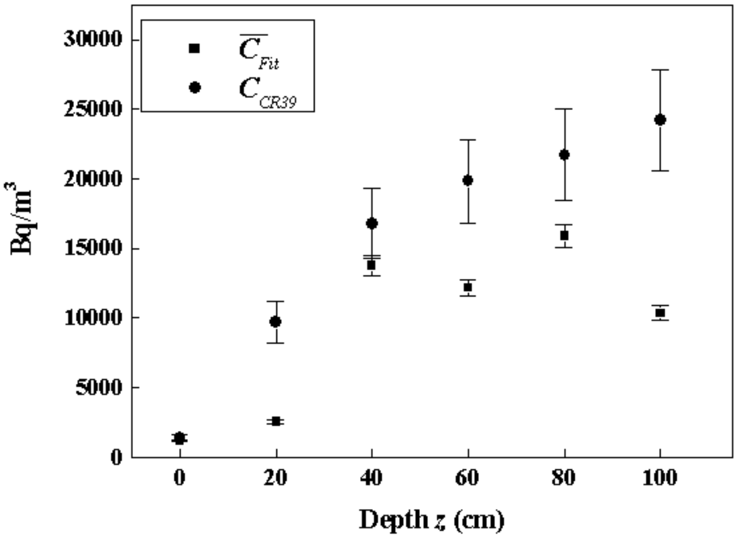

FIG. 8. $\overline{C}_{Fit}$ (RAD7®) vs. C_{CR39} for all depths.

The percent differences, for each depth, between C_{max}, $\overline{C}$ and $\overline{C}_{Fit}$, shown in Table 2, indicate that the average-time values can represent well the set of readings of RAD7® over the time period of measurement (7 hours).

Conclusion

Measurements using the RAD7® active detector and the CR-39 passive radon diffusion dosimeters show that soil radon concentration levels increase with depth as expected and confirmed by many previous studies [19]. The differences between the two types of detectors are mainly due to their function modes.

Taking the simple average of a set of readings of RAD7® over a short period of time gives the differences $(diff_2)$16%, 73%, 21%, 38%, 29% and 57% for the depths 0, 20, 40, 60, 80 and 100 cm, respectively.

A standard non-linear least squares fit using a cosine function ($A\cos(\omega t + \delta) + B$), where ω is the angular frequency of the rotation of the earth around the sun, was used in order to smooth the RAD7® data using the expected periodic behavior of soil radon concentration with time. The time-average of this function is taken as being the "reading" of RAD7® for a given depth. Comparing this time-average to its corresponding measurement by the passive CR-39 dosimeters gives acceptable results.

The differences in this case $(diff_3)$ are 16%, 74%, 18%, 39%, 27% and 57% for the depths 0, 20, 40, 60, 80 and 100 cm, respectively.

Comparing these differences with those in the previous paragraph indicates that the time-averaged values of the RAD7® readings "inspired" by the cosine behavior can be well considered instead of the simple averages over a short period of time.

Appendix

The temperature of the soil can be obtained from the solution of the heat equation:

$$\frac{\delta T}{\delta t} = a\nabla^2 T \tag{A1}$$

with a heat wave, originating from the sun and hitting the soil, given by:

$$T(t) = T_0\cos(\omega t + \delta) \text{ at } z = 0. \tag{A2}$$

a is the Fourier coefficient, which is related to the physical properties of the diffusing medium as follows. For a medium of density ρ (g cm^{-3}) and specific heat capacity at constant pressure c_P (J g^{-1} K^{-1}) and thermal conductivity (k (usual units: W m^{-1} K^{-1}), we have:

$$a = \frac{k}{(\rho c_P)} \quad . \tag{A3}$$

T_0 is the maximum amplitude of the heat source (the sun) generally taken to be 15 °C; i.e., the average temperature of the earth, ω is the angular frequency of the earth ($\omega = 7.27\times10^{-5}$ rad/s = 0.262 rad/hour) and δ is a phase constant.

The temperature field, $T(z,t)$, at depth z below the soil/air interface is the solution of the heat equation with the boundary conditions:

$$T(0,t) = T_{av} + T_0 \cos(\omega t) \tag{A4}$$

$$T(\infty,t) = T_{av} \ , \tag{A5}$$

where T_{av} is the average temperature of the soil-air interface (around 18 °C in this study). This solution has the form - see details in [18]:

$$T(z,t) = T_{av} + T_0 e^{-Fz} \cos\left(\omega\left(t - \frac{z}{v}\right)\right), \tag{A6}$$

where F is the inverse of the damping width which is the width at which the amplitude of the wave is reduced by a factor $1/e$ and v is the diffusion velocity.

Taking a, the Fourier coefficient for soil (0.018 cm^2 s^{-1}), $F = \sqrt{\omega/(2a)} = 0.0449\,\mathrm{cm}^{-1}$, $v = \sqrt{2a\omega} = 0.0016\,\mathrm{cm\,s^{-1}} = 5.827\,\mathrm{cm\,h^{-1}}$.

The periodic function used for the fit of the RAD7® data is:

$$C_{fit} = A\cos(\omega t + \delta) + B. \tag{A7}$$

See text for more details on the fit parameters.

References

[1] NCRP, 1984. Report No. 78. Evaluation of occupational and environmental exposures to radon and radon daughters in the United States.

[2] IAEA (International Atomic Energy Agency) (2013). Safety Reports, series No. 78, Radiation Protection and Management of NORM Residues in the Phosphate Industry.

[3] Al-Kofahi, M.M., Khader, B.R., Lehlooh, A.D., Kullab, M.K., Abumurad, K.M. and Al-Bataina, B.A., Nucl. Tracks Radiat. Meas., 20 (1992) 377.

[4] Abumurad, K., Al-Bataina, B., Ismail, A., Kullab, M. and Al-Eloosy, A., Radiat. Prot. Dosimetry, 69 (1997) 221.

[5] Al-Bataina, B.A., Ismail, A.M., Kullab, M.K., Abumurad, M.K. and Mustafa, H., Radiat. Meas., 28 (1997) 591.

[6] Al-Shereideh, S.A., Al-Bataina, B.A. and Ershaidat, N.M., Radiat. Meas., 41 (2006) 703.

[7] Jönsson, G. and Hellborg, R., Nucl. Tracks Radiat. Meas. 19 (1991) 333.

[8] Durrani, S.A and Ilic, R., "Radon Measurement by Etched Track Detector Application in Radiation Protection, Earth Science and Environment". (World Scientific Singapore, 1997).

[9] Nikezić, D. and Yu, K.N., NIM in Phys. Res. B, 196 (2002) 105.

[10] Espinosa, G., Golzarri, J.J., Gaso, M.I., Mena, M. and Segovia, N., Radiat. Meas., 50 (2013) 112.

[11] Durridge Company, Inc. (2000), Reference Manual, version 6.0.1, RAD7 Electronic Radon Detector.
(http://www.durridge.com/products_rad7.shtml)

[12] Ruckerbauer, F. and Winkler, R., Appl. Radiat. Isot., 55 (2001) 273.

[13] Giammanco, S., Imme, G., Mangano, G., Morelli, D. and Neri, M., Appl. Radiat. Isot., 67 (2009) 185.

[14] Abo-Elmagd, M., Metwally, S.M., El-Fiki, S.A., Eissa, H.M. and Salama, E., Radiat. Meas., 42 (2007) 116.

[15] Jönsson, G., Albarracin, D., Bacmeister, G.U., Baixeras, C., Climent, H., Cotellessa, G., Devantier, R., Enge, W., Freyer, K., Font, L.L., Ghose, R., Monnin, M.M., Sciocchetti, G., Seidel, J.L. and Treutler, H.C., Radiat. Meas., 28 (1997) 651.

[16] Shweikani, R., Giaddui, T.G. and Durrani, S.A., Radiat. Meas., 25 (1995) 581.

[17] Schubert, M. and Schulz, H., Health Phys., 83 (2002) 91.

[18] Ershaidat, N.M., Almomani, R.R., Al-Bataina, B.A. and Al-Rayashi, W.S., Jordan J. Phys., 6 (2013) 47.

[19] Ershaidat, N.M., Al-Bataina, B.A. and Al-Shereideh, S.A., Environ. Geol., 55 (2008) 29.

[20] Saphymo, GmbH, Heerstraße 149, D-60488 Frankfurt am Main – Germany. Saphymo.de

Volume 8, Number 1, 2015. pp. 39-47

Jordan Journal of Physics

ARTICLE

Reflection of Polarized Light at Quasi-Index-Matched Dielectric-Conductor Interfaces

R. M. A. Azzam

Department of Electrical Engineering, University of New Orleans, New Orleans, Louisiana 70148, USA.

Received on: 20/1/2015; Accepted on: 7/7/2015

Abstract: Quasi-index-matched (QIM) dielectric-conductor interfaces are characterized by a unit-magnitude complex relative dielectric function, $\varepsilon = \exp(-j\theta), 0 \leq \theta \leq \pi,$ and exhibit minimum reflectance at normal incidence. Their reflection properties are analyzed in detail as functions of the incident linear polarization (*p* or *s*), angle of incidence ϕ and θ. Complex-plane trajectories of the Fresnel reflection coefficients $r_p(\phi)$, $r_s(\phi)$ and their ratio $\rho(\phi) = r_p / r_s = \tan\psi \exp(j\Delta)$ as ϕ increases from 0 to 90° are presented at discrete values of θ. Absolute values and phase angles of r_p, r_s and ρ are also plotted as functions of ϕ. Finally, the pseudo-Brewster angle of minimum $|r_p|$, the second-Brewster angle of minimum $|\rho|$, the principal angle at which $\Delta = \pi/2$ and the special angle $(\phi = \sin^{-1}\sqrt{0.5\sec\theta})$ at which $\delta_p = \arg(r_p) = \pm\pi$ of QIM interfaces are determined as functions of θ.

Keywords: Physical optics; Reflection; Interfaces; Polarization; Dielectric function; Ellipsometry.
PACS: 42. Optics.

1. Introduction

The reflectance of monochromatic light at normal incidence by the plane boundary between a transparent medium of incidence with real dielectric function ε_0 and an absorbing medium of refraction with complex dielectric function ε_1 is minimized when $\varepsilon_0 = |\varepsilon_1|$. The complex relative dielectric function $\varepsilon = \varepsilon_1 / \varepsilon_0$ of such quasi-index-matched (QIM) interfaces [1] has unit magnitude and is expressed in polar form as:

$$\varepsilon = \exp(-j\theta), 0 \leq \theta \leq \pi. \tag{1}$$

The range of θ in Eq. (1) is consistent with the $\exp(-j\omega t)$ time dependence (*j* is the pure imaginary number and ω is the angular frequency) and the Nebraska-Muller conventions [2]. Specific examples of interfaces that satisfy the QIM condition in different spectral regions are given in Appendix A.

For a given ε, the complex-amplitude Fresnel reflection coefficients of *p*- and *s*-polarized light at an oblique angle of incidence ϕ are given by [3, 4]:

Corresponding Author: R. M. A. Azzam **Email**: razzam@uno.edu

$$r_p = \frac{\varepsilon \cos\phi - (\varepsilon - \sin^2\phi)^{1/2}}{\varepsilon \cos\phi + (\varepsilon - \sin^2\phi)^{1/2}}, \qquad (2)$$

$$r_s = \frac{\cos\phi - (\varepsilon - \sin^2\phi)^{1/2}}{\cos\phi + (\varepsilon - \sin^2\phi)^{1/2}}. \qquad (3)$$

At normal incidence $(\phi = 0)$, the reflection coefficients r_p, r_s of QIM interfaces with unit-magnitude relative dielectric function [Eq. (1)] reduce to:

$$r_p = -j\tan(\theta/4), r_s = +j\tan(\theta/4). \qquad (4)$$

From Eqs. (4), it is apparent that the reflection *p*- and *s*-polarized light at normal incidence by QIM interfaces is accompanied by quarter-wave $(\mp\pi/2)$ phase shifts and that the associated amplitude reflectances are equal to the tangent of one-fourth the angle θ of complex ε.

In this study, the complex reflection coefficients r_p, r_s, and ellipsometric function [3, 5],

$$\left.\begin{aligned} \rho &= r_p / r_s = \tan\psi \exp(j\Delta) \\ &= \frac{\sin\phi\tan\phi - (\varepsilon - \sin^2\phi)^{1/2}}{\sin\phi\tan\phi + (\varepsilon - \sin^2\phi)^{1/2}}, \end{aligned}\right\} \qquad (5)$$

of QIM dielectric-conductor interfaces are considered in detail as functions of both ϕ and θ.

In Section 2, complex-plane trajectories of r_p and r_s as the angle of incidence ϕ increases from $\phi = 0$ [initial values given by Eqs. (4)] to $\phi = 90^\circ$ [$r_p = r_s = -1$] are presented at discrete values of θ in the range $0 \le \theta \le 180^\circ$. Amplitude reflectances $|r_p|$, $|r_s|$ and phase shifts $\delta_p = \arg(r_p)$, $\delta_s = \arg(r_s)$ are also plotted as functions of ϕ at the same discrete values of θ.

In Section 3, trajectories of $\rho(\phi)$, $0 \le \phi \le 90^\circ$, in the complex plane and graphs of the ellipsometric parameters $\tan\psi$ and Δ *versus* ϕ at constant values of θ are presented.

In Section 4, the pseudo-Brewster angle of minimum reflectance for incident *p*-polarized light [6 - 9], the principal angle at which the differential reflection phase shift $\Delta = \pi/2$ [7, 10], the second-Brewster angle of minimum reflectance ratio $|\rho|$ [11] and the special angle at which the reflection phase shift of *p*-polarized light $\delta_p = \pm\pi$ [12] are all determined as functions of θ for all QIM dielectric-conductor interfaces.

Section 5 gives a brief summary of this work.

2. Reflection Coefficients of *p*- and *s*-Polarized Light at QIM Dielectric-Conductor Interfaces

Fig. 1 shows the complex-plane trajectories of $r_p(\phi)$ as ϕ increases from 0 [initial values $r_p(0)$ along the negative imaginary axis *ON* given by Eqs. (4)] to 90° ($r_p = -1$ at point *G*) for QIM dielectric-conductor interfaces with $\theta = 0.1^\circ$ and $\theta = 10^\circ$ to 180° in equal steps of 10°.

Note that $\theta = 0$ represents a vanishing optical interface with $\varepsilon = 1$, so that $r_p = r_s = 0$ at all angles of incidence and the corresponding trajectory collapses to a single point at the origin *O*. For $\theta = 180^\circ$ and $\varepsilon = -1$ (an ideal dielectric-plasma interface), total reflection takes place $|r_p| = |r_s| = 1$ at all incidence angles, and the corresponding locus of $r_p(\phi)$ becomes the arc *NG* of the unit circle in the third quadrant of the complex plane. The ϕ- dependent phase shift along this unit-circle arc is derived from Eq. (2) as:

$$\delta_p(\phi) = -2\tan^{-1}[(1 + \sin^2\phi)^{1/2} / \cos\phi]. \qquad (6)$$

The top and bottom parts of Fig. 2 show the amplitude and phase plots $|r_p|(\phi)$ and $\delta_p(\phi)$, respectively, for $\theta = 0.1^\circ$ and $\theta = 10^\circ$ to 180° in equal steps of 10°. The pseudo-Brewster angle ϕ_{pB} of minimum $|r_p|$ is $< 45^\circ$ for all values of θ, as is discussed further in Section 4. The angles of incidence at which $\delta_p = \pm 180^\circ$ (located at the vertical transitions in the $\delta_p - vs - \phi$ curves) are also determined in Section 4.

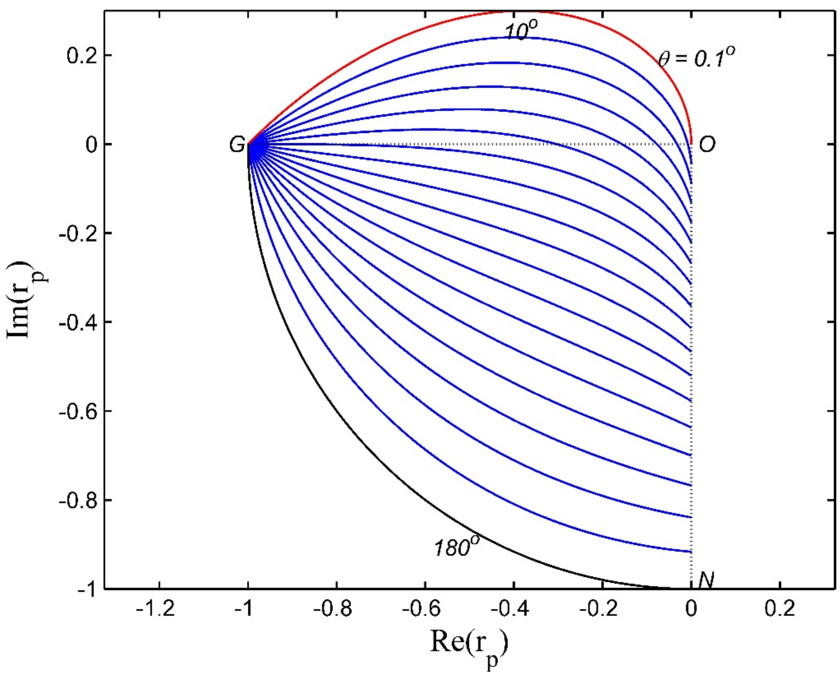

FIG. 1. Complex-plane trajectories of $r_p(\phi)$ as ϕ increases from 0 [initial values $r_p(0)$ along the negative imaginary axis *ON* are given by Eqs. (4)] to 90° ($r_p = -1$ at point *G*) of QIM dielectric-conductor interfaces with $\theta = 0.1^{\circ}$ and $\theta = 10^{\circ}$ to 180° in equal steps of 10°.

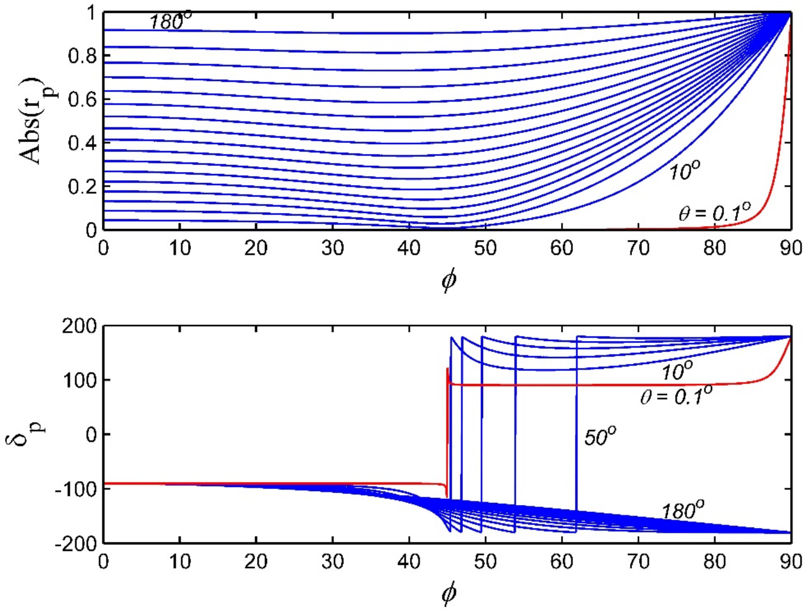

FIG. 2. Amplitude reflectance $|r_p|(\phi)$, top, and phase shift $\delta_p(\phi)$, bottom, as functions of incidence angle ϕ for QIM interfaces with $\theta = 0.1^{\circ}$ and $\theta = 10^{\circ}$ to 180° in equal steps of 10°.

Fig. 3 shows the complex-plane trajectories of $r_s(\phi)$ as ϕ increases from 0 to 90°, with initial values $r_s(0)$ located on the positive imaginary axis *ON* [given by Eqs. (4)] and the same θ values used in Fig. 1. In the limiting case of $\theta = 180^{\circ}$, the locus of $r_s(\phi)$ is the arc *NG* of the unit circle in the second quadrant of the complex plane. The associated ϕ- dependent phase shift $\delta_s(\phi)$ equals the negative of $\delta_p(\phi)$ given by Eq. (6).

The amplitude reflectance of s-polarized light $|r_s|(\phi)$ and associated reflection phase shift $\delta_s(\phi)$ are plotted in the top and bottom parts of Fig. 4, respectively. Both $|r_s|$ and δ_s increase monotonically with ϕ from normal to grazing incidence.

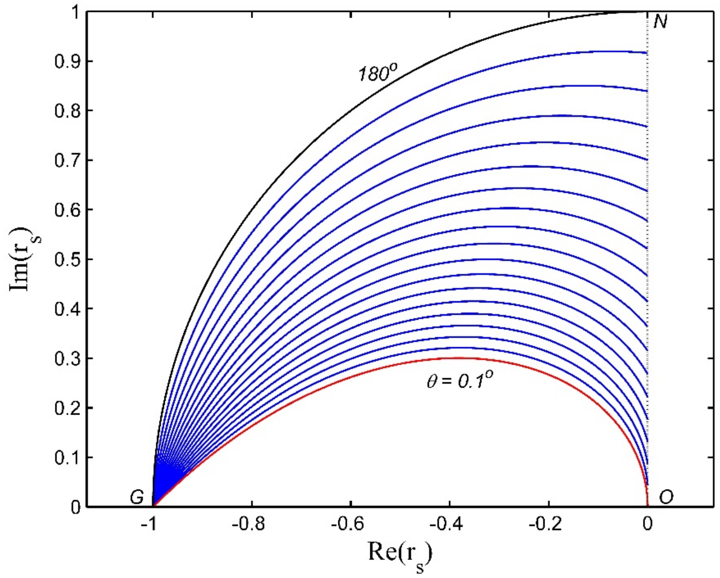

FIG. 3. Complex-plane trajectories of $r_s(\phi)$ as ϕ increases from 0 [initial values $r_s(0)$ along the positive imaginary axis *ON* are given by Eqs. (4)] to 90° ($r_s = -1$ at point *G*) of QIM dielectric-conductor interfaces with $\theta = 0.1^\circ$ and $\theta = 10^\circ$ to 180° in equal steps of 10°.

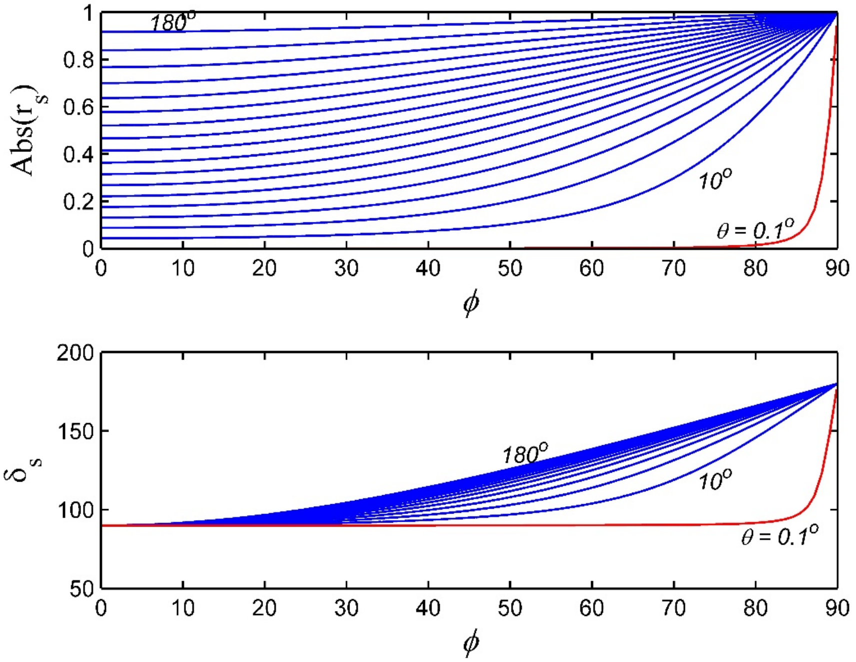

FIG. 4. Amplitude reflectance $|r_s|(\phi)$, top, and phase shift $\delta_s(\phi)$, bottom, as functions of incidence angle ϕ for QIM interfaces with $\theta = 0.1^\circ$ and $\theta = 10^\circ$ to 180° in equal steps of 10°.

3. Ellipsometric Function of QIM Dielectric-Conductor Interfaces

Fig. 5 shows trajectories of the ratio of complex reflection coefficients $\rho = r_p / r_s = \tan\psi \exp(j\Delta)$ as ϕ increases from normal to grazing incidence for QIM dielectric-conductor interfaces at the same θ values used in Figs. 1 and 3. All curves start at $\rho = -1$ when $\phi = 0$ (point *N*) and end at $\rho = +1$ when $\phi = 90^\circ$ (point *G*). The point of intersection of each curve with the imaginary axis (represented by the vertical dashed line in Fig. 5) defines a unique principal angle ϕ_{PA} at which $\Delta = 90^\circ$. Dependence of ϕ_{PA} on θ is presented in Section 4.

The top and bottom parts of Fig. 6 show $\tan\psi$ and Δ, respectively, as functions of ϕ along each one of the contours in Fig. 5. The $\Delta - vs - \phi$ curve at $\theta = 0.1^\circ$ is nearly a step function with vertical transition of Δ from 180° to 0° located at $\phi = 45^\circ$, which is the second Brewster angle at which $\tan\psi \approx 0$.

In Fig. 6, the $\Delta - vs - \phi$ curve at $\theta = 180^\circ$ is described by:

$$\left.\begin{array}{l}\Delta(\phi) = \\ 360^\circ - 4\tan^{-1}[(1+\sin^2\phi)^{1/2}/\cos\phi].\end{array}\right\} \qquad (7)$$

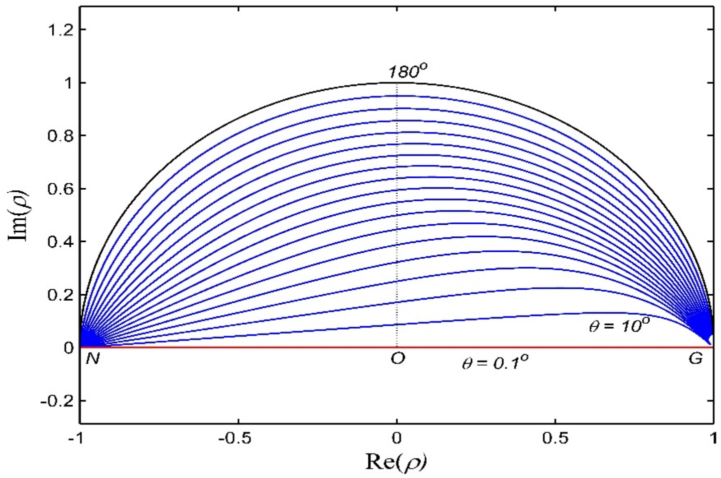

FIG. 5. Trajectories of the ellipsometric function $\rho(\phi) = r_p / r_s = \tan\psi \exp(j\Delta)$ as ϕ increases from 0 to 90° for QIM dielectric-conductor interfaces with $\theta = 0.1^\circ$ and $\theta = 10^\circ$ to 180° in equal steps of 10°.

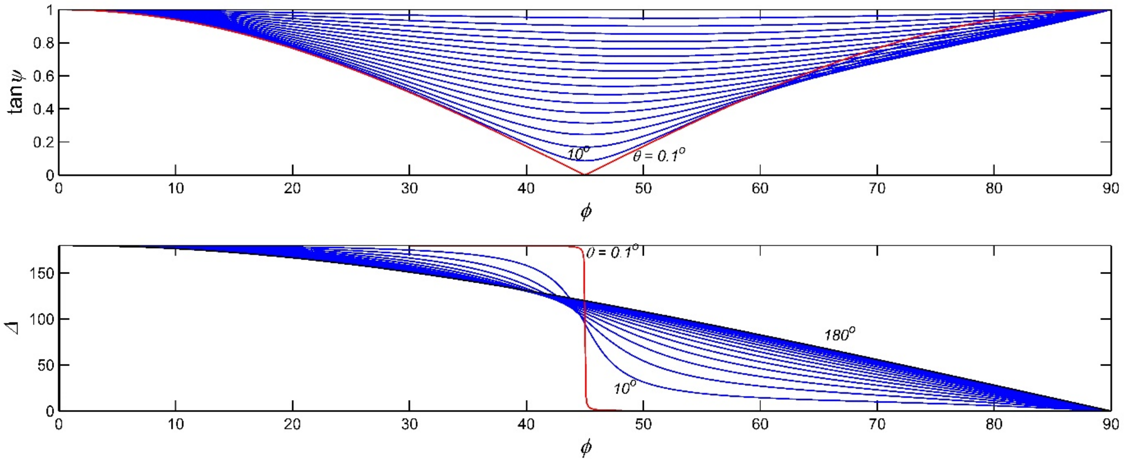

FIG. 6. Ellipsometric parameters $\tan\psi$ and Δ as functions of ϕ along each one of the contours shown in Fig. 5.

4. Special Angles of Incidence Associated with Light Reflection at QIM Dielectric-Conductor Interfaces

The pseudo-Brewster angle ϕ_{pB} of minimum $|r_p|$ of a QIM dielectric-conductor interface is determined by solving the following cubic equation [9]:

$$a_3u^3 + a_2u^2 + a_1u + a_0 = 0, \tag{8}$$

in which $u = \sin^2\phi_{pB}$ and

$$\left.\begin{aligned} a_3 &= 2\cos\theta + 2, \\ a_2 &= a_1 = -2, \\ a_0 &= 1. \end{aligned}\right\} \tag{9}$$

Likewise, the principal angle ϕ_{PA} at which $\Delta = 90^\circ$ [10] is obtained by solving another cubic equation [Eq. (8)] with $u = \sin^2\phi_{PA}$ and coefficients given by:

$$\left.\begin{aligned} a_3 &= a_1 = 2\cos\theta + 2, \\ a_2 &= 2 - 2a_1, \\ a_0 &= -1. \end{aligned}\right\} \tag{10}$$

The second-Brewster angle ϕ_{2B} of minimum $|\rho|$ of a QIM interface is determined by solving a quartic equation [11],

$$a_4u^4 + a_3u^3 + a_2u^2 + a_1u + a_0 = 0, \tag{11}$$

with $u = \sin^2\phi_{2B}$ and

$$\left.\begin{aligned} a_4 &= \tan(\theta/2) - \sin\theta, \\ a_3 &= 2\sin\theta - 0.5\tan(\theta/2), \\ a_2 &= 0.5\tan(\theta/2)[\sec^2(\theta/2) - 2\cos\theta - 8], \\ a_1 &= 0.5\tan(\theta/2)[\tan^2(\theta/2) + 5], \\ a_0 &= -0.5\tan(\theta/2)\sec^2(\theta/2). \end{aligned}\right\} \tag{12}$$

Eqs. (12) are obtained by substituting $\varepsilon = \exp(-j\theta)$ into Eqs. (15), (18), (19) and (23) of [11] and applying several trigonometric identities.

Finally, the angle at which $\delta_p = \pm\pi$ [12] (at vertical transitions shown in the bottom part of Fig. 2) is given by:

$$\phi(\delta_p = \pm\pi) = \sin^{-1}\sqrt{0.5\sec\theta}. \tag{13}$$

This angle exists only within the limited range $0 < \theta < 60^\circ$.

In Fig. 7, the four special angles of incidence $\phi_{pB}, \phi_{2B}, \phi_{PA}$ and $\phi(\delta_p = \pm\pi)$, calculated from Eqs. (8) – (13), are plotted as functions of θ. As $\theta \to 0$ (i.e., for a vanishing optical interface) all angles converge to $\phi = 45^\circ$, which is represented by the horizontal dotted line in Fig. 7. Note that $\phi_{pB} < 45^\circ$ for all QIM interfaces; the four angles diverge apart as θ increases; and $\phi_{pB} < \phi_{2B} < \phi_{PA}$ over the full range $0 < \theta < 180^\circ$; an order that holds true for all values of complex ε.

Table 1 lists ϕ_{pB}, ϕ_{2B} and ϕ_{PA} for values of θ from 0° to 180° in equal steps of 30°. The fourth angle $\phi(\delta_p = \pm\pi)$ is not included, as it is readily obtained from Eq. (13).

All calculations and figures presented in this paper are obtained using Matlab [13]. The precision of determining the angles presented in Table 1 is better than 0.01°.

5. Conclusion

Detailed analysis of the reflection of p- and s-polarized light by quasi-index-matched (QIM) dielectric-conductor interfaces of unit-magnitude relative dielectric function, $\varepsilon = \exp(-j\theta), 0 \le \theta \le \pi$, is presented. Figures 1, 3 and 5 show the complex-plane trajectories of r_p, r_s and ellipsometric function $\rho = r_p/r_s = \tan\psi\exp(j\Delta)$, respectively, as ϕ increases from 0 to 90° at discrete values of θ in the range $0 \le \theta \le 180^\circ$.

Amplitude reflectances $|r_p|$, $|r_s|$, their ratio, $|\rho| = |r_p/r_s| = \tan\psi$ and reflection phase shifts $\delta_p = \arg(r_p)$, $\delta_s = \arg(r_s)$ and $\Delta = \delta_p - \delta_s$ are shown in Figs. 2, 4 and 6, respectively, as functions of ϕ at constant values of θ.

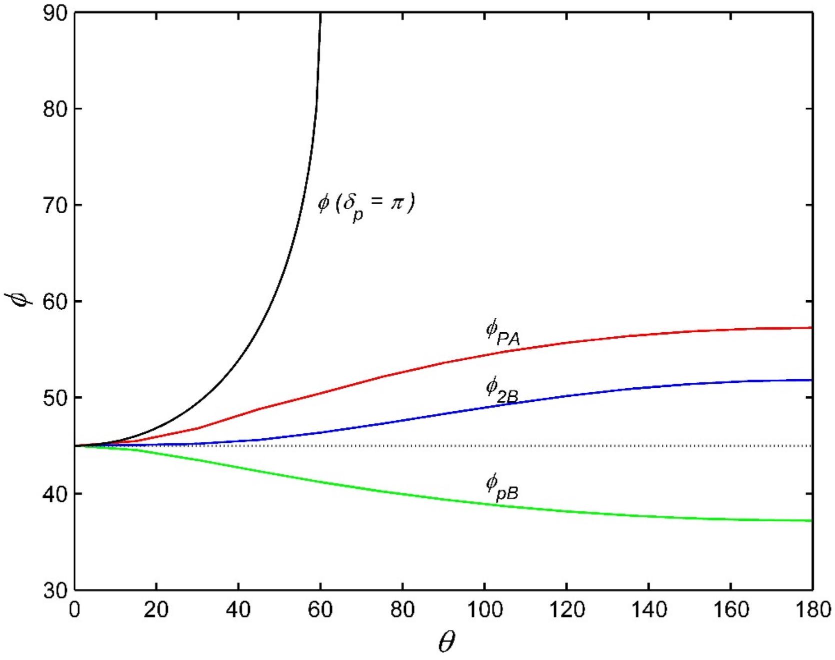

FIG. 7 Special angles of incidence ϕ_{pB}, ϕ_{2B}, ϕ_{PA} and $\phi(\delta_p = \pm\pi)$, of light reflection at QIM interfaces, calculated from Eqs. (8) - (13), are plotted as functions of θ. All angles are in degrees.

TABLE 1. Pseudo-Brewster angle ϕ_{pB} of minimum $|r_p|$, second-Brewster angle ϕ_{2B} of minimum $|\rho|$ and principal angle ϕ_{PA} at which $\Delta = \pi/2$ of QIM interfaces at selected values of θ (top row). All angles are in degrees.

$\theta \Rightarrow$	0	30	60	90	120	150	180
ϕ_{pB}	45.00	43.52	41.22	39.41	38.17	37.46	37.23
ϕ_{2B}	45.00	45.20	46.36	48.30	50.16	51.40	51.83
ϕ_{PA}	45.00	46.79	50.44	53.60	55.69	56.86	57.24

Finally, the pseudo-Brewster angle ϕ_{pB} of minimum $|r_p|$, the second-Brewster angle ϕ_{2B} of minimum $|\rho|$, the principal angle ϕ_{PA} at which $\Delta = \pi/2$ and the angle at which $\delta_p = \pm\pi$ are plotted in Fig. 7 as functions of θ for all possible QIM dielectric-conductor interfaces.

The results presented in this paper illustrate the physical optics aspects of light reflection by a unique set of interfaces with unit complex relative dielectric function. Light reflection by nearly vanishing interfaces is represented by the curves for $\theta = 0.1^\circ$ in Figs. 1 – 6. Examples of QIM interfaces in different parts of the optical spectrum are given in Appendix A.

Appendix A: Examples of QIM Interfaces

1. At the IR wavelength $\lambda = 3\mu m$, fused silica is transparent with refractive index n = 1.4193 (calculated from a dispersion relation given by Malitson [14]) and water is absorbing with complex refractive index $N = n - jk = 1.371 - j0.272$ at 25°C (from the tabular data of Hale and Querry [15]). The fused silica-water interface is characterized by $\varepsilon = (N/n)^2 = 0.9699\exp(-j22.443^\circ)$, so that QIM is almost satisfied. It may be possible to achieve $|\varepsilon| = 1$ by changing temperature.

2. At the visible wavelength $\lambda = 500$ nm, QIM is satisfied at the interface between a transparent liquid with n = 2.060 (e.g. Cargille Optical Liquid Series EH [16]) and Au substrate with $N = 0.8472 - j1.8775$ (interpolated form data given by Lynch and Hunter [17]); for such interface $\varepsilon = 0.9998\exp(-j131.427^\circ)$.

3. Metals have fractional optical constants $\varepsilon_r = n^2 - k^2$ and $\varepsilon_i = -2nk$ in the vacuum ultraviolet (VUV). Fig. 8 shows the real part ε_r, imaginary part, $-\varepsilon_i$ and absolute value, $abs(\varepsilon)$, of the complex dielectric function ε of Au *versus* wavelength λ in the 36 to 46 nm spectral range [17]. QIM ($abs(\varepsilon) = 1$) at the vacuum-Au interface is satisfied at point M at $\lambda = 39.1 nm$.

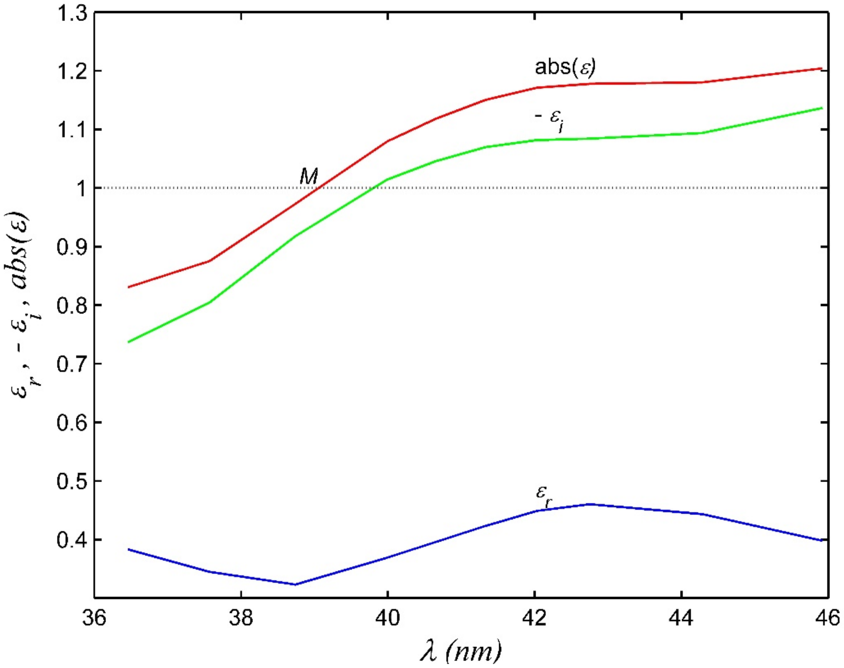

FIG. 8. Real part, ε_r, imaginary part, $-\varepsilon_i$ and absolute value, abs(ε), of the complex dielectric function of Au, $\varepsilon = (n - jk)^2$, are plotted *versus* wavelength λ in the 36-to-46 nm VUV spectral range. QIM is satisfied at point M. Optical constants n and k of Au are those of [15].

References

[1] Azzam, R.M.A. and Alsamman, A., Appl. Opt., 47 (2008) 3211.

[2] Muller, R.H., Surf. Sci., 16 (1969) 14.

[3] Azzam, R.M.A. and Bashara, N.M., "Ellipsometry and Polarized Light" (North-Holland, Amsterdam, 1987).

[4] Lekner, J., "Theory of Reflection" (Martinus Nijhoff, Dordrecht, 1987).

[5] Tompkins, H.G. and Irene, E.A., Eds., "Handbook of Ellipsometry" (William Andrew, Inc., Norwich, New York, 2005).

[6] Humphreys-Owen, S. P. F., Proc. Phys. Soc. London, 77 (1961) 949.

[7] Holl, H.B., J. Opt. Soc. Am., 57 (1967) 683.

[8] Kim, S.Y. and Vedam, K., J., Opt. Soc. Am. A, 3 (1986) 1772.

[9] Azzam, R.M.A. and Ugbo, E., Appl. Opt., 28 (1989) 5222.

[10] Azzam, R.M.A., J. Opt. Soc. Am., 71 (1981) 1523.

[11] Azzam, R.M.A., J. Opt. Soc. Am., 73 (1983) 1211.

[12] Azzam, R.M.A., J. Opt. Soc. Am., 69 (1979) 487.

[13] www.mathworks.com/products/matlab.

[14] Malitson, I.H., J. Opt. Soc. Am., 55 (1965) 1205.

[15] Hale, G.M. and Querry, M.R., Appl. Opt., 12 (1973) 555.

[16] www.cargille.com/opticalintro.shtml.

[17] Lynch, D.W. and Hunter, W.R., in "Handbook of Optical Constants of Solids" Palik, E. D., Ed. (Academic Press, New York, 1985).

الاستنتاجات

أظهرت النتائج أنّ استخدام الطريقة الرقمية التي تم عرضها في هذا البحث يوفر سرعة ودقة مضافة في عمليات تعداد الآثار وقياس أقطارها. وفّرت الطريقة الجديدة التي أعتمدت المعالجة الصورية باستخدام البرمجة بلغة Matlab في بناء برمجياتها سرعة كبيرة جداً في حساب عدد الآثار النووية الموجودة على وحدة السطوح للكاشف بالمقارنة مع طريقة التعداد اليدوية. أما فيما يتعلق بالدقة، فإن الطريقة الرقمية التي تتحدد دقتها بأبعاد pixel وفرت دقة تفوق عدة أضعاف الدقة التي يتم الحصول عليها يدوياً والتي يحدّدها سمك شعيرة (تدريجة) القياس للمايكروسكوب المستخدم. كما أنّ السرعة والدقة التي تميزت بها الطريقة الرقمية أدّتا إلى إمكانية إجراء عدد كبير من القياسات تحت ظروف مختلفة، وساعدت نتائجها في التوصل إلى علاقات تجريبية لأقطار الآثار مع متغيرات عدة: كطاقة الجسيمات، وزمن القشط، ودرجة حرارة محلول القشط.

المراجع

[1] Al-Jubbory, M.M.S., M. Sc. Thesis, Physics Dept., College of Education, University of Mosul, Iraq (2004).

[2] Ramakumar, K.L., "Interaction of Radiation with Matter", Ed. Rama Rao, G.A., III(3), (IANCAS Bulletin, 2004), pp. 189-192.

[3] Al-Jumaely, F.M.A., Ph.D. Thesis, Physics Dept., College of Science, University of Mosul, Iraq (2009).

[4] Yu, K.N., Ng, F.M.F. and Nikezic, D., Radiat. Meas., 40 (2005) 380.

[5] Al-Jubbori, M.A.D., Ph.D.Thesis, Physics Dept., College of Education, University of Mosul, Iraq (2004).

[6] Patiris, D.L., Blekas, K. and Ioannides, K.G., Comp. Phys. Comm., 177 (2007) 329.

[7] Sinenian, N., Rosenberg, M.J., Manuel, M.J.E., McDuffee, S.C., Casey, D.T., Zylstra, A.B., Rinderknecht, H.G., Gatu Johnson, M., Seguin, F.H., Frenje, J.A., Li, C.K. and Petrasso, R. D., Revi. Scien. Instr., 82(10) (2011) 103303.

[8] Cassou, R.M. and Benton, E.V., Nucl. Track. Detect., 2 (1988) 173.

[9] Sadowski, M., Al-Mashhadani, E.M., Szydlowski, A.T., Czyzewki, T., Glowacka, L., Jaskola, M., Rolfs, C. and Wielunski, M., Radiat. Meas., 25(1-4) (1999) 175.

[10] Dwaikat, N., El-hasan, M., Sueyasu, M., Kada, W., Sato, F., Kato, Y., Saffarini, G. and Iida, T., Nucl. Instr. and Meth. in Phys. Res. B, 268 (2010) 3351.

[11] http://www.mathworks.com/matlabcentral/fileexchange/4492 0-cr- 39-d1

[12] El Gazaly, M., Radia. Eff. and Deff. in Soli, 167 (6) (2012) 421.

[13] Patiris, D.L., Blekas, K. and Ioannides, K.G., Nucl. Instr.and Meth.in Phys.Res. B, 244 (2006) 392.

[14] Al-Jubbori, M.A., Raf. J. Sci., 25(1) (2014) 120.

يتضح من الشكل (6-a) أنّ مواءمة المعلْمة A_1 غالباً تكون دالة أسيّة تناقصية، وهذا منطقي؛ إذ عند زمن قشط ثابت فإنّ أقطار جسيمات ألفا تقل بزيادة طاقة الجسيم. أما فيما يخص المعلْمة A_2 فتكون العلاقة أقرب إلى الدالة الخطية. لذا اُستنبطت معادلات المعلْمتين أعلاه دالة للطاقة كما يلي:

$$A_1 = a_1 \exp(-a_2 E) \tag{2}$$

$$A_2 = a_3 E + 0.72 \tag{3}$$

ومن الممكن كتابة المعادلة (1) دالة لزمن القشط t وطاقة الجسيم E بدلالة المعلْمات الجديدة a_1, a_2, a_3 .

$$D(t,E) = a_1 \exp(-a_2 E) \times t^{a_3 E + 0.72} \tag{4}$$

المعلْمات الثلاث اُختيرت بحيث تكون لها القيم نفسها للطاقات المستخدمة. وفي بحثنا هذا كانت قيم هذه المعلْمات:

$$\left.\begin{aligned} a_1 &= 7.1671\mu m, \\ a_2 &= 0.4913 MeV^{-1} \\ a_3 &= 0.1 MeV^{-1} \end{aligned}\right\}$$

إنّ لدرجة حرارة المحلول القاشط تأثيراً على سرعة عملية القشط [14]. ولدراسة هذا التأثير على أقطار آثار جسيمات ألفا أُخذت أربع عينات من كاشف CR-39 وشُعِعَتْ بجسيمات ألفا بطاقة 3.1MeV. قشطت العينات بمحلول NaOH بعيارية 6.25N وبمدى درجات حرارة (70-85)°C بزيادة تتابعية مقدارها 5°C. ولإيجاد معادلة لأقطار جسيمات ألفا دالة لدرجة حرارة المحلول القاشط، رسم تغير هذه الأقطار مع زمن القشط لدرجات الحرارة (70, 75, 80, 85)°C بالطريقة نفسها المتبعة في الوصول لمعادلة الأقطار دالة للطاقة. وقد تم الوصول إلى معادلة أخرى تربط بين الأقطار ودرجة حرارة المحلول القاشط ولها شروط المعادلة (1) نفسها؛ أي أنّها تحقق $D(t=0, T=0) = 0$. ويمكن أنْ تعطى هذه المعادلة بالصيغة التالية:

$$\left.\begin{aligned} &D(t,T) = \\ &(-b_1 T + 2200)(1 - \exp(-(b_2 \exp(b_3 T))t)) \end{aligned}\right\} \tag{5}$$

حيث T درجة حرارة المحلول القاشط وt زمن القشط. أما قيم المعلْمات b_1, b_2, b_3 فهي كما يلي: $b_1=19\mu m/^{o}C$, $b_2=6.028\times10^{-7}$ and $b_3=0.1149^{o}C^{-1}$.

يبين الشكل (7) تغير أقطار آثار جسيمات ألفا لدرجات حرارة مختلفة للمحلول القاشط. ويتضح من الشكل أنّ التوافق جيد بين قيم الأقطار المقاسة (العملية) وحسابات المعادلة (5)؛ إذ تدل الإشارات الملونة على القيم العملية في حين تدل الخطوط الملونة على نتائج المعادلة (5).

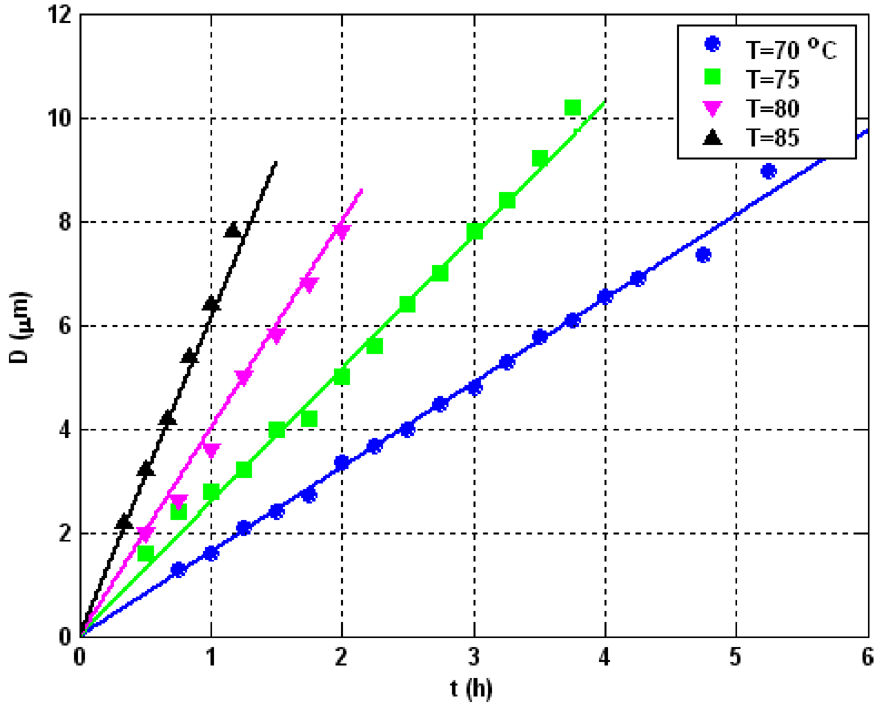

الشكل (7): تغير أقطار آثار جسيمات ألفا بدلالة زمن القشط لدرجات حرارة مختلفة للطاقة 3.1MeV وعيارية 6.25N للمحلول.

1- يجب أنْ تحقق المعادلة المقترحة زيادة قطر جسيم ألفا بزيادة زمن القشط.

2- عند زمن قشط وطاقة مساوييْن للصفر، يجب أنْ يكون القطر مساوياً للصفر أيضاً $D(t=0, E=0) = 0$.

وعلى هذا الأساس، فقد تم اختيار معادلة من النوع:

$$D(t) = A_1 t^{A_2} \qquad (1)$$

A_1 وA_2 معلمات حرة تعتمد فقط على طاقة الجسيم الساقط. أُجريت عملية المواءمة للمعادلة (1) لإيجاد قيم المعلمات الحرة للطاقات المستخدمة في هذا البحث (2.0, 2.5, 3.1) MeV باستخدام برنامج Matlab الذي يعطي درجة ثقة لإجراء المواءمة تزيد على 95%. ولكي تكون المعادلة (1) أكثر فائدةً، يجب أنْ يؤخذ بعين الاعتبار اعتماد المعْلمتين A_1 وA_2 على الطاقة كما هو موضح في الشكل (6).

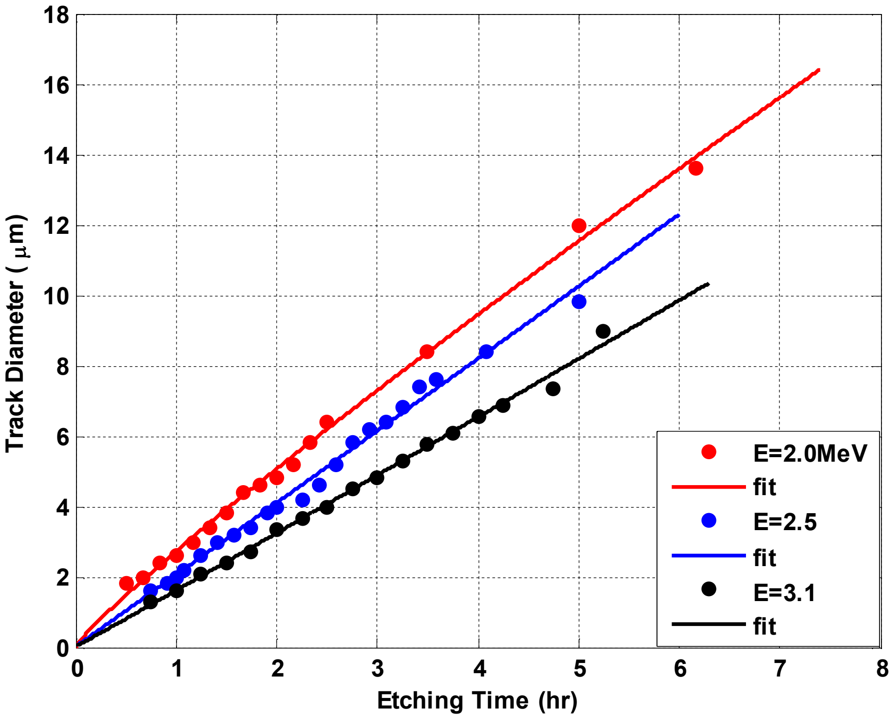

الشكل(5): تغير أقطار آثار جسيمات ألفا مع زمن القشط.

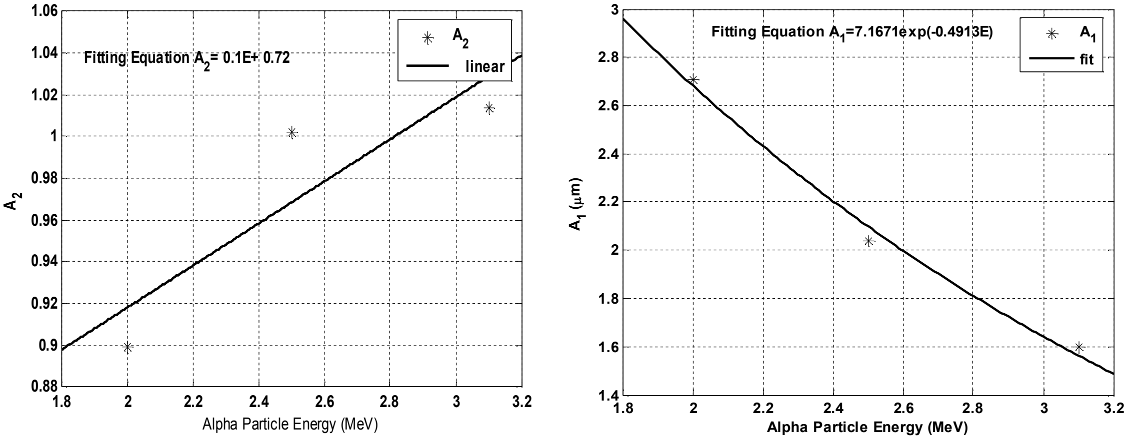

(b) (a)

الشكل(6): تغير المعْلمتين A_1 وA_2 مع طاقة جسيمات ألفا.

ولغرض التأكد من صحة أداء البرنامج وكفاءته، فقد تم إجراء مقارنة بين البيانات المستحصلة عن طريق استخدام البرنامج وتلك التي تم الحصول عليها بالطريقة اليدوية. ويوضح الجدول (1) نتائج هذه المقارنة. وتظهر هذه النتائج توافقاً جيداً بين الطريقتين ضمن حدود الخطأ التجريبي للطريقة اليدوية الذي لا يقل عن 10% في أحسن الأحوال. إضافة لذلك، فإنّ هذه النتائج جاءت متوافقة مع النتائج المستقلة المنشورة [12] (El Ghazaly) لآثار جسيمات ألفا عند الطاقات وأزمان القشط نفسها كما هو مبين في الشكل (4)، إذ إن El Ghazaly استخدم في بحثه شروط القشط نفسها من تركيز محلول NaOH ودرجة حرارته (6.25N,T=70°C). أما فيما يخص نتائج (Patiris *et al.*) [13]، فنلاحظ أنّ هنالك انحرافاً بسيطاً؛ إذ استخدموا شروط قشط مغايرة: NaOH (6N,T=75°C).

الجدول(1): مقارنة بين الطريقتين اليدوية والرقمية لبعض أقطار آثار ألفا.

E_α (MeV)	Etching Time, t (hr)	Diameter, D (µm)	
		Manual System	Digital System
2.0	2	5.20±0.30	4.80±0.05
2.5	2	4.50±0.23	4.00±0.02
3.1	4	6.75±0.15	6. 50±0.01

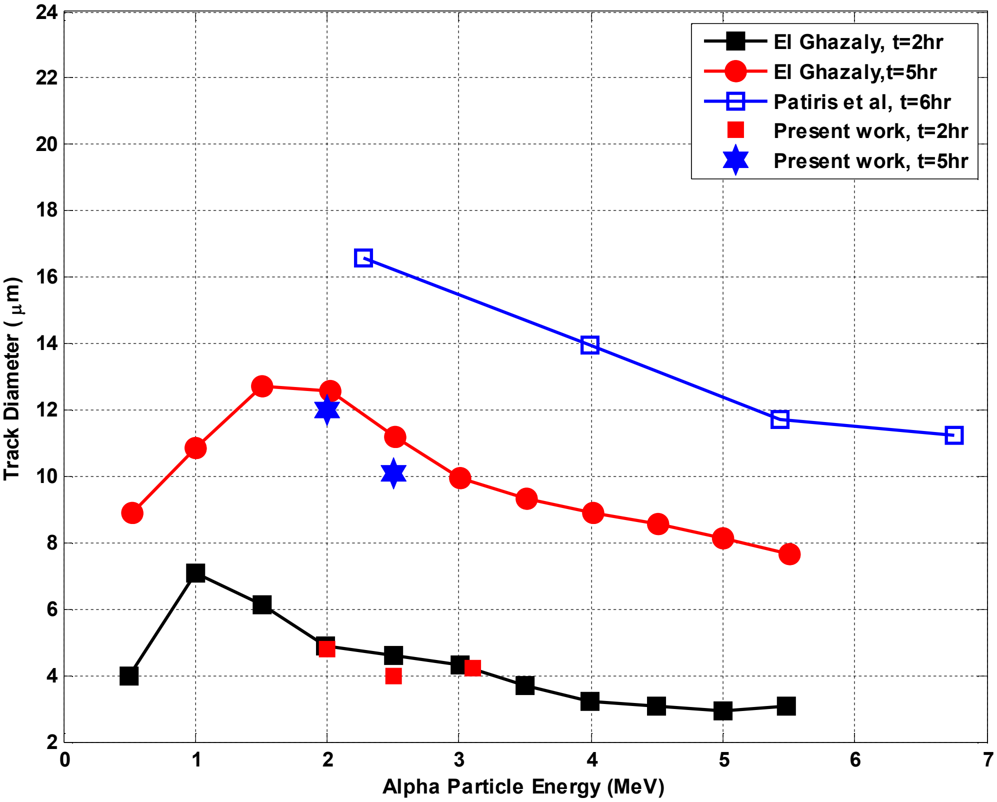

الشكل (4): مقارنة بين القياسات الحالية وقياسات El Ghazaly [12] و Patiris *et al.* [13] لأقطار آثار جسيمات ألفا.

النتائج والمناقشة

بعد التأكد من أداء البرنامج الحاسوبي، تم استخدامه لقياس تطور أقطار الآثار مع كل من زمن القشط ودرجة حرارة المحلول القاشط، بهدف محاولة وضع علاقة تجريبية بين أقطار الآثار وكل من طاقة الجسيمات وزمن القشط ودرجة حرارة المحلول.

ولأجل الوصول إلى معادلة تربط الأقطار بطاقات جسيمات ألفا وزمن القشط، تم رسم هذه الأقطار كدالة لزمن القشط للطاقات الثلاث التي تمت دراستها في الشكل (5). إنّ أي علاقة من هذا النوع يجب أنْ تأخذ بعين الاعتبار وجوب تحقيقها للشروط الفيزيائية التالية:

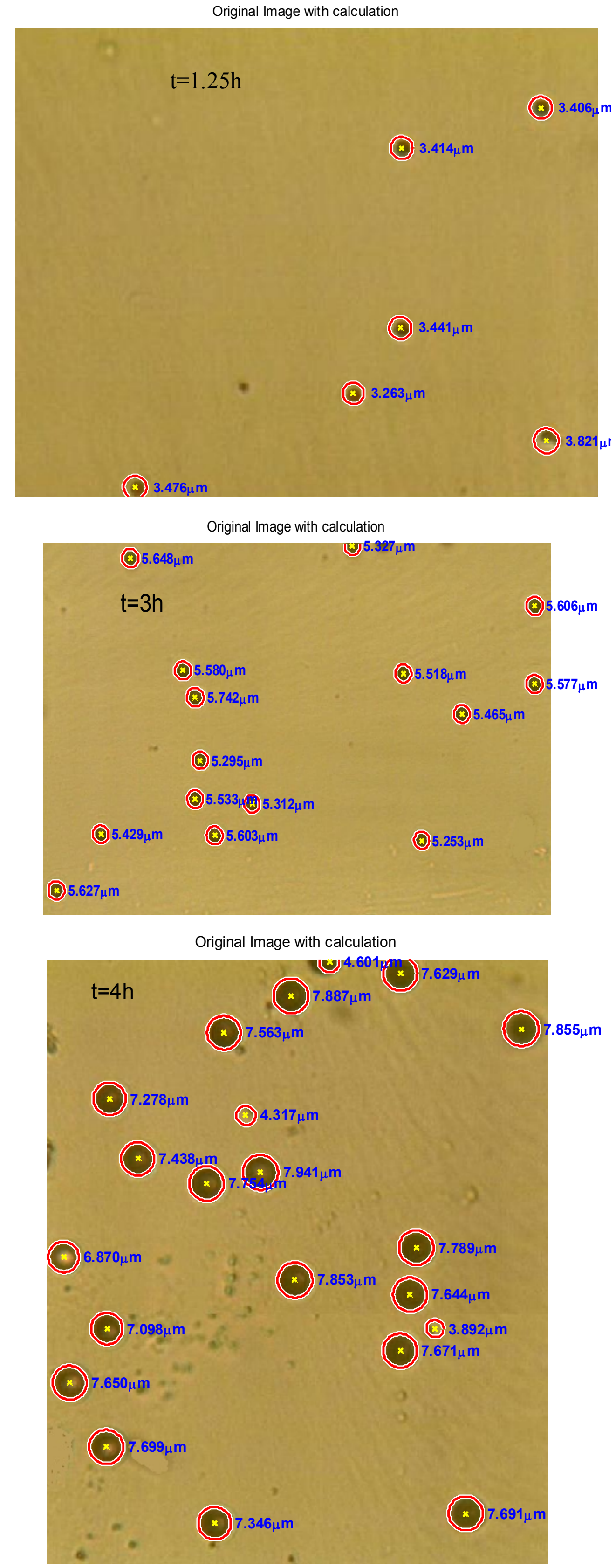

الشكل (3): عدّ الآثار وقياس أقطارها للطاقة 2MeV ولأزمان قشط مختلفة عند درجة حرارة $70^{o}C$.

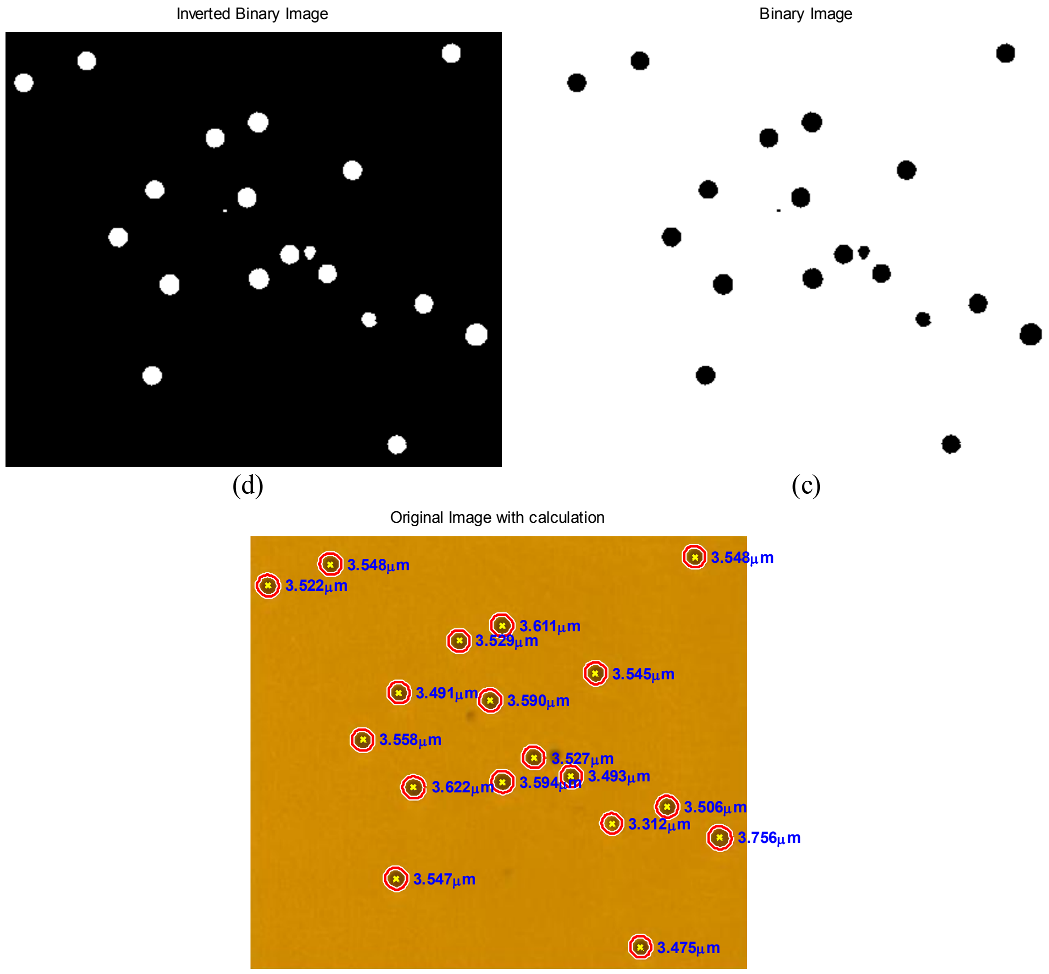

(d) (c)

(e)

الشكل (1): مراحل قراءة الآثار المتكونة في الكاشف CR-39 وعدّها وقياسها للطاقة 3.1 MeV وزمن قشط 2hr.

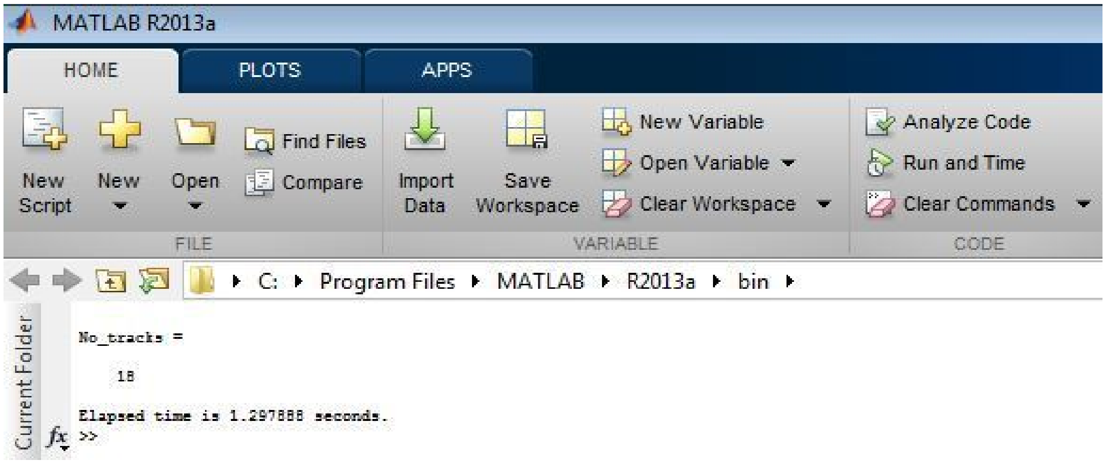

```
No_tracks =

    18

Elapsed time is 1.297888 seconds.
>>
```

الشكل (2): مخطط طباعة عدد الآثار والوقت المستغرق لتنفيذ البرنامج.

بعد التأكد من توافق نتائج البرنامج مع النتائج اليدوية ومدى صحة عملِه، التقطت صور لآثار مختلفة ولأزمان قشط مختلفة. ويتضح من الشكل (3) أنَّ الأقطار في بدايات عملية القشط تكون صغيرة، أما في مراحل متقدمة من عملية القشط، فإنَّ هذه الأقطار تزداد تباعاً.

المناطق التالفة لإظهار الآثار المتكونة، استُخدام محلول هيدروكسيد الصوديوم NaOH بتركيز 6.25N ودرجة حرارة (70±1) ^{o}C للطاقتين (2.0, 2.5) MeV. وفي حالة العينات المُشعَعة بطاقة 3.1 MeV (المجموعة الثانية) استخدمَ تركيز المحلول نفسه 6.25N لكن بمدى مختلف لدرجات الحرارة (70-85)^{o}C بزيادة تتابعية مقدارها 5^{o}C، وذلك لدراسة تأثير درجة حرارة المحلول القاشط على أقطار الآثار. ولأخذ صور للآثار المقشوطة وقياس أقطارها، تم ربط الكاميرا الرقمية من نوع (OPTIKAM 4083.B5) مع المجهر الضوئي من نوع (OPTIKA B-193) الذي يعمل ضمن برنامج معين لغرض نقل صور الآثار مباشرة إلى الحاسوب الشخصي PC حيث يتم إجراء عمليات القياس عليها باستعمال تقنية التحليل الصوري من خلال البرنامج الحاسوبي الذي تم إعداده.

2- المعالجة الصورية الحاسوبية

تمت كتابة برنامج حاسوبي بلغة Matlab2012 لعدّ أثار جسيمات ألفا المتكونة على سطح الكاشف وقياس أقطارها، وسُمي هذا البرنامج "CR-39-D1" وهو متوفر الآن على موقع تبادل الملفات الخاص بـ Matlab من خلال الرابط التالي حيث يتم تحميل هذا البرنامج [11] http://www.mathworks.com/matlabcentral/fileexchange/44920-cr-39-d1

يقوم البرنامج ***"CR-39-D1"*** بتحميل الصورة وقراءتها آلياً، وهذا موضح في الشكل (1-a). ومن خلال دوال متحسسة في لغة Matlab كدالة Gray تحول الصورة إلى اللون الرمادي لكي يتسنى للبرنامج تحسس الآثار النووية كما في الشكل (1-b). أما الشكل (1-c) فيبين صور الآثار النووية بعد معالجتها من البرنامج لكي تصبح صورة ثنائية اللون، ومن ثم أخذ معكوس الصورة ثنائية اللون حيث يتم تحويل الخلفية من البيضاء إلى السوداء، وذلك لكي يتمكن البرنامج من عزل الآثار عن الشوائب (الخلفية الإشعاعية) الموجودة في الكاشف، وهذا موضح في الشكل (1-d)، وبعدها يقوم البرنامج بعدّ الآثار وقياس أقطارها من خلال الدالة Center التي تسمح بتحسس الأشكال الدائرية وقياس أقطارها. والخطوة الأخيرة في البرنامج هي إعادة قراءة الصورة الأصلية وطباعة قطر كل أثر من هذه الآثار على الصورة الأصلية وكتابة عبارة (original image with calculation) للتأكد من أنها الصورة النهائية للكاشف، وهذا مُوضح في الشكل (1-e). ولا تستغرق عملية المعالجة وإجراء العد والحسابات سوى بضع ثوان حسب عدد الآثار. يُظهر الشكل (2) الزمن المستغرق في تنفيذ البرنامج من خلال طباعة دوال حساب الزمن المستغرق في تنفيذ البرنامج على الشاشة الخاصة بماتلاب (Work Space) (عدّ الآثار وقياس أقطارها وطباعتها).

أظهرت عمليات تعداد الآثار تطابقاً جيداً بين الطريقتين الحاسوبية واليدوية، في حين أنّ الدقة في قياس الأقطار بالطريقة الحاسوبية متفوقة كثيراً على نظيرتها اليدوية؛ إذ إنّ دقة الأولى تكون بحدود البكسل (Pixel). وكمثال على ذلك، فإنّ صورة لمشهد 1mm x 1mm مأخوذة بحجم 10000 x 10000 pixels ستوفر دقة في القياس تصل إلى 0.1 مايكرون، وهي دقة كبيرة بالمقارنة بالقياس اليدوي التي تصل دقته إلى حوالي 1 مايكرون.

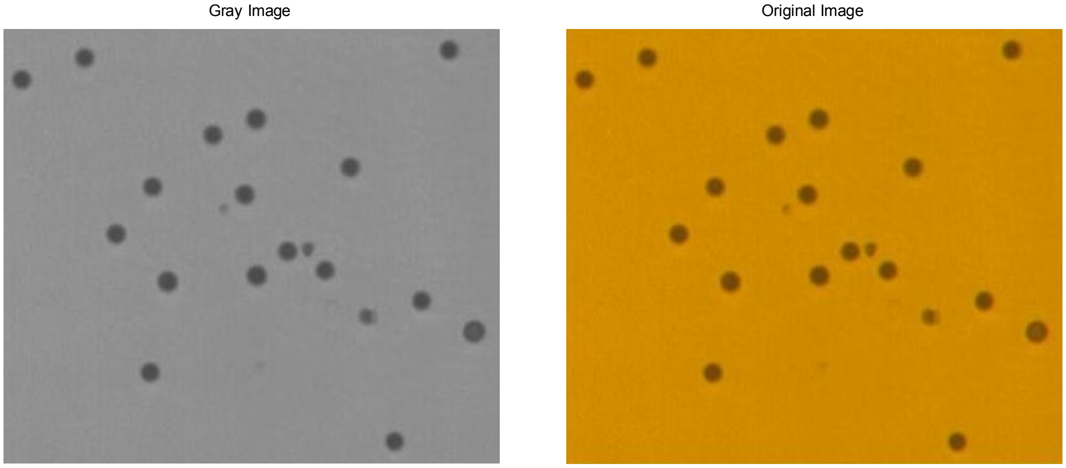

(a) (b)

المقدمة

تتباين كفاءة الأنواع المختلفة من كواشف الأثر النووي في التحسس بالجسيمات الساقطة عليها تبايناً كبيراً. وتعتمد هذه الكفاءة أيضاً على نوع الجسيم الساقط وطاقته. وعلى الرغم من أنّ الكواشف الإلكترونية بمختلف أنواعها تتمتع بخصائص أفضل في مجال الاستخدام بهدف كشف نوعية الجسيمات وطاقاتها، فإن اللجوء إلى استخدام الكواشف البلاستيكية ككواشف LR-115, CN-85, CR-39, PM قد يكون أكثر ملاءمة في بعض التطبيقات والاستخدامات [1-4] المتعلقة بمراقبة التلوثات الإشعاعية لفترات طويلة، وذلك لسهولة استخدامها وعدم حاجتها إلى أجهزة إلكترونية ومجهزات قدرة...إلخ. وعلى الرغم أيضًا من أنّ قدرة التمييز للطاقات المختلفة لهذه الكواشف هي محدودة جداً، فإنها في الوقت نفسه تتمتع بكفاءة كشف عالية جداً تقترب من 100%، إذ إن معظم الجسيمات المادية أو جميعها كالبروتونات وجسيمات ألفا والأيونات التي تسقط عليها تؤدي إلى تكوين آثار ثابتة في هذه الكواشف. وبذلك فإن المؤثر الرئيسي المهم في تحديد كفاءة الكاشف هو مدى فعالية العمليات والإجراءات المتبعة في إظهار تلك الآثار [5-7].

تتضمن عمليات إظهار الآثار في معظم الأحيان إجراء عملية القشط الكيميائي لفترات زمنية معينة بهدف إزالة جزيئات مادة الكاشف المتأثرة بالجسيمات المشحونة من خلال تحول تلك الجزيئات الخاملة إلى جذور كيميائية حرة يمكن إذابتها في محلول قاعدي عند درجات حرارة معينة. وقد أجريت الكثير من البحوث والدراسات المتعلقة بأنواع المحاليل المستخدمة ومديات درجات الحرارة لأنواع كثيرة من الجسيمات المشحونة ولفترات قشط مختلفة [8-10].

تعتبر كثافة الآثار المتكونة على الكاشف مقياساً مباشراً لشدة الإشعاعات المؤينة التي يكون الكاشف قد سبق أنْ تعرض لها. وعلى هذا الأساس، فإنّ مدى كفاءة عملية تعداد الآثار التي تُظهرها عملية القشط هو من العوامل الحاسمة في تحديد دقة القياسات. وتتم عملية التعداد هذه عادة بطريقة يدوية من خلال استخدام المجهر الضوئي الاعتيادي في تحديد عدد الآثار لكل وحدة مساحة للكاشف وكذلك قياس أقطار تلك الآثار، وهذا ما يسمى الطريقة اليدوية. وتتطلب هذه الطريقة جهداً بشرياً لا يُستهانُ به إضافة إلى إمكانيات حدوث أخطاء في أثناء عمليات العد والقياس.

لقد وفر التطور الكبير في برمجيات الحاسبات المختصة بالمعالجات الصورية في السنوات الأخيرة إمكانيات واسعة من أجل تطوير عمليات التعداد اليدوي للآثار في الكواشف النووية. ويتعلق هذا البحث بتطوير برنامج خاص يستخدم البرمجة بلغة MATLAB لتحقيق هذا الغرض. وقد تم استخدام هذه اللغة البرمجية، ليس فقط بسبب قدرتها الكبيرة في إجراء عمليات المعالجة الصورية، ولكن أيضًا لتمتعها بأدوات حسابات إحصائية ورياضية كبيرة بشكل يمكن من خلاله إجراء تحليلات إضافية للنتائج المستخلصة. كما يمكن أيضاً بسهولة تخزين النتائج الرقمية أو نقلها لتستخدم ضمن برمجيات شائعة أخرى مثل Microsoft Excel.

الجانب العملي

1- التشعيع والقشط

تم في هذا البحث استخدام كاشف الأثر النووي CR-39 بريطاني المنشأ من صنع شركة (Page Moldings Pershore UK) بسمك 200µm لقياس أقطار آثار جسيمات ألفا. والكاشف عبارة عن مادة بوليمرية بلاستيكية صلبة من نوع متعدد الكربون يمتاز بتجانس مادته وتماثل خواصه وبخلفيته الإشعاعية القليلة وحساسيته العالية للكشف عن الجسيمات المشحونة مثل جسيمات ألفا وكذلك الكشف عن النيوترونات. تم تقطيع هذا الكاشف إلى مجموعتين ذات أبعاد 1cm×1cm. وللحصول على صور أقطار الآثار لفترات قشط مختلفة جرى تشعيع الكاشف بجسيمات ألفا المنبعثة من مصدر ^{241}Am بطاقة قصوى 5.485MeV لها متوسط مدى في الهواء مقداره 4.16cm. ولأجل الحصول على طاقات مختلفة، تم تغيير المسافة بين المصدر المشع والكاشف من خلال منظومة تشعيع للحصول على الطاقات المستخدمة في هذا البحث. أخذت عدة عينات من الكاشف بواقع مجموعتين: جرى تعريض المجموعة الأولى المؤلفة من عينتين لجسيمات بطاقات (2, 2.5)MeV في حين شُعِعت المجموعة الثانية المكونة من أربع عينات بطاقة 3.1MeV بهدف إجراء دراسة جزئية لتأثير درجة حرارة محلول القشط على أقطار الآثار. وتضمنت عملية التشعيع استخدام منظومة بحيث تكون كمجمع لجسيمات ألفا من خلال ثقب صغير لا تتجاوز مساحته 1mm^2، وذلك لضمان السقوط العمودي لجسيمات ألفا على الكاشف CR-39. بعد قشط العينات لغرض حفر

المجلد 8، العدد 1، 2015. ص ص. 57-65

المجلة الأردنية للفيزياء

ARTICLE

برنامج حاسوبي لتعداد آثار جسيمات ألفا وقياس أقطارها في كاشف الأثر النووي CR-39

مشتاق عبد داود الجبوري و صلاح أحمد محمد الشميسي

قسم الفيزياء، كلية التربية للعلوم الصرفة، جامعة الموصل، الموصل، العراق.

Received on: 15/9/2014; Accepted on: 19/1/2015

الملخص: يتعلق البحث بتصميم برنامج حاسوبي بلغة Matlab-2012 واختباره يقوم بإجراء عمليات المعالجة الصورية لآثار جسيمات ألفا الساقطة على كاشف الأثر النووي CR-39، وذلك من خلال استخدام كاميرا رقمية متصلة بمايكروسكوب (مجهر). يقوم البرنامج بقياس أقطار الآثار كل على حِدة وتسجيل قيمة كل قطر على الصورة الرقمية وحساب معدل الأقطار وانحرافاتها المعيارية ضمن المشهد الواحد. كما يوفر البرنامج جهداً كبيراً بالمقارنة مع الطريقة اليدوية التقليدية المستخدمة في دراسة الآثار النووية، بالإضافة إلى زيادة الدقة في قياس الأقطار من خلال تجنب الأخطاء اليدوية الناتجة عن استخدام المايكروسكوب. يؤدي هذا البرنامج من خلال استخدامه في تحليل آثار جسيمات ألفا بطاقات 2, 2.5, 3.1 MeV على الكاشف CR-39 بعد عمليات القشط بمحلول NaOH 6.25 N بدرجة حرارة $(70\pm1)^{o}$C إلى التمكن من الوصول إلى معادلات تجريبية لوصف علاقة قطر الأثر مع كل من طاقة جسيمات ألفا ومع درجة حرارة محلول القشط.

الكلمات المفتاحية: كواشف الأثر النووي، نمذجة أقطار ألفا، معادلات تجريبية، CR-39، Matlab.

Computer Algorithm for Counting and Measuring Alpha Particles Track Diameters in CR-39 Detectors

Mushtaq Al-Jubbori and **Salah Al-Shumaisy**

Department of Physics, College of Education for Pure Science, Mosul University, Mosul, Iraq.

Abstract: This work is concerned with the design and test of a Matlab-2012 computer algorithm capable of performing image processing operations on digital images of alpha particles tracks on CR-39 detectors. The software measures the diameters of individual tracks separately and registers the measured value of each diameter on the digital picture. It also calculates the mean and standard deviation for all tracks within any particular view. In addition to the enhanced measurement accuracy resulting from the elimination of sources of human errors associated with microscope measurements, the software saves a great deal of manual effort compared with the method currently being used for the study of nuclear tracks. The use of the software in the analysis of 2, 2.5, 3.1 MeV alpha particles tracks on CR-39 detector etched with 6.25 N NaOH solution at $(70\pm1)^{o}$C resulted in the ability to reach some empirical relations describing the tracks diameters as functions of alpha particles energy and etching solution temperature.

Keywords: CR-39 detectors; Alpha diameters modeling; Empirical relations; Matlab.

Corresponding Author: Mushtaq Al-Jubbori **Email**: mushtaq_phy8@yahoo.com

[13] Balestra, S., Cozzi, M., Giacomelli, G., Giacomelli, R., Giorgini, M., Kumar, A., Mandrioli, G., Manzoor, S., Margiotta, A.R., Medinaceli, E., Partizii, L., Popa, V., Qureshi, I.E., Rana, M.A., Sirri, G., Spurio, M., Togo, V. and Valieri, C., Nucl. Instr. and Meth. in Physics Research, B254 (2007) 254.

[14] Chan, K.F, Ng, F.M.F., Nikezic, D and Yu, K.N, Nuclear Instruments and Methods in Physics Research, B263 (2007) 284.

[15] Ho, J.P.Y., Yip, C.W.Y., Nikezic, D. and Yu, K.N., Radiat. Meas., 36 (2003) 141.

[16] Randhaw, G.S., Shyam, K. and Virk, H.S., Radiat. Meas., 22(3) (1979) 523.

[17] Leonardi, F., Caresana, M., D'Alessandro, M., Mishra, R., Tonnarini, S., Trevisi, R. and Veschetti, M., Radiat. Meas., 44 (2013) 787.

[18] Szydlowski, A., Sadowski, M., Czyzewski, T., Jaskola, M., Kormona, A., Kedzierski, J. and Krestschmer, W., Radiat. Meas., 312 (1999) 257.

[19] Nikezic, D. and Yu, K.N., Materials Science and Engineers, R46 (2004) 51.

[20] Manzoor, S., Balestra, S., Cozzi, M., Errico, M. Giacomelli, G., Giorgini, M., Kumar, A., Margiotta, A., Medinaceli, E., Patrizii, L., Popa, V., Qureshi, I.E. and Togo, V., Nucl. Phys. Proc. Suppl., 172 (2007) 92. DOI:0.1016/j.nuclphysbps.2007.07.017

[21] Dörschel, B., Hermsdorf, D., Kadner, K. and Kühne, H., Radiat. Prot. Dosimetry, 78(3) (1998) 205.

[22] Azooz, A.A., Al-Nia'emi, S.H.S. and Al-Jubbori, M.A., Computer Physics Communications, 183 (2012) 2470.

[23] Al-Hubayti, Y.Y.K., Ph.D. Thesis, Department of Physics, College of Education, University of Mosul, Iraq (2013).

[24] Azooz, A.A., Al-Nia'emi, S.H.S. and Al-Jubbori, M.A., Radiation Measurements, 47 (2012) 67.

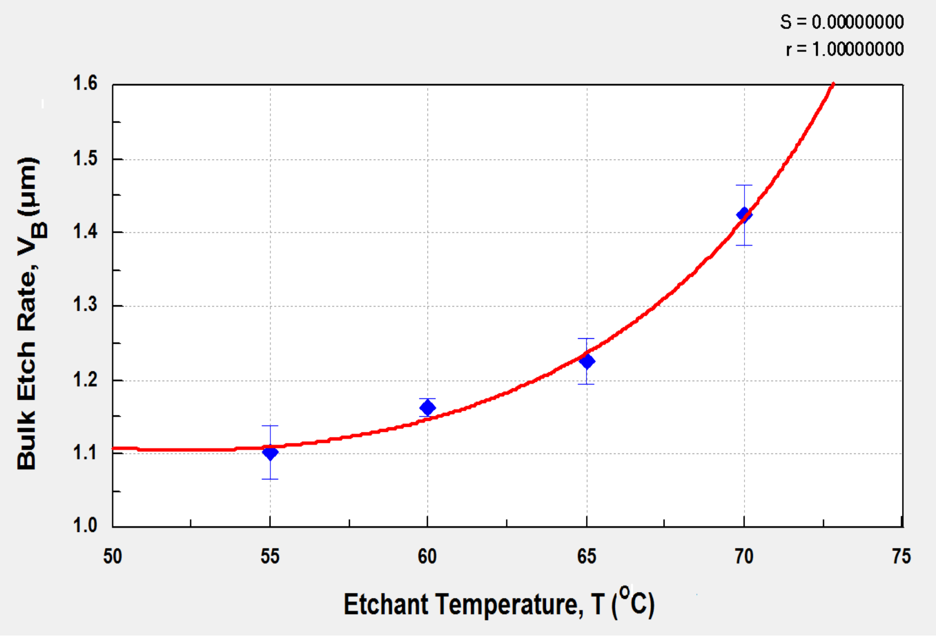

الشكل (6): العلاقة بين معدل القشط العام ودرجة حرارة المحلول القاشط.

الاستنتاجات

يلاحظ من النتائج أن رفع درجة حرارة المحلول القاشط يُحسِّن معدل القشط العام V_B حيث يؤدي إلى زيادته، ومن ثم إلى زيادة معدل قشط الأثر بالعمق مما يزيد من سرعة إظهار الأثر من خلال إزالة كميات أكثر من مادة الكاشف من السطح ومن المسار المتضرر للجسيم الساقط كلما زادت درجة حرارة المحلول القاشط. كذلك يلاحظ أن طريقة L_e-D لقياس V_B هي طريقة جيدة وتعطي نتائج دقيقة، لأنها تتعامل مع الصور الحقيقية للآثار المقشوطة المتكونة في الكاشف وقياس أطوالها وأقطارها مباشرة وبشكل دقيق. ويمكن استخدام المنحني بين معدل القشط العام ودرجة حرارة المحلول كمنحني معايرة لإيجاد معدل القشط العام عند أي درجة حرارة ضمن الظروف المستخدمة.

المراجع

[1] Pandey, A.K., Kalsi, P.C. and Iyer, R.H., Nucl. Instrum. and Meth. in Physics Research, B134 (1998) 393.

[2] Khayrat, A.H. and Durrani, S.A., Radiat. Meas., 25 (1995) 163.

[3] Tse, K.C.C., Ng, F.M.F. and Yu, K.N., Poly. Degradation Stability, 91 (2006) 2380.

[4] Tse, K.C.C., Nikezic, D. and Yu, K.N., Radiat. Meas., 43 (2008) S98.

[5] Vilensky, A.I., Zagorski, D.L., Kabanov, V.Ya. and Mchedlishvili, B.V., Radiat. Meas., 36 (2003) 131.

[6] Al-Hubayti, Y.Y.K., M.Sc. Thesis, Department of Physics., College of Education, University of Mosul, Iraq (2005).

[7] Ng, F.M.F. and Yu, K.N., Materials Chemistry and Physics, 100 (2006) 38.

[8] Jaleh, B., Parvin, P., Mirabaszadeh, K. and Katouzi, M., Radiat. Meas., 38 (2004) 173.

[9] Al-Nia’emi, S.H.S. and Khidher, N.S., Abhath Al-Yarmouk -Basic Sciences and Engineering, 15(1) (2006) 17.

[10] Al-Nia’emi, S.H.S. and Al-Obedy, A.A.I., Abhath Al-Yarmouk, Basic Sciences and Engineering, 12(1) (2003) 1.

[11] Al-Nia’emi, S.H.S. and Al-Obedy, A.A.I, Abhath Al-Yarmouk, Basic Sciences and Engineering, 13(2) (2004) 113.

[12] Al-Nia'emi, S.H.S. and Kasim, Y.Y., Jordan J. of Phys., 6(1) (2013) 17.

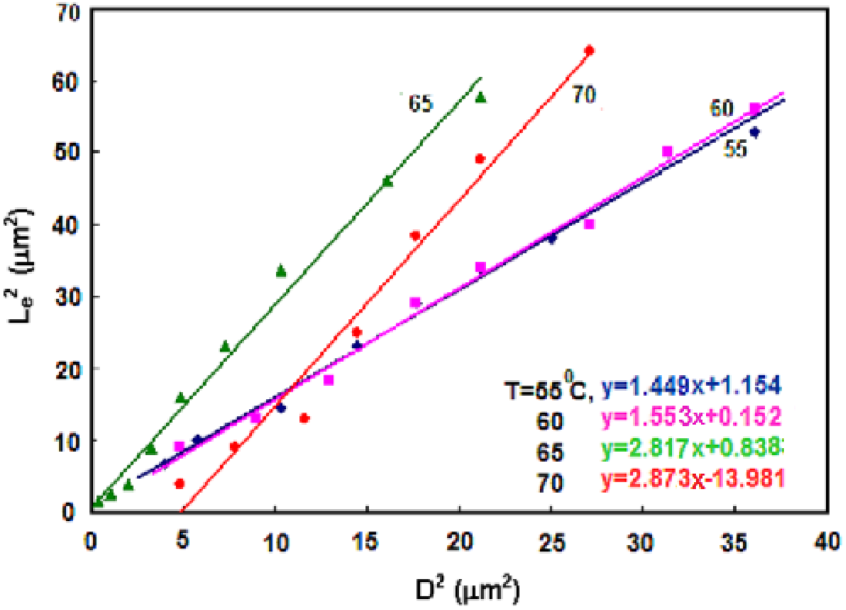

الشكل (5): العلاقة بين L_e^2 وD^2.

وعليه، فإن قياساتنا يجب أن تكون ضمن المرحلة الأولى لنمو الأثر، ويعزى السبب في ذلك إلى أن أطوال الآثار المتكونة L_e وكذلك المعدل الزمني لتغير طول الأثر (dL/dt) لا يستمران بالزيادة مع استمرار زيادة أقطار الآثار مع تقدم القشط، لأن ثبات طول الأثر يعني أن عمق الأثر (x) يصبح مساوياً لمدى الجسيم داخل الكاشف، وأن المدى المتبقي للجسيم داخل الكاشف [R'(=R-X)=0] يصبح مساوياً للصفر ويصبح الأثر تام القشط (etched-out). وعليه، فإن أيّ تقدم في عملية القشط بعد هذه النقطة على عمق أكبر من مدى الجسيم على طول امتداد مسار الجسيم خارج المسار المتضرر في المنطقة السليمة في الكاشف يؤدي إلى أن تكون قيمة المدى المتبقي للجسيم غير مقبولة لأنها تصبح سالبة. وفضلاً عن ذلك، فإن معدل قشط الأثر يهبط بشكل كبير ومفاجئ ليصبح مساوياً لمعدل القشط العام (V_T=V_B)، وتصبح نسبة معدل القشط مساوية للواحد (V=1) مهما استمرت عملية القشط في هذه المرحلة. ولهذا، فإنه لا يمكن إجراء قياسات لمعلمات الأثر في هذه المرحلة لأن المنطقة المقشوطة تقع خارج مدى الجسيم ولا تمثل الأثر الحقيقي الناتج من سقوط الجسيم على الكاشف بل تدعى حفرة القشط (etch pit) ولا يجوز إجراء قياسات عليها، لذا من المفروض التوقف عن القشط عند ثبات طول الأثر أو تشبعه وعدم الاستمرار لفترات أطول.

من نتائج الشكلين (4) و(5)، تم إيجاد معدلات القشط العام V_B من المعادلة (1) للكاشف CR-39 عند درجات حرارة مختلفة للمحلول القاشط كما هو موضح في الجدول (1). والشكل (6) يوضح العلاقة بين معدل القشط العام (V_B) ودرجة حرارة المحلول القاشط (T)، حيث يلاحظ أن معدل القشط العام يزداد بشكل أسي مع زيادة درجة حرارة المحلول القاشط؛ إذ إن زيادة درجة الحرارة تُسرّع التفاعل بين المحلول القاشط والكاشف وتزيد من ثم من معدلات قشط الكاشف. وباستخدام برنامج Curve Expert 1.3 لرسم العلاقة، فقد وُجد أنها تأخذ الصيغة الرياضية التجريبية الآتية:

$$V_b = (a+bT) / (1+cT+dT^2) \qquad (2)$$

$a = 119.139,\ b = -0.8395,\ c = 3.322,\ d = -0.0390.$

الجدول (1): معدل القشط العام بطريقة L_e-D عند درجات حرارة مختلفة للمحلول القاشط.

Temp. (°C)	V_B (µm h^{-1})
55	1.1022± 0.0363
60	1.1643 ± 0.0143
65	1.2255 ± 0.032
70	1.424 ± 0.0414

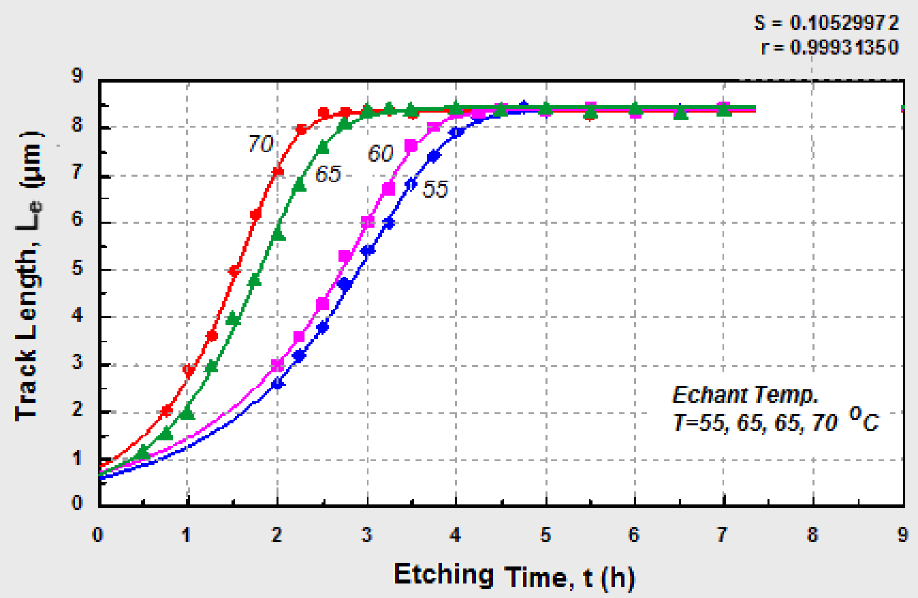

الشكل (3): تغير طول الأثر مع زمن القشط.

يُبيِّن الشكلان (4) و(5) العلاقة بين مربع قطر الأثر وحاصل ضرب الفترة الزمنية للقشط في طول الأثر المتكون خلال هذه الفترة $(L_e t, D^2)$ والعلاقة بين مربع قطر الأثر ومربع طوله (L_e^2 , D^2) لتلك الفترة الزمنية في درجات حرارة القشط المختلفة. يلاحظ من الشكلين أن العلاقة بين كل من $(L_e t , D^2)$ و(L_e^2, D^2) بشكل عام هي تقريباً علاقة خطية في مرحلة الشكل المخروطي المنتظم للأثر ذي الرأس المدبب (المرحلة الأولى من مراحل نمو الأثر)، لأن طول الأثر يزداد مع زيادة زمن القشط ويصل إلى الثبات أو حالة التشبع في نهاية هذه المرحلة الأولى عندما يصل رأس الأثر المقشوط إلى نهاية المسار المتضرر تحت نهاية مدى الجسيم في الكاشف. ويستمر طول الأثر ثابتًا مهما ازداد زمن القشط بعد الدخول في مرحلة القشط المفرط (المرحلة الثانية)، في حين يستمر قطر الأثر بالزيادة مع تقدم القشط في هذه المرحلة (القشط المفرط) خارج مدى الجسيم في الكاشف. وهذا ما تمت ملاحظته عند رسم أقطار الآثار مع زمن القشط في مرحلة القشط المفرط التي لم يتم تضمينها هنا لأنها لا تدخل في الحسابات.

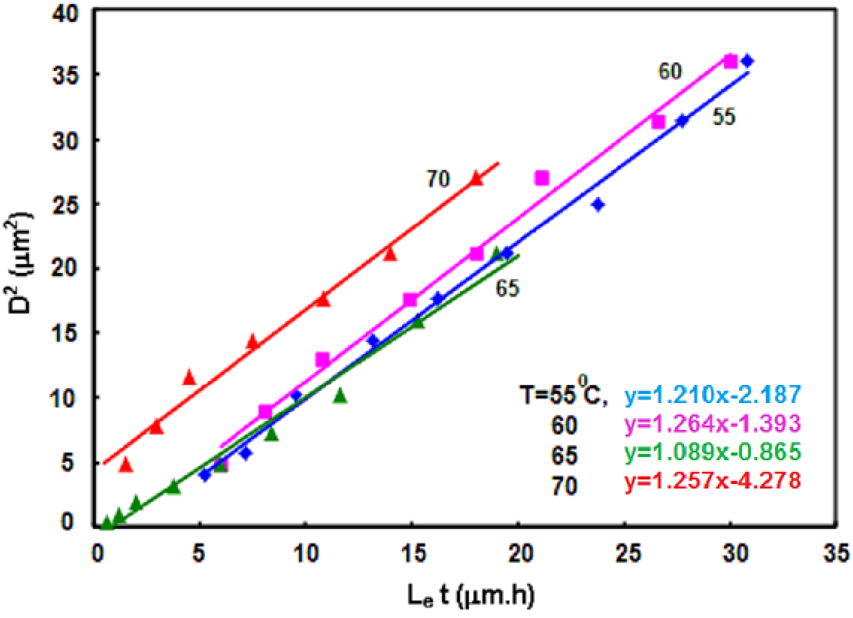

الشكل (4): العلاقة بين $L_e t$ وD^2.

النتائج والمناقشة

يبين الشكل (2) العلاقة بين قطر الأثر وزمن القشط، حيث يلاحظ أن أقطار الآثار تزداد مع زمن القشط، وان هذه الزيادة تختلف باختلاف درجة حرارة المحلول القاشط؛ إذ تكون أكبر عند درجات الحرارة الأعلى، ويستمر قطر الأثر بالزيادة مع تقدم القشط في مرحلة الأثر المخروطي المنتظم كما في الشكل وكذلك في مرحلة القشط المفرط خارج مدى الجسيم في الكاشف.

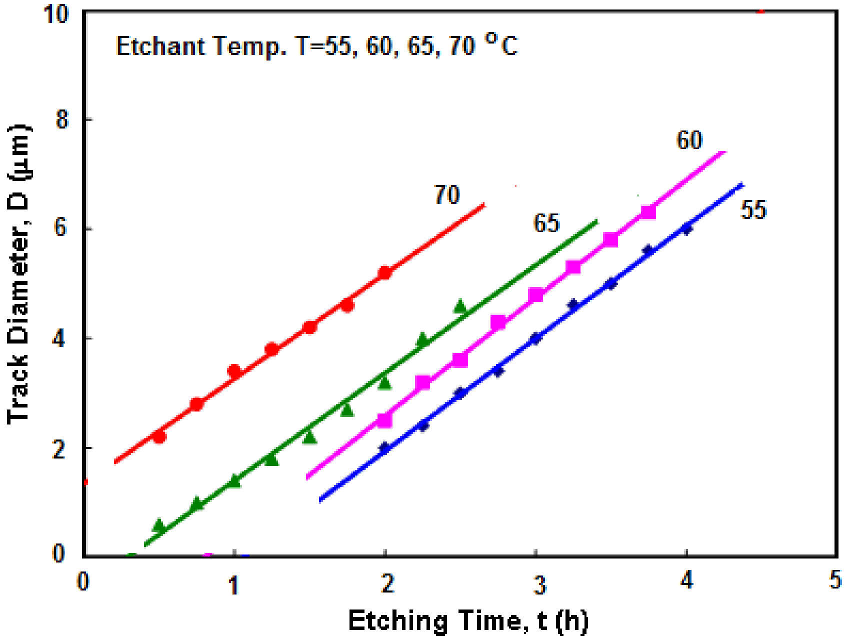

الشكل (2): تغير قطر الأثر مع زمن القشط.

يمثل الشكل (3) العلاقة بين طول الأثر(L) المقاس مباشرة وزمن القشط (t) في درجات حرارة مختلفة للمحلول الكيميائي القاشط. يلاحظ من الشكل أن طول الأثر ينمو لاخطياً وبصورة تدريجية مع تقدم عملية القشط وصولاً إلى أقصى قيمة له، التي تمثل نقطة التشبع أو نقطة ثبات تقابل ذروة براك (Bragg peak) التي بعدها يصبح معدل نمو طول الأثر مساوياً للصفر (ميل المنحني $\frac{dL}{dt} = 0$)؛ أي يصبح طول الأثر ثابتاً مهما تقدمت عملية القشط. وهكذا يدخل الأثر عندئذٍ في مرحلة القشط المفرط (المرحلة الثانية) خارج المسار المتضرر في المنطقة السليمة تحت نهاية مسار الجسيم في الكاشف، ويبدأ رأس الأثر المدبب بالاستدارة (rounded) وصولاً إلى الشكل الكروي للأثر مع تقدم عملية القشط حيث يقترب معدل قشط الأثر باتجاه عمق الأثر V_T من معدل القشط العام V_B وما يلبث أن يساويه بعد زمن قشط قليل جداً، وعندها يبدأ القشط بمعدل متساوٍ هو V_B في جميع الاتجاهات. إن نقطة ثبات طول الأثر أو نقطة التشبع تحدث مع وصول المحلول القاشط إلى نهاية المسار المتضرر وهي نهاية مدى الجسيم في الكاشف الذي يمثل وصول رأس الأثر المقشوط إلى هذه النقطة؛ إذ يكون الأثر الناتج خلال هذه المرحلة (وهي الأولى) مخروطي الشكل ذا نهاية مدببة (cone tip). وهذه النتائج تتوافق مع ما وجده [21، 22، 23].

يلاحظ من الشكل (3) أيضاً، أن زمن بداية ثبات طول الأثر وتشبعه يقل بزيادة درجة حرارة المحلول القاشط للطاقة نفسها؛ إذ إن زيادة درجة حرارة المحلول القاشط تزيد من سرعة التفاعل بين المحلول والكاشف، فتزيد من معدل قشط الأثر باتجاه العمق، وبذلك تسرِّع من نمو الأثر ووصوله إلى حالة التشبع (saturation)، وإن مقدار القيمة القصوى لطول الأثر (نقطة التشبع) تحصل عند القيمة نفسها لدرجات الحرارة المختلفة للطاقة الواحدة لجسيمات ألفا التي تساوي هنا بحدود($L=8.4\ \mu m$) لطاقة ألفا 2.5 MeV؛ إذ إنها تختلف باختلاف طاقة الجسيم الساقط [21، 22، 23، 24]، وتعتمد على نوع الكاشف وتركيبه ومنشئِه، وترتبط بشكل وثيق بمعدل نمو الأثر.

17، 18] فضلاً عن عوامل أخرى؛ إذ إن دراسة تأثير العوامل البيئية في الكاشف تمكّننا من قياس التأثيرات الحقيقية للجسيمات المشحونة التي يقصف بها الكاشف.

يعّد معدل القشط العام أحد معالم الكاشف. فهو معلم كشفي (detecting parameter) لاعتماده على عوامل منها؛ نقاوة المادة الأساسية المصنّع منها الكاشف، ومدى تجانسها وتماثل خواصها, وطبيعة جزيئات البوليمر المكون للكاشف، وظروف بلمرتها خلال عملية إنتاج الكاشف، فضلاً عن اعتمادها على العوامل البيئية عند تشعيع الكاشف. وإلى جانب كون V_B معلماً كشفياً فإنه يعد معلمًا قشطياً (etching parameter) مهماً، لاعتماده على نوع المحلول الكيميائي القاشط المستعمل في إظهار الآثار في الكاشف وتركيزه ودرجة حرارته [11، 12، 14]. عموماً، فإن معدل القشط العام (V_B) للكاشف يمتلك قيمة واحدة، وقد تكون محددة تحت الظروف القشطية والبيئية المستخدمة [19] وضمن سمك مزال قليل من سطح الكاشف، في حين أن قيمته قد تتغير عندما يزال سمك كبير لفترات قشط طويلة.

تعد طريقة قياس "طول- قطر" الأثر (L_e-D) طريقة حديثة وليست سهلة، ولكن نتائجها دقيقة مقارنة بالطرائق الأخرى التي كانت تستعمل سابقاً في عملية إيجاد V_B. فهذه الطريقة تتطلب الحصول على صور لعدد كبير من الآثار المتكونة في الكاشف، وتتطلب قياساً دقيقاً لكل من قطر الأثر (D) وطوله (L_e) تجريبياً بشكل مباشر وهذا يحتاج إلى وقت وجهد غير قليل. يتم حساب معدل القشط العام (V_B) من العلاقة [20، 13، 21]:

$$V_B = \frac{D^2}{4\,t\,L_e}\left[1+\sqrt{1+\frac{4L_e^2}{D^2}}\right] \qquad (1)$$

حيث L_e طول الأثر، وD قطر فتحة الأثر، وt زمن القشط، كما هو موضح في الشكل (1).

يهدف البحث إلى إيجاد معدل القشط العام لكاشف CR-39 ودراسة تأثير درجة حرارة المحلول الكيميائي القاشط NaOH/water عليه، وإيجاد علاقة رياضية شبه تجريبية تبين نمط هذا التغير.

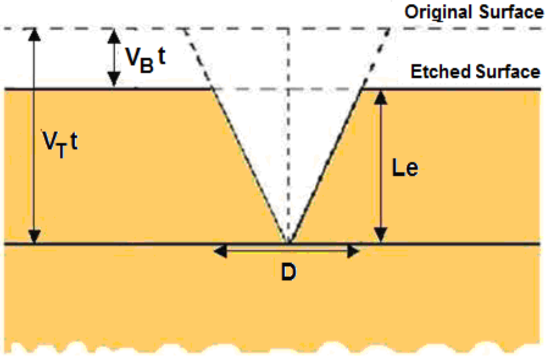

الشكل (1): رسم تخطيطي جانبي لـ "الأثر المقشوط" للسقوط العمودي للجسيمات.

طريقة العمل

استُعمل كاشف الأثر النووي البلاستيكي CR-39 ذو الحساسية العالية والخلفية الإشعاعية القليلة بسمك 200 µm لقياس معدل القشط العام له. استعملت أربع قطع من الكاشف بأبعاد $(1X1)cm^2$، ثم شُعِّعت بجسيمات ألفا بطاقة 2.5 MeV من مصدر أمريشيوم ^{241}Am نشاطه الإشعاعي (1µCi) والطاقة الرئيسية لجسيمات ألفا المنبعثة منه هي 5.485 MeV بمتوسط مدى في الهواء يقرب من 4.16 cm. تم الحصول على الطاقة 2.5 MeV من خلال تغيير البعد بين المصدر المشع والكاشف في الهواء. أُجريت عملية القشط الكيميائي للكاشف لإظهار آثار جسيمات ألفا، باستعمال المحلول المائي NaOH/water بتركيز 6.25 N عند درجات حرارة (55, 60, 65, 70) ± 1°C. تم تصوير الأشكال الجانبية (profiles) للآثار وقياس أقطارها وأطوالها لأزمان قشط مختلفة لمراحل نمو الأثر ضمن مرحلتي الأثر المخروطي المنتظم والقشط المفرط للآثار (over-etching)، وذلك لإيجاد معدل القشط العام بطريقة قياس "طول - قطر" الأثر(L_e-D) [12، 13].

استعملت في عملية تصوير الآثار المقشوطة وقياس أطوالها وأقطارها مباشرة منظومة حاسوبية متكونة من مجهر بصري مثبت عليها كاميرا رقمية (digital camera) من نوع MDCE-5A موصولة إلى حاسوب يعمل ضمن برنامج معين خاص بالكاميرا التي يتم تنصيبها في المنظومة، وذلك لإجراء القياسات على الآثار التي يتم تصويرها.

المجلد 8، العدد 1، 2015. ص ص. 49-55

المجلة الأردنية للفيزياء

ARTICLE

تأثير درجة حرارة المحلول الكيميائي في معدل القشط العام لكاشف CR-39

سعيد حسن سعيد النعيمي
قسم الفيزياء، كلية التربية للعلوم الصرفة، جامعة الموصل، العراق.

Received on: 30/1/2014; Accepted on: 22/4/2015

الملخص: في هذا البحث، تمت دراسة تأثير درجة حرارة المحلول القاشط في معدل القشط العام (V_B) لكاشف الأثر النووي CR-39. استعملت طريقة القياس المباشر لـ "طول- قطر" (L_e-D) آثار جسيمات ألفا في الكاشف. استعمل مصدر الأمريشيوم ^{241}Am نشاطه الإشعاعي 1µCi للتشعيع بجسيمات ألفا بطاقة 2.5MeV. قُشِط الكاشف بالمحلول المائي NaOH/water بتركيز 6.25 N بدرجات حرارة (70, 65, 60, 55) ± 1^{o}C. قيست أطوال الآثار وأقطارها من الصور المباشرة للآثار المقشوطة في الكاشف المشعع. وجد أن معدل القشط العام يزداد أسياً مع درجة حرارة المحلول؛ إذ تراوحت قيمه بين (1.1022-1.424) µm.h^{-1} ضمن مدى درجة الحرارة المذكورة.

الكلمات المفتاحية: CR-39، قشط الأثر، جسيمات ألفا، كاشف الأثر النووي.

Effects of Chemical Solution Temperature on the Bulk Etch Rate of the Detector CR-39

Sa'eed Hassan Sa'eed Al-Nia'emi
Physics Department, College of Education for Pure Scince, Mosul University, Iraq.

Abstract: The effects of chemical etchant temperatures on the bulk etch rate V_B of CR-39 SNTDs were investigated. The bulk etch rate is determined through direct measurement of "length-diameter Le-D" of alpha-particles track in the detector. Alpha-particles irradiations were made with energy of 2.5MeV under normal incidence radioactive source ^{241}Am of an activity of 1 µCi. The detector is etched by an aqueous solution of NaOH/water with 6.25 normality N in the temperature range (55, 60, 65, 70) ±1 ^{o}C. The lengths and diameters of alpha-particles tracks are directly measured from the tracks images obtained from the irradiated detector. It was found that the bulk etch rate is exponentially increasing with the temperature of the solution and its values ranged between (1.1022-1.424) µm.h^{-1} in the above temperature range.

Keywords: CR-39; Track etch; Alpha particle; Nuclear track detector.

المقدمة

تؤدي العوامل البيئية دوراً كبيراً في التأثير على الصفات الكشفية والتسجيلية لكواشف الأثر النووي البلاستيكية SSNTD'S كالحساسية والزاوية الحرجة ومعدل القشط العام (V_B) ومعدل قشط الأثر (V_T) وطول الآثار (L_e) المتكونة فيها وأقطارها (D). من هذه العوامل الأمواج فوق الصوتية [1] والإشعاعات الكهرومغناطيسية مثل الأشعة فوق البنفسجية [2، 3، 4] وأشعة غاما [5، 6] والأشعة السينية [7] وأشعة الليزر [8]، والمجال الكهربائي [9]، والمعالجة الحرارية للكاشف (التسخين) [10]، وكذلك نوع المحلول القاشط وتركيزه ودرجة حرارته [11، 12، 13]، ونوع المحاليل المضافة إلى المحلول القاشط [14]، وعملية رجّ المحلول القاشط (stirring) في أثناء القشط [15]. وهناك عوامل تخص الكاشف نفسه لها أيضاً تأثير في حساسيته ومعلماته مثل نوع الكاشف ومنشئه [16]،

Corresponding Author: Sa'eed Hassan Al-Nia'emi **Email**: saeed_alnaeme@yahoo.com

Authors Index

Subject Index

المراجع: يجب طباعة المراجع بأسطر مزدوجة ومرقمة حسب تسلسلها في النص. وتكتب المراجع في النص بين قوسين مربعين. ويتم اعتماد اختصارات الدوريات حسب نظام Wordlist of Scientific Reviewers.

الجداول: تعطى الجداول أرقاما متسلسلة يشار إليها في النص. ويجب طباعة كل جدول على صفحة منفصلة مع عنوان فوق الجدول. أما الحواشي التفسيرية، التي يشار إليها بحرف فوقي، فتكتب أسفل الجدول.

الرسوم التوضيحية: يتم ترقيم الأشكال والرسومات والرسومات البيانية (المخططات) والصور، بصورة متسلسلة كما وردت في النص.

تقبل الرسوم التوضيحية المستخرجة من الحاسوب والصور الرقمية ذات النوعية الجيدة بالأبيض والأسود، على ان تكون أصيلة وليست نسخة عنها، وكل منها على ورقة منفصلة ومعرفة برقمها بالمقابل. ويجب تزويد المجلة بالرسومات بحجمها الأصلي بحيث لا تحتاج إلى معالجة لاحقة، وألا تقل الحروف عن الحجم 8 من نوع Times New Roman، وألا تقل سماكة الخطوط عن 0.5 وبكثافة متجانسة. ويجب إزالة جميع الألوان من الرسومات ما عدا تلك التي ستنشر ملونة. وفي حالة إرسال الرسومات بصورة رقمية، يجب أن تتوافق مع متطلبات الحد الأدنى من التمايز (1200 dpi Resolution) لرسومات الأبيض والأسود الخطية، و 600 dpi للرسومات باللون الرمادي، و300 dpi للرسومات الملونة. ويجب تخزين جميع ملفات الرسومات على شكل (jpg)، وأن ترسل الرسوم التوضيحية بالحجم الفعلي الذي سيظهر في المجلة. وسواء أرسل المخطوط بالبريد أو عن طريق الشبكة (Online)، يجب أرسال نسخة ورقية أصلية ذات نوعية جيدة للرسومات التوضيحية.

مواد إضافية: تشجع المجلة الباحثين على إرفاق جميع المواد الإضافية التي يمكن أن تسهل عملية التحكيم. وتشمل المواد الإضافية أي اشتقاقات رياضية مفصلة لا تظهر في المخطوط.

المخطوط المنقح (المعدَل) والأقراص المدمجة: بعد قبول البحث للنشر وإجراء جميع التعديلات المطلوبة، فعلى الباحثين تقديم نسخة أصلية ونسخة أخرى مطابقة للأصلية مطبوعة بأسطر مزدوجة، وكذلك تقديم نسخة إلكترونية تحتوي على المخطوط كاملا مكتوبا على Microsoft Word for Windows 2000 أو ما هو استجد منه. ويجب إرفاق الأشكال الأصلية مع المخطوط النهائي المعدل حتى لو تم تقديم الأشكال إلكترونيا. وتخزن جميع ملفات الرسومات على شكل (jpg)، وتقدم جميع الرسومات التوضيحية بالحجم الحقيقي الذي ستظهر به في المجلة. ويجب إرفاق قائمة ببرامج الحاسوب التي استعملت في كتابة النص، وأسماء الملفات على قرص مدمج، حيث يعلَم القرص بالاسم الأخير للباحث، وبالرقم المرجعي للمخطوط للمراسلة، وعنوان المقالة، والتاريخ. ويحفظ في مغلف واقٍ.

الفهرسة: تقوم المجلة الأردنية للفيزياء بالإجراءات اللازمة لفهرستها وتلخيصها في جميع الخدمات الدولية المعنية.

حقوق الطبع

يُشكِّل تقديم مخطوط البحث للمجلة اعترافاً صريحاً من الباحثين بأنَ مخطوط البحث لم يُنْشَر ولم يُقَدَّم للنشر لدى أي جهَة أخرى كانت وبأي صيغة ورقية أو إلكترونية أو غيرها. ويُشترط على الباحثين ملء أنموذج يَنُصُ على نقْل حقوق الطبع لتُصبح ملكاً لجامعة اليرموك قبل الموافقة على نشر المخطوط. ويقوم رئيس التحرير بتزويد الباحثين بإنموذج نقل حقوق الطبع مع النسخة المُرْسَلَة للتنقيح. كما ويُمنع إعادة إنتاج أيِّ جزء من الأعمال المنشورة في المجلَة من دون إذن خَطِّيٍّ مُسبَق من رئيس التحرير.

إخلاء المسؤولية

إن ما ورد في هذه المجلة يعبر عن آراء المؤلفين، ولا يعكس بالضرورة آراء هيئة التحرير أو الجامعة أو سياسة اللجنة العليا للبحث العلمي أو وزارة التعليم العالي والبحث العلمي. ولا يتحمل ناشر المجلة أي تبعات مادية أو معنوية أو مسؤوليات عن استعمال المعلومات المنشورة في المجلة أو سوء استعمالها.

معلومات عامة

المجلة الأردنية للفيزياء هي مجلة بحوث علميّة عالمية متخصصة مُحكمة تصدر بدعم من صندوق دعم البحث العلمي، وزارة التعليم العالي والبحث العلمي، عمان، الأردن. وتقوم بنشر المجلة عمادة البحث العلمي والدراسات العليا في جامعة اليرموك، إربد، الأردن. وتنشر البحوث العلمية الأصيلة، إضافة إلى المراسلات القصيرة Short Communications، والملاحظات الفنية Technical Notes، والمقالات الخاصّة Feature Articles، ومقالات المراجعة Review Articles، في مجالات الفيزياء النظرية والتجريبية، باللغتين العربية والإنجليزية.

تقديم مخطوط البحث

تقدم البحوث عن طريق إرسالها إلى البريد الإلكتروني : jjp@yu.edu.jo

تقديم المخطوطات إلكترونيًا: اتبع التعليمات في موقع المجلة على الشبكة العنكبوتية.

ويجري تحكيمُ البحوثِ الأصيلة والمراسلات القصيرة والملاحظات الفنية من جانب مُحكِّمين اثنين في الأقل من ذوي الاختصاص والخبرة. وتُشَجِّع المجلة الباحثين على اقتراح أسماء المحكمين. أما نشر المقالات الخاصّة في المجالات الفيزيائية النَشِطَة، فيتم بدعوة من هيئة التحرير، ويُشار إليها كذلك عند النشر. ويُطْلَب من كاتب المقال الخاص تقديم تقرير واضح يتّسم بالدقة والإيجاز عن مجال البحث تمهيداً للمقال. وتنشر المجلةُ أيضاً مقالات المراجعة في الحقول الفيزيائية النشطة سريعة التغيُر، وتُشَجَع كاتبي مقالات المراجعة أو مُستَكتبيها على إرسال مقترحٍ من صفحتين إلى رئيس التحرير. ويُرفَق مع البحث المكتوب باللغة العربية ملخص (Abstract) وكلمات دالة (Keywords) باللغة الإنجليزية.

ترتيب مخطوط البحث

يجب أن تتم طباعة مخطوط البحث ببنط 12 نوعه Times New Roman، وبسطر مزدوج، على وجه واحد من ورق A4 (21.6 × 27.9 سم) مع حواشي 3.71 سم ، باستخدام معالج كلمات ميكروسوفت وورد 2000 أو ما اسْتَجَد منه. ويجري تنظيم أجزاء المخطوط وفق الترتيب التالي: صفحة العنوان، الملخص، رموز التصنيف (PACS)، المقدّمة، طرق البحث، النتائج، المناقشة، الخلاصة، الشكر والعرفان، المراجع، الجداول، قائمة بدليل الأشكال والصور والإيضاحات، ثَمَّ الأشكال والصور والإيضاحات. وتُكْتَب العناوين الرئيسة بخطٍ **غامق**، بينما تُكْتَب العناوين الفرعية بخطٍ *مائل*.

صفحة العنوان: وتشمل عنوان المقالة، أسماء الباحثين الكاملة وعناوين العمل كاملة. ويكتب الباحث المسؤول عن المراسلات اسمه مشارا إليه بنجمة، والبريد الإلكتروني الخاص به. ويجب أن يكون عنوان المقالة موجزا وواضحا ومعبرا عن فحوى (محتوى) المخطوط، وذلك لأهمية هذا العنوان لأغراض استرجاع المعلومات.

الملخص: المطلوب كتابة فقرة واحدة لا تزيد على مائتي كلمة، موضحة هدف البحث، والمنهج المتبع فيه والنتائج وأهم ما توصل إليه الباحثون.

الكلمات الدالة: يجب أن يلي الملخص قائمة من 4-6 كلمات دالة تعبر عن المحتوى الدقيق للمخطوط لأغراض الفهرسة.

PACS: يجب إرفاق الرموز التصنيفية، وهي متوافرة في الموقع http://www.aip.org/pacs/pacs06/pacs06-toc.html.

المقدمة: يجب أن توضّح الهدف من الدراسة وعلاقتها بالأعمال السابقة في المجال، لا أن تكون مراجعة مكثفة لما نشر (لا تزيد المقدمة عن صفحة ونصف الصفحة مطبوعة).

طرائق البحث (التجريبية / النظرية): يجب أن تكون هذه الطرائق موضحة بتفصيل كاف لإتاحة إعادة إجرائها بكفاءة، ولكن باختصار مناسب، حتى لا تكون تكرارا للطرائق المنشورة سابقا.

النتائج: يستحسن عرض النتائج على صورة جداول وأشكال حيثما أمكن، مع شرح قليل في النص ومن دون مناقشة تفصيلية.

المناقشة: يجب أن تكون موجزة وتركز على تفسير النتائج.

الاستنتاج: يجب أن يكون وصفا موجزا لأهم ما توصلت إليه الدراسة ولا يزيد عن صفحة مطبوعة واحدة.

الشكر والعرفان: الشكر والإشارة إلى مصدر المنح والدعم المالي يكتبان في فقرة واحدة تسبق المراجع مباشرة.

Subscription Form

Jordan Journal of

PHYSICS

An International Peer-Reviewed Research Journal issued by the Support of the Scientific Research Support Fund

Published by the Deanship of Research & Graduate Studies, Yarmouk University, Irbid, Jordan

Name: .... :الأسم
Specialty:..:التخصص
Address: ....:العنوان
P.O. Box:.. : صندوق البريد
City & Postal Code: ....:المدينة/الرمز البريدي
Country: ....:الدولة
Phone: ....:رقم الهاتف
Fax No:... :رقم الفاكس
E-mail:.. :البريد الإلكتروني
No. of Subscription: .... :عدد الإشتراكات
Method of Payment:... :طريقة الدفع
Amount Enclosed:... :المبلغ المرفق
Signature: ....:التوقيع

Cheques should be paid to Deanship of Research and Graduate Studies - Yarmouk University.

I would like to subscribe to the Journal
For

- ☐ One Year
- ☐ Two Years
- ☐ Three Years

One Year Subscription Rates

	Inside Jordan	Outside Jordan
Individuals	JD 8	€ 40
Students	JD 4	€ 20
Institutions	JD 12	€ 60

Correspondence

Subscriptions and Sales:

Prof. Nehad M. Tashtosh
Deanship of Research and Graduate Studies
Yarmouk University
Irbid – Jordan
Telephone: 00 962 2 711111 Ext. 2075
Fax No.: 00 962 2 7211121

المملكة الأردنية الهاشمية

جامعة اليرموك

المجلة الأردنية
للفيزياء

مجلة بحوث علمية عالمية متخصصة محكّمة

تصدر بدعم من صندوق دعم البحث العلمي

المجلد (8)، العدد (1)، 2015م / 1436هـ

المجلة الأردنية

للفيزياء

مجلة بحوث علمية عالمية محكّمة

المجلد (8)، العدد (1)، 2015م / 1436هـ

المجلة الأردنية للفيزياء: مجلة علمية عالمية متخصصة محكّمة تصدر بدعم من صندوق دعم البحث العلمي، وزارة التعليم العالي والبحث العلمي، الأردن، وتصدر عن عمادة البحث العلمي والدراسات العليا، جامعة اليرموك، إربد، الأردن.

ترسل البحوث إلى العنوان التالي:

الأستاذ الدكتور نهاد محمد طشطوش
رئيس تحرير المجلة الأردنية للفيزياء
عمادة البحث العلمي والدراسات العليا، جامعة اليرموك
إربد ، الأردن
هاتف 00 962 2 7211111 **فرعي** 2075
E-mail: *jjp@yu.edu.jo*
Website: *http://Journals.yu.edu.jo/jjp*